Study on Ion Cyclotron Emission Driven by Fusion Product in Tokamak Plasma

Shuhei Sumida

February 2019

Study on Ion Cyclotron Emission Driven by Fusion Product in Tokamak Plasma

Shuhei Sumida

Doctoral Program in Physics

Submitted to the Graduate School of

Pure and Applied Sciences

in Partial Fulfillment of the Requirements

for the Degree of Doctor of Philosophy in

Science

at the

University of Tsukuba

Content

Chapter 1
Introduction

In this chapter, backgrounds and a purpose of this study are explained. First, advantages of nuclear fusion energy power generation and approaches toward realization of the nuclear fusion power generation are introduced. Next, a role of fast ions produced by fusion reactions in the reactor is explained. Then, backgrounds and remaining issues of research on ion cyclotron emissions are explained. Finally, the purpose of this study is described.

1.1. Nuclear fusion energy

Baseload powers are indispensable to prosperity of modern society. However, every present baseload power generations have not only merits, but also demerits. The present baseload powers mainly consist of i) thermal power generation, ii) hydroelectric power generation, and iii) nuclear power generation. i) The thermal power generation can stably supply a large amount of energy. However, its resource amounts of the fossil fuels such as oil, coal and natural gas are finite. In addition, the fuel burning produces carbon dioxides, which promote the global warming. ii) The hydroelectric power generation can also supply a large amount of energy, but its energy supply stability depends on the weather. iii) The nuclear power generation can stably supply a large amount of energy and emit no carbon dioxides. However, it produces massive high-level radioactive wastes. The high-level radioactive wastes must be controlled for several ten thousands years. In addition, the fission reactions used for the reactor are chain reactions. Therefore, the nuclear power generation has a potential risk of runaway reactions.

Nuclear fusion power generation is expected as a future baseload power generation. Nuclear fusion reaction is a reaction where two and more atomic nucleuses fuse and become different atomic nucleuses. In the case of relatively light atomics, the total masses of the atomic nucleuses after the fusion reaction are lighter than those before the reaction. The atomic nucleuses produced by the fusion reaction have high energy due to the mass defect and are utilized for heat generation of the fusion power reactor. The following hydrogen isotope fusion reactions are going to be caused for the fusion power generation.

$$\mathrm{D} + \mathrm{T} \rightarrow \alpha(3.52\ \mathrm{MeV}) + \mathrm{n}(14.06\ \mathrm{MeV}) \tag{1.1}$$

where, D and T are deuterium (= $^{2}_{1}\mathrm{H}$) and tritium ions (= $^{3}_{1}\mathrm{H}$), respectively. α is a helium ion (= $^{4}_{2}\mathrm{He}$) and n is a neutron. To occur the fusion reaction, the atomic nucleuses must be accelerated so as to have enough high energy and collide with each other. The DT fusion reaction is the most easily caused fusion reaction in a region of relatively low energy.

Advantages of the fusion power generations are as follows. The fusion power generation can stably supply a large amount of the energy because weather is not related to the process of the power generation. An enormous amount of D can be extracted from seawater since the seawater contains a low percentage of heavy water (D_2O). Neutrons produced by the DT fusion reaction are utilized not only for the heat generation of the reactor, but also for the production of T ions via the following fusion reaction using lithium.

$$\mathrm{Li} + \mathrm{n} \rightarrow \mathrm{T} + \alpha + 4.8\ \mathrm{MeV} \tag{1.2}$$

where, Li is a lithium ion (= $^{6}_{3}\mathrm{Li}$). The lithium is also included in the seawater. This fusion reaction is going to be caused inside the reactor vessel. In addition, the DT fusion reaction is not a chain reaction, and carbon dioxides and high-level radioactive wastes are not produced by the fusion reaction. Hence, the fusion power generation has many advantages in comparison with the present baseload power generations such as thermal, hydroelectric, and nuclear power generations.

1.2. Approach toward realization of fusion reactor

The cross section of the DT fusion reaction is peaked around high temperature of 40 keV (about 464 million K) [1]. All atoms are ionized and become plasma under such high temperature conditions. The plasma consists of the electrically charged particles and neutral particles. In the high-temperature plasma, the proportion of the neutral particles becomes less due to ionization. Therefore, the high-temperature plasma can be confined by the magnetic field because the charged particles move Larmor motions in the magnetic field and a high-temperature region can be separated from the wall of the vessel. This is a concept of magnetic confinement fusion reactor. In this method, the high-temperature plasma is magnetically confined and efficiently causes the fusion reactions.

Developments of torus-shaped magnetic confinement devices have been advanced toward the realization of the fusion reactor. In the fusion reactor, the fusion power from the plasma P_{f} must be sufficiently over the external heating power P_{h}. The energy gain factor Q is defined as $Q = P_{\mathrm{f}}/P_{\mathrm{h}}$. Tokamak device [2], which is one of the torus magnetic confinement devices, is the most promising magnetic fusion device. High performance plasma that is equivalent to $Q > 1$ has been already produced in the tokamak devices [3, 4].

The experimental devices of the tokamak have been constructed and the physics of the tokamak plasma has been studied all over the world. Representative large- and middle-size tokamak devices are as follows: JET (Joint European Torus) [5] in UK (the United Kingdom), TFTR (Tokamak Fusion Test Reactor) [6] in US (the United States), ASDEX (Axisymmetric Divertor Experiment) / ASDEX Upgrade [7] in Germany, DIII (Doublet III) -D [8] in USA, KSTAR (Korean Superconducting Tokamak Advanced Research) in Korea [9], and JT-60 (Japan Atomic Energy Research Institute Tokamak 60) / JT-60U (JT-60 Upgrade) [10] in Japan. In the JET and TFTR, the DT plasma experiments have been carried out and more than 10 MW fusion powers were already achieved [11, 12]. In some tokamak devices such as JT-60U, only H and D plasma experiments have been carried out because they are not designed to be able to treat the tritium. In high-temperature D plasma, the following DD fusion reactions mainly occur.

$$\mathrm{D} + \mathrm{D} \rightarrow \mathrm{T}(1.01\ \mathrm{MeV}) + \mathrm{p}(3.03\ \mathrm{MeV}) \tag{1.3a}$$

$$\mathrm{D} + \mathrm{D} \rightarrow {}^{3}_{2}\mathrm{He}(0.82\ \mathrm{MeV}) + \mathrm{n}(2.45\ \mathrm{MeV}) \tag{1.3b}$$

where, p is a proton (= $^{1}_{1}\mathrm{H}$) and $^{3}_{2}\mathrm{He}$ is a helium-3 ion. The $^{3}_{2}\mathrm{He}$ ion is simply called $^{3}\mathrm{He}$ ion in this study. The DD fusion reactions of Eq. (1.3a) and Eq. (1.3b) occur at almost same probabilities. Toward achieving high performance plasma production with $Q \geq 10$ and steady-state plasma production with $Q \sim 5$ in the DT plasma experiment, ITER is being constructed in France by collaborations with China, the European Union,

India, Korea, Russia, US and Japan in recent years [13].

1.3. Role of fusion produced ions

To maintain the high fusion reaction rate, the plasma temperature must be kept high by heating the plasma. The main heating source in the DT fusion reactor is high-energy α particles produced by the DT fusion reactions. The high-energy α particles heat the bulk plasma via Coulomb collisions. The bulk electrons are mainly heated by the α particles when the α particles have relatively high energies. Then, the α particles mainly heat the bulk ions when their energies are decreased by the collisions and become relatively low. The proportion of the external heating power can be reduced when the α particles efficiently heat the plasma. Therefore, the α particle heating efficiency directly leads to the plasma performance and the economic efficiency of the DT fusion reactor. To make the heating efficiency high, particle and energy loss of the α particles must be reduced as small as possible until the α particles deliver their most energies to the bulk plasma. In addition, the particle loss of the α particles also increases local heat loads on the wall [14]. Good confinement of the α particles in the tokamak plasma is indispensable to the realization of the DT fusion reactor. Hence, understanding their confinement and transport properties is essential to design the reactor.

1.4. Wave-particle interaction in tokamak plasma

Many types of wave-particle interactions occur in the plasma [15-17]. In some wave-particle interactions, the high-energy ions (also called fast ions) deliver their energies to waves in the plasma and grow the waves. Then, the fast ions are transported toward outside the plasma by the waves. Namely, some wave-particle interactions cause the energy loss and the particle loss of the fast ions. In other words, these interactions deteriorate the confinement properties of the fast ions. Fishbone instability [15], Alfvén eigenmodes (AEs) [16], and energetic particle modes (EPMs) [17] are representative wave-particle interactions that lead to serious amount of the energy and particle loss of the fast ions. Therefore, investigating such wave-particle interactions is also important to understand the confinement property of the fast ions such as the α particles produced by the fusion reaction and to avoid the interactions that cause the fast ion losses in the fusion reactor.

1.5. Ion cyclotron emission (ICE)

In the tokamak plasma, ion cyclotron range of frequency (ICRF) waves considered to be driven by a kind of the wave-particle interactions have been observed [18-30]. These emissions of the ICRF waves are called ion cyclotron emissions (ICEs). The ICEs are often observed in several tokamak devices, e.g., JET [18-20], TFTR [21, 22], JT-60U [23-26], ASDEX Upgrade [27], DIII-D [28, 29], and KSTAR [30]. The ICEs often appear when the number of the fast ions increases, e.g., neutral beams (NBs) are injected into the plasma, the fusion reactions occur, and ions are accelerated by the ICRF waves. The ICEs are thought to be a kind of the wave-particle interactions between the fast ions and the ICRF waves. It is considered that frequencies, mode structures, and temporal behaviors of ICEs would depend on behaviors of the fast ions. Therefore, the ICEs are expected as fast ion diagnostics in ITER, particularly diagnostics for the DT fusion produced fast α

particles [31, 32].

The ICEs thought to be driven by the DT fusion produced fast α particles (ICE(α)) have been observed in the JET [18, 19] and the TFTR DT plasma experiments [21, 22]. On JT-60U, the ICEs thought to be driven by DD fusion produced fast ^{3}He ions [ICE(^{3}He)], fast T ions [ICE(T)] and fast H ions [ICE(H)] have been observed [23-26]. These ICEs originating from the fusion produced fast ions are generally observed in the frequency near the ion cyclotron frequency at the midplane edge of the plasma on low field side. The location of the midplane edge of the plasma on low field side is shown in Fig. 1.1. The toroidal magnetic field strength is inversely proportional to a distance from the axis of the torus device (major radius). The low field side is the side where the toroidal magnetic field strength is lower as shown in Fig. 1.1. In addition, correlations between the ICEs and edge-localized modes have been observed [18, 23, 27, 30]. Hence, the ICEs are considered to be excited near the plasma edge on the low field side.

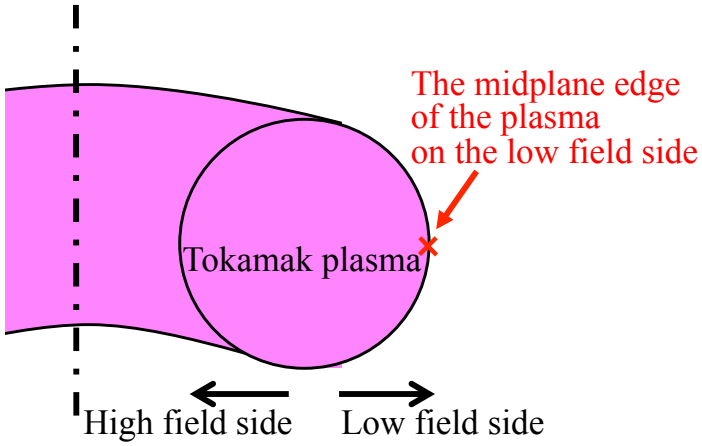

Figure 1.1. A schematic drawing of the location of the midplane edge of the plasma on the low field side.

The fast ion velocity distribution near the plasma edge on the low field side is predicted to have a strong pitch-angle anisotropy and a positive gradient structure in the energy direction (bump-on-tail structure) [18, 20, 22, 27, 30]. Here, a pitch angle is defined as an angle between the velocity vector of the particle and the magnetic field line. The reasons for the formation of the distribution having the pitch-angle anisotropy and the bump-on-tail structure near the plasma edge on the low field side are because the fast ions produced around the plasma center can pass through the plasma edge on the low field side under limited conditions of their energies and pitch angles. The detailed process for the formation of such fast ion velocity distribution near the plasma edge on the low field side is explained in Section 2.2.3. In general, the ICRF waves can be excited by ions having non-thermal velocity distribution [33-35]. Hence, it is believed that the fast ion velocity distribution near the midplane edge of the plasma on the low field side drives the ICEs.

The magneto-acoustic cyclotron instability (MCI) and its eigenmodes have been suggested as emission mechanisms for the ICEs from theoretical analyses [19, 20, 30, 35-44]. The MCI is destabilized by the anisotropy and the bump-on-tail structure in the ion velocity distribution and becomes unstable under the ion cyclotron resonance condition. It is considered that the MCI can be driven by the fast ion velocity distribution near the plasma edge on the low field side. Drifting-ring-type ion velocity distribution functions (see Eq. (5.7) as an example), which are the velocity distributions having only an almost single energy and pitch angle, are often used for the fast ion velocity distribution in the theoretical analyses of the MCI [19, 20, 22, 30, 35, 36, 39-42, 44].

To understand the emission mechanism for the ICE, investigations of the fast ion velocity distributions and of wave dispersion relations are important. This is because the ICE is considered to be a kind of the wave-particle interactions. The fast ion distributions are possible driving sources for the ICE and we can understand the property of the interacted waves from the dispersion relations. However, there are few studies [45] so far at which the fast ion velocity distributions near the plasma edge on the low field side are evaluated under conditions, where plasma parameters in the experiments and collisional effects are taken into account. Hence, it is not clear what characteristics of the evaluated fast ion distributions are formed near the plasma edge on the low field side. Then, it is also not known whether the evaluated distribution has similar characteristics to the drifting-ring-type distribution. In addition, it is not clear whether both frequencies and wavenumbers of the ICE measured in the experiments are consistent with the MCI. Although the toroidal wavenumbers of the ICEs have been quantitatively measured only on JT-60U, only first measurement results of the wavenumbers in the toroidal direction have been reported [24-26]. Moreover, in order to identify key characteristics of the fast ion velocity distribution driving the ICE, it has been reported so far in few works [45] at which the distributions are compared between cases when the ICE is observed and not. These issues are the main motivations behind this study. Elucidation of the emission mechanism for the ICE can contribute to the application to the fast ion diagnostics with the ICE and understanding of behaviors of the fast ions in the tokamak plasma.

1.6. Purpose of this study

As we mentioned in Section 1.5, the ICEs driven by the fusion produced fast ions such as ICE(α) are expected as the diagnostics for the fusion products in ITER [31, 32]. On JT-60U, the DT plasma experiments were not carried out, but the D plasma experiments have been implemented and the ICEs thought to be driven by the DD fusion products such as ICE(^{3}He), ICE(T) and ICE(H) have been observed [23-26]. In addition, on JT-60U, the quantitative measurements of the toroidal wavenumbers of these ICEs have been successful [24-26]. In general, the ICRF waves are categorized into fast Alfvén waves and slow Alfvén waves in accordance with their phase speeds [46]. The waves of the ICE(α) are considered to belong to the fast Alfvén waves. The waves of the ICE(^{3}He) and ICE(H) observed on JT-60U are also on the fast Alfvén wave branch, while those of the ICE(T) are on the slow Alfvén wave branch [24-26]. On JT-60U, the ICE(H) is observed only under limited plasma conditions [26]. Thus, in this study, we focused on the ICE(^{3}He) in JT-60U as a typical ICE driven by the fusion product in the tokamak plasma.

The purpose of this study is to reveal the emission mechanism for the ICE(^{3}He) in terms of the wave dispersion and of the fast ^{3}He ion velocity distribution. In this study, we carried out the following analyses. First, we evaluated the fast ^{3}He ion velocity distribution by using a fast ion orbit following Monte-Carlo code (OFMC) [47]. Then, we confirmed that the distribution has similar characteristics to the drifting-ring-type distribution. In addition, we newly developed the wave dispersion code to solve the dispersion of the MCI, and compared both of the frequency and the toroidal wavenumber between the experimental observations of the ICE(^{3}He) and the calculations of the MCI driven by the drifting-ring-type distribution. Next, we more quantitatively evaluated the fast ^{3}He ion velocity distribution, and compared the distributions between the cases when the ICE(^{3}He) is observed and not in order to identify the key characteristics of the distribution driving the ICE(^{3}He). Finally, we investigated influences of the characteristics of the fast ^{3}He ion distribution on the growth rate of the MCI.

References in Chapter 1

[1] K. Miyamoto, *Plasma Physics and Controlled Nuclear Fusion,* Springer, New York (2005).

[2] L. A. Arsimovitch, Nucl. Fusion **12**, 215 (1972).

[3] JET Team, Nucl. Fusion **32**, 187 (1992).

[4] T. Fujita *et al.*, Nucl. Fusion **39**, 1627 (1999).

[5] F. Romanelli and on behalf of JET Contributors, Nucl. Fusion **55**, 104001 (2015).

[6] R. J. Hawryluk *et al.*, Phys. Plasmas **5**, 1577 (1998).

[7] A. Kallenbach for the ASDEX Upgrade Team and the EUROfusion MST1 Team, Nucl. Fusion **57**, 102015 (2017).

[8] S. L. Allen and DIII-D Team, Nucl. Fusion **41**, 1341 (2001).

[9] J. G. Kwak *et al.*, Nucl. Fusion **53**, 104005 (2013).

[10] S. Ide and the JT-60 Team, Nucl. Fusion **45**, S48 (2005).

[11] M. G. Bell *et al.*, Nucl. Fusion **35**, 1429 (1995).

[12] A. Gibson and the JET Team, Phys. Plasmas **5**, 1839 (1998).

[13] R. Aymar *et al.*, Plasma Phys. Control. Fusion **44**, 519 (2002).

[14] T. Kurki-Suonio *et al*., Nucl Fusion **49**, 095001 (2009).

[15] K. McGuire *et al.*, Phys. Rev. Lett. **50**, 891 (1983).

[16] W. W. Heidbrink, Phys. Plasmas **15**, 055501 (2008).

[17] F. Zonca and L. Chen, Phys. Fluids **B5**, 3668 (1993).

[18] G. A. Cottrell *et al.*, Nucl. Fusion **33**, 1365 (1993).

[19] K. G. McClements *et al.*, Phys. Rev. Lett. **82**, 2099 (1999).

[20] K. G. McClements *et al*., Nucl. Fusion **58**, 096020 (2018).

[21] S. Cauffman and R. Majeski, Rev. Sci. Instrum. **66**, 817 (1995).

[22] S. Cauffman *et al.*, Nucl. Fusion **35**, 1597 (1995).

[23] H. Kimura *et al.*, Nucl. Fusion **38**, 1303 (1998).

[24] M. Ichimura *et al.*, Nucl. Fusion **48**, 035012 (2008).

[25] M. Ichimura *et al*., Proc. 22nd IAEA Fusion Energy Conf. (Geneva, Switzerland, 2008) EX/P8-2 (2008).

[26] S. Sato *et al.*, Plasma Fusion Res. **5**, S2067 (2010).

[27] R. D'Inca, *Ion Cyclotron Emission on ASDEX-Upgrade*, Ph. D. Thesis, Max Planck Institute for Plasma Physics (2014).

[28] W. W. Heidbrink *et al.*, Plasma Phys. Control. Fusion **53**, 085028 (2011).

[29] K. E. Thome *et al*., Rev. Sci. Instrum. **89**, 10I102 (2018).

[30] B. Chapman *et al.*, Nucl. Fusion **57**, 124004 (2017).

[31] K. G. McClements *et al.*, Nucl. Fusion **55**, 043013 (2015).

[32] R. O. Dendy, and K.G. McClements, Plasma Phys. Control. Fusion **57**, 044002 (2015).

[33] A. Iiyoshi *et al*., Phys. Fluids **10**, 749 (1967).

[34] R. C. Davidson and J. M. Ogden, Phys. Fluids **18**, 1045 (1975).

[35] V. S. Belikov and Ya. I. Kolesnichenko, Sov. Phys. Tech. Phys. **20**, 1146 (1976).

[36] R. O. Dendy *et al.*, Phys. Plasmas **1**, 1918 (1994).

[37] N. N. Gorelenkov and C. Z. Cheng, Phys. Plasmas **2**, 1961 (1995).

[38] N. N. Gorelenkov and C. Z. Cheng, Nucl. Fusion **35**, 1743 (1995).

[39] K. G. McClements *et al*., Phys. Plasmas **3**, 543 (1996).

[40] T. Fülöp *et al*., Nucl. Fusion **37**, 1281 (1997).

[41] T. Fülöp and M. Lisak, Nucl. Fusion **38**, 761 (1998).

[42] L. Carbajal *et al.*, Phys. Plasmas **21**, 012106 (2014).

[43] N. N. Gorelenkov, New J. Phys. **18**, 105010 (2016).

[44] L. Carbajal *et al.*, Phys. Rev. Lett. **118**, 105001 (2017).

[45] T. Hellsten *et al.*, Nucl. Fusion **46**, S442 (2006).

[46] T. H. Stix, *Waves in Plasmas*, Springer-Verlag, New York (1992).

[47] K. Tani *et al.*, J. Phys. Soc. Jpn. **50**, 1726 (1981).

Chapter 2
Motions of charged particles and wave propagations in the magnetized plasma

Both physics of the charged particles and of the ICRF waves in the magnetized plasma are important to understand behaviors of the ICE in the tokamak plasma since the ICE is considered to be a kind of the wave-particle interactions. In this chapter, motions of charged particles in the magnetic field and in the tokamak plasma are explained. Then, wave equations in the magnetized plasma are introduced.

2.1. Motions of charged particles in the magnetic field

In this section, we explain motions of charged particles in the magnetic field: Larmor motions, drifts, reflections by magnetic mirror and collisions in the magnetized plasma [1].

2.1.1. Larmor motion

Here, we explain the Larmor motion that the charged particle circles around the magnetic field line. In the magnetic field $\boldsymbol{B}$, the motion equation of the particle is given by,

$$m\frac{d\boldsymbol{v}}{dt} = q(\boldsymbol{E} + \boldsymbol{v}\times\boldsymbol{B}) \tag{2.1}$$

where, m and q are the mass and the electric charge of the charged particle, respectively. $\boldsymbol{E}$ is the electric field and $\boldsymbol{v}$ is the velocity of the charged particle. If there is no electric field $\boldsymbol{E}$, the motion equation is given by,

$$\frac{d\boldsymbol{v}}{dt} = \frac{qB}{m}(\boldsymbol{v}\times\boldsymbol{b}) \tag{2.2}$$

where,

$$\boldsymbol{b} \equiv \frac{\boldsymbol{B}}{B} \tag{2.3}$$

If $\boldsymbol{B}$ is described as $\boldsymbol{B} = (0, 0, B)$ in the orthogonal coordinate system (x, y, z), the velocity vectors of the charged particle $\boldsymbol{v} = (v_x, v_y, v_z)$ are given by,

$$\begin{aligned} v_x &= v_\perp \cos(\Omega t + \delta) \\ v_y &= -v_\perp \sin(\Omega t + \delta) \\ v_z &= v_{\parallel 0} \end{aligned} \tag{2.4}$$

where, Ω is the cyclotron angular frequency $\Omega = qB/m$, and δ is the initial phase of the motion. $v_\perp$ is

the velocity in the perpendicular direction to the magnetic field line ($v_\perp = \sqrt{v_x^2 + v_y^2}$), and $v_{\parallel 0}$ is the initial velocity in the parallel direction. Equation (2.4) indicates that the particle circles around the magnetic field line with the cyclotron angular frequency Ω. This motion is called Larmor motion. The radius of the Larmor motion is called Larmor radius r_L. On the orbit of the Larmor motion of Eq. (2.4), the centrifugal force and the Lorentz force are equal. The centrifugal force F_C is given by,

$$F_C = m\frac{v_\perp^2}{r_L} \tag{2.5}$$

and the Lorentz force F_L is given by,

$$F_L = qv_\perp B \tag{2.6}$$

Therefore, r_L can be given by,

$$r_L = \frac{mv_\perp}{|q|B} \tag{2.7}$$

The orbit of the particle is called full-gyro orbit and that of the center position of the Larmor motion is called guiding-center orbit.

2.1.2. Drift motion

The charged particle moves across the magnetic field line if forces in the perpendicular direction to the magnetic field line are applied and/or the magnetic field is inhomogeneous. These motions are called drift motions. If the general force $\boldsymbol{F}$ acts on the particle in the magnetic field $\boldsymbol{B}$, its motion equation is given by,

$$m\frac{d\boldsymbol{v}}{dt} = \boldsymbol{F} + q\boldsymbol{v}\times\boldsymbol{B} \tag{2.8}$$

Here, we define a velocity $\boldsymbol{v}'$ in the perpendicular direction to both $\boldsymbol{F}$ and $\boldsymbol{B}$ as,

$$\boldsymbol{v}' \equiv \frac{1}{q}\frac{\boldsymbol{F}\times\boldsymbol{b}}{B} \tag{2.9}$$

and define the velocity except for $\boldsymbol{v}'$ as,

$$\boldsymbol{u} \equiv \boldsymbol{v} - \boldsymbol{v}' \tag{2.10}$$

Then, the motion equation except for the motion with $\boldsymbol{v}'$ is given by,

$$m\frac{d\boldsymbol{u}}{dt} = q(\boldsymbol{u}\times\boldsymbol{B}) \tag{2.11}$$

Equations (2.10) and (2.11) indicate that the motion of the particle ($\boldsymbol{v}$) consists of the Larmor motion ($\boldsymbol{u}$) and the motion with $\boldsymbol{v}'$. Therefore, $\boldsymbol{v}'$ is called drift velocity $\boldsymbol{v}_\mathrm{d}$. The direction of $\boldsymbol{v}_\mathrm{d}$ is perpendicular to both $\boldsymbol{F}$ and $\boldsymbol{B}$. Namely, the charged particle moves across the magnetic field line with the drift velocity of $\boldsymbol{v}_\mathrm{d}$.

a) $\boldsymbol{E}\times\boldsymbol{B}$ drift

Here, we explain the drift motion if the homogeneous electric field $\boldsymbol{E}$ is superimposed on the magnetic field $\boldsymbol{B}$ and its direction is perpendicular to $\boldsymbol{B}$, or $\boldsymbol{E} \perp \boldsymbol{B}$. In this situation, the drift velocity $\boldsymbol{v}_E$ can be obtained by substitution of Coulomb force into the general force $\boldsymbol{F}$ in Eq. (2.9).

$$\boldsymbol{v}_E = \frac{\boldsymbol{E}\times\boldsymbol{b}}{B} \tag{2.12}$$

The drift velocity $\boldsymbol{v}_E$ is called $E\times B$ drift velocity. In the $E\times B$ drift motion, the velocities of the ion and electron are equal and their directions are the same.

b) $\nabla\boldsymbol{B}$ drift

Here, we explain the drift motion if the magnetic field strength $\boldsymbol{B}$ is inhomogeneous in the perpendicular direction to the magnetic field line, or $\nabla\boldsymbol{B} \perp \boldsymbol{B}$. At first, we derive a time-averaged value of the Lorentz force $F_L = q\boldsymbol{v}\times\boldsymbol{B}$. If $\boldsymbol{B}_0 = (0, 0, B_0)$ and $\nabla_\perp\boldsymbol{B}$ is in the y direction, the Lorentz force in the y direction F_{Ly} and the magnetic field strength at the guiding center $\boldsymbol{B}$ are given by,

$$F_{Ly} = -qv_xB = -qv_\perp \cos(\Omega t)\,\boldsymbol{B} \tag{2.13}$$

$$\boldsymbol{B} = \boldsymbol{B}_0 \pm \frac{\partial \boldsymbol{B}}{\partial y} r_L \cos(\Omega t) \tag{2.14}$$

where, the signs indicate cases for ion and electron. The averaged Lorentz force during one cycle of the Larmor motion $\langle F_{Ly}\rangle$ is given by,

$$\langle F_{Ly}\rangle = \mp\frac{1}{2}\frac{\partial \boldsymbol{B}}{\partial y} q v_\perp r_L \tag{2.15}$$

The drift velocity by $\langle F_{Ly}\rangle$ can be obtained from Eqs. (2.9) and (2.15). The drift velocity $v_{\nabla B}$ under the general condition of the inhomogeneous magnetic field is given by,

$$\boldsymbol{v}_{\nabla B} = \pm\frac{mv_\perp^2/2}{qB^2}(\boldsymbol{b}\times\nabla\boldsymbol{B}) \tag{2.16}$$

The drift velocity $v_{\nabla B}$ are called ∇B drift velocity. The particle crosses the field line by the ∇B drift motion. In the ∇B drift motion, the ion and the electron move in the opposite directions each other.

c) Curvature drift

Here, we explain the drift motion if the magnetic field line curves. In this situation, the centrifugal force acts on the particle moving with $v_\parallel$ due to the curvature of the field line. The centrifugal force $\boldsymbol{F}_\mathrm{c}$ is given by,

$$\boldsymbol{F}_\mathrm{c} = mv_\parallel^2 \frac{\boldsymbol{R}_\mathrm{c}}{R_\mathrm{c}^2} \tag{2.17}$$

where, R_c is the curvature radius of the field line. The drift velocity $\boldsymbol{v}_c$ by this centrifugal force $\boldsymbol{F}_c$ can be obtained by substitution of Eq. (2.17) into Eq. (2.9).

$$\boldsymbol{v}_c = \frac{mv_\parallel^2}{qB^2}\frac{\boldsymbol{R}_c \times \boldsymbol{B}}{R_c^2} \tag{2.18}$$

$\boldsymbol{v}_c$ is called curvature drift velocity. Here, we define a minute length along the magnetic field line δl_m as

$$\delta l_m = -R_c\, \delta b \tag{2.19}$$

The change of the magnetic field strength δB in the distance of δl_m is given by,

$$\frac{\delta B}{B} = \delta b = -\frac{\delta l_m}{R_c} \tag{2.20}$$

The curvature drift velocity $\boldsymbol{v}_c$ of Eq. (2.18) can be replaced by,

$$\boldsymbol{v}_c = \frac{mv_\parallel^2}{qB^2}(\boldsymbol{b} \times \nabla \boldsymbol{B}) \tag{2.21}$$

In the curvature drift motion, the ion and the electron move in the opposite directions each other.

2.1.3. Magnetic mirror

Here, we explain motions of the charged particles if the magnetic field strength $\boldsymbol{B}$ is inhomogeneous in the parallel direction to the magnetic field line, or $\nabla \boldsymbol{B} \parallel \boldsymbol{B}$. In this situation, the pitch angle is changed by a change of $\boldsymbol{B}$. If I is a loop current and S is an area of the loop, the magnetic moment μ_m is given by,

$$\mu_m = IS \tag{2.22}$$

In the case of the Larmor motion, $I = q\Omega/2\pi$ and $S = \pi r_L^2$. Then, the magnetic moment μ_m can be described by,

$$\mu_m = \frac{mv_\perp^2}{2B} \tag{2.23}$$

The magnetic moment μ_m is conserved when $|\partial B/\partial t| \ll |\Omega B|$. The energy conservation of the particle is expressed as,

$$E = \frac{mv_\perp^2}{2} + \frac{mv_{||}^2}{2} = \text{Const.} \tag{2.24}$$

Substituting Eq. (2.23) into Eq. (2.24) yields,

$$v_\parallel = \pm\sqrt{v^2 - \frac{2}{m}\mu_m B} \tag{2.25}$$

Equation (2.25) indicates that $|v_\parallel|$ decreases (/increases) when $|B|$ becomes higher (/lower). Namely, $\nabla \boldsymbol{B}$ reflects the charged particle when $|B|$ becomes sufficiently high. This magnetic structure is called the

magnetic mirror. The condition for the reflection of the particle by the magnetic mirror is given by,

$$B_{\mathrm{ref}} = \frac{B}{\sin^2 \phi_{\mathrm{pitch}}} \tag{2.26}$$

where, B_{ref} is the magnetic field strength at the reflection position and ϕ_{pitch} is the pitch angle of the particle ($\phi_{\mathrm{pitch}} = \sin^{-1}(v_\perp/v)$). The charged particle is reflected when the magnetic field strength B is higher than B_{ref}. In the inhomogeneous magnetic field, the ∇B drift of Eq. (2.16), the curvature drift of Eq. (2.21), and the magnetic mirror effect of Eq. (2.25) are superimposed on the Larmor motion of the charged particle.

2.1.4. Collision process of fast ions in the plasma

Here, we explain the collision processes of the fast ions. The fast ions are decelerated and scattered by the Coulomb collisions with the bulk electrons and ions. In general, the density of the fast ions n_{f} is much less than that of the bulk electrons n_{e} and bulk ions n_{i}. In addition, the velocity of the fast ions v_{f} is much lower than the thermal velocity of the bulk electrons and higher than the thermal velocity of the bulk ions since the fast ions that are of our interest in this study have hundreds keV order. Under this condition, the time variation of the energy of the fast ions E_{f} can be expressed by,

$$\frac{dE_{\mathrm{f}}}{dt} = -\frac{E_{\mathrm{f}}}{\tau_{\mathrm{fi}}} - \frac{E_{\mathrm{f}}}{\tau_{\mathrm{fe}}} \tag{2.27}$$

where, τ_{fi} and τ_{fe} are the energy relaxation times for collisions with the bulk ions and the bulk electrons, respectively. These relaxation times are given by [2-4],

$$\tau_{\mathrm{fi}} = \frac{2\pi\varepsilon_0^2 m_{\mathrm{i}} m_{\mathrm{f}} v_{\mathrm{f}}^3}{q_{\mathrm{f}}^2 q_{\mathrm{i}}^2 n_{\mathrm{i}} \ln \Lambda_{\mathrm{C}}} \tag{2.28}$$

$$\tau_{\mathrm{fe}} = \frac{m_{\mathrm{f}}}{m_{\mathrm{e}}} \frac{(2\pi)^{1/2} 3\pi\varepsilon_0^2 m_{\mathrm{e}}^{1/2} {T_{\mathrm{e}}}^{3/2}}{q_{\mathrm{f}}^2 q_{\mathrm{e}}^2 n_{\mathrm{e}} \ln \Lambda_{\mathrm{C}}} \tag{2.29}$$

where, m_{i}, m_{e} and m_{f} are the mass of the bulk ion, the electron and the fast ion, respectively. q_{i}, q_{e} and q_{f} are their electric charges. T_{e} is the bulk electron temperature, ε_0 is the permittivity of vacuum and $\ln \Lambda_{\mathrm{C}}$ is the Coulomb logarithm. The fast ion critical energy E_{cr}, at which the energy flow rates of the fast ions to the bulk electrons and the bulk ions are equal, is defined as [4]:

$$E_{\mathrm{cr}} = 14.8 T_{\mathrm{e}} A_{\mathrm{f}} \left(\frac{1}{n_{\mathrm{e}}} \sum_{\mathrm{s}} \frac{n_{\mathrm{s}} Z_{\mathrm{s}}^2}{A_{\mathrm{s}}} \right)^{2/3} \tag{2.30}$$

where, A_{f} is the atomic weight for the fast ion. Here, the subscription of s is the ion species. n_{s}, A_{s} and Z_{s} are the density, the atomic weight and the electric charge number for the ions, respectively. The energy flow rate of the fast ion to the bulk electrons is higher (/lower) than that to the bulk ions when $E_{\mathrm{f}} > E_{\mathrm{cr}}$ ($/E_{\mathrm{f}} < E_{\mathrm{cr}}$). The pitch angle of the fast ion is changed little by the collisions with the bulk electrons because of $m_{\mathrm{f}} \gg m_{\mathrm{e}}$. On the other hand, the pitch angle is scattered by the collisions with the bulk ions because the fast ion mass m_{f} is a similar value to the bulk ion mass m_{i}. In the case of $E_{\mathrm{f}} > E_{\mathrm{cr}}$, a slowing-down time of the fast ion τ_{s} is given by,

$$\tau_s = \int_{E_{cr}}^{E_f} -\frac{1}{(dE/dt)} dE = \frac{\tau_{fe}}{1.5} \ln\left\{1 + \left(\frac{E_f}{E_{cr}}\right)^{3/2}\right\} \tag{2.31}$$

After the time scale of τ_s elapses, the fast ions are sufficiently slowed down. The velocity distribution of the fast ions becomes stationary (called slowing-down distribution) if the fast ions continue to be supplied and the time scale of τ_s elapses.

2.2. Plasma confinement in the tokamak device

Here, we explain the concept for the plasma confinement in the tokamak device. Forming a toroidal structure of the magnetic field lines, a torus-shaped device magnetically confines the plasma. Figure 2.1 shows the schematic drawing of the torus device with only the toroidal magnetic field B_φ. The circumferential directions of the torus device and of its cross section are called the toroidal and poloidal direction, respectively. Distances from the axis of the torus device and from the plasma axis are called the major radius R and the minor radius r, respectively. The vertical coordinate is called Z. The charged particles are confined in the perpendicular direction to the magnetic field line due to the Larmor motion, and also confined in the parallel direction because the particles loop along the closed field line. However, a drastic diffusion of the particles occurs due to the $E \times B$ drift originating from charge separations of the plasma if the magnetic field consists of only the toroidal field B_φ as shown in Fig. 2.1.

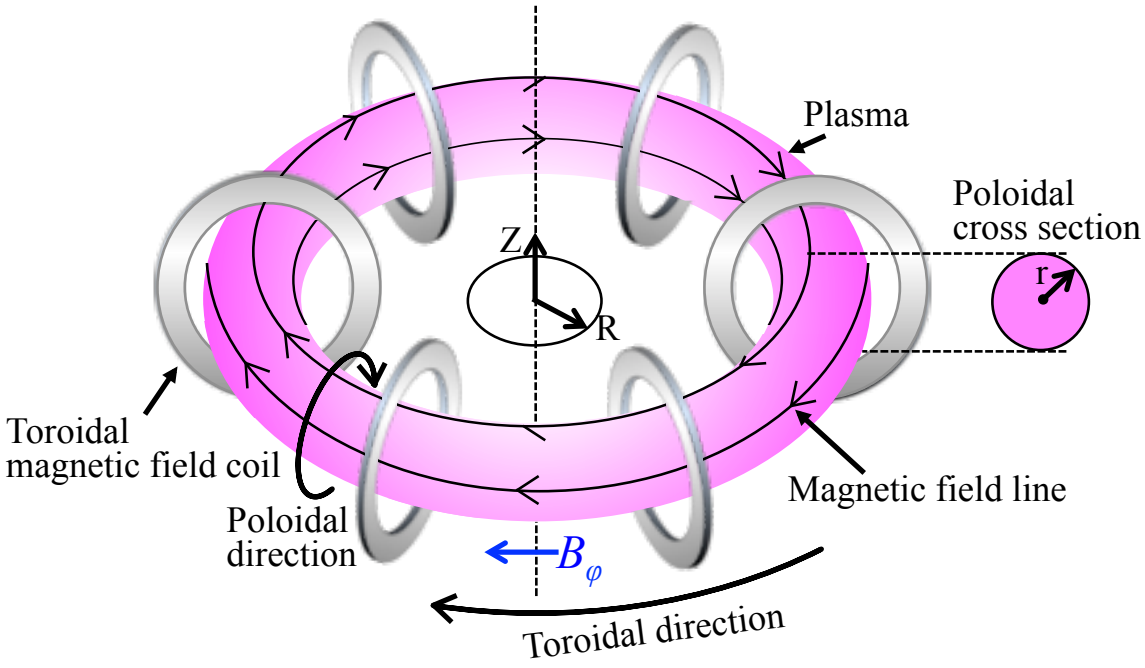

Figure 2.1. A schematic drawing of the torus device with only toroidal magnetic fields B_φ.

2.2.1. Electric charge separation in the torus device

In the torus plasma, ∇B in the opposite direction to R exists because the toroidal magnetic field coils are

relatively close on the small R side than those on the large R side. Therefore, the toroidal magnetic field strength is inversely proportional to R. Here, the sides, at which the toroidal magnetic field strengths are higher and lower than that at the plasma center, are called high field side and low field side, respectively (see Fig. 1.1). In addition, the toroidal magnetic field lines have curvatures. Hence, ions (/electrons) in the plasma move in the lower (/upper) directions of the device due to the ∇B drift and the curvature drift as shown in Fig. 2.2(a). As a result, the charge separation occurs and the electric field E is formed in the upper direction of the device. Then, the ions and the electrons move toward outside the plasma due to the $E \times B$ drift originating from the formed electric field E and the toroidal magnetic field B_φ as shown in Fig. 2.2(b). Hence, the plasma cannot be confined by only the toroidal magnetic field B_φ.

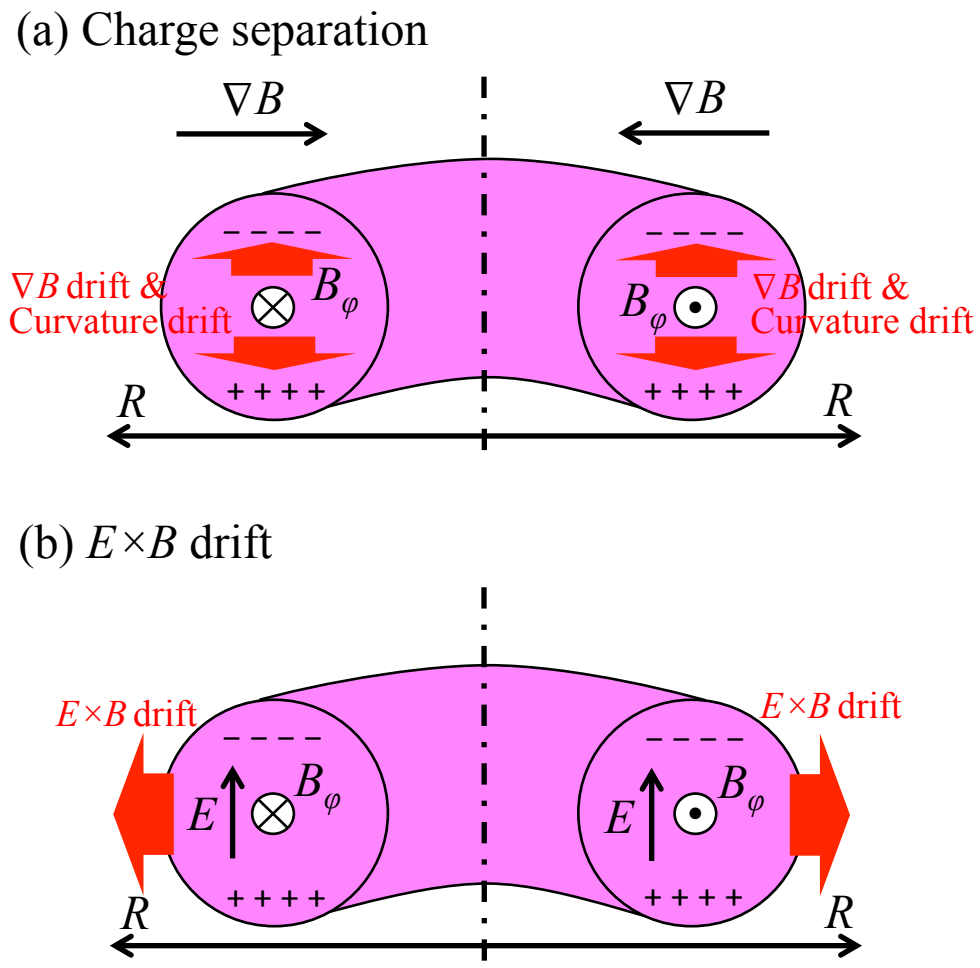

Figure 2.2. Schematic drawings of occurrence processes of (a) the charge separation and (b) the $E \times B$ drift in the torus plasma.

2.2.2. Tokamak

A tokamak device is one of the torus devices for the magnetic plasma confinement [5]. In the tokamak plasma, a plasma current I_p is flowed in the toroidal direction to suppress the charge separation. Figure 2.3 shows the schematic drawing of the tokamak device. The plasma current produces the magnetic field in the

poloidal direction B_θ. The poloidal magnetic field B_θ twists the field lines and magnetic flux surfaces are formed. The separated charges are spatially homogenized by the formation of the flux surface. Therefore, the charge separation is suppressed. The torsion of the magnetic field line is defined as a safety factor $q_{\mathrm{safe}} = rB_\varphi / R_{\mathrm{axis}} B_\theta$, where R_{axis} is R at the plasma axis. The safety factor q_{safe} is an indicator of the stability of the plasma.

As we mentioned in Section 1.2, the tokamak is the most promising magnetic fusion device. The high performance plasma with $Q > 1$ has been almost produced in the tokamak device so far [6, 7]. The tokamak method is adopted for ITER [8]. To achieve the generation of the high fusion power and sustain the high fusion reaction rate, the fast ions, which are produced by the fusion reaction and play the role of the heating of the plasma, must be efficiently confined in the plasma as we mentioned in Section 1.3. Orbits of the fast ions can be different from the flux surface due to their high speeds. Hence, considering the orbits of the fast ions is important to understand their behaviors in the plasma. In the next section, we explain orbits of the fast ions in the tokamak.

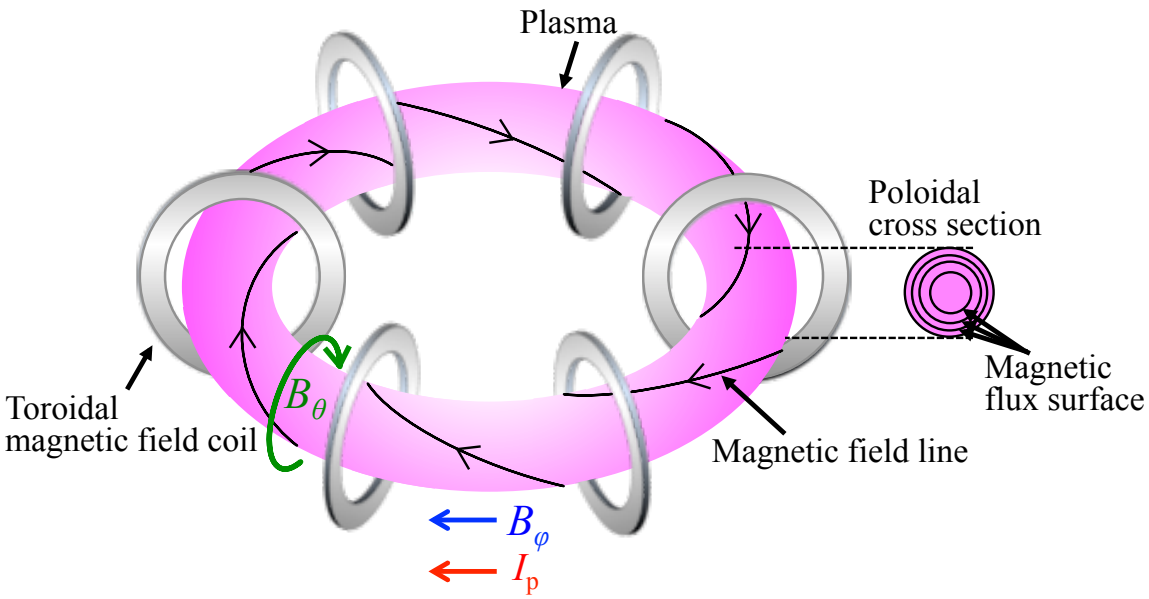

Figure 2.3. A schematic drawing of the tokamak device. B_φ and B_θ are the toroidal and the poloidal magnetic fields, respectively. I_p is the plasma current.

2.2.3. Orbits of fast ions in the tokamak

As we mentioned in Section 2.1.3, the magnetic mirror effect acts on the motion of the charged particles in the tokamak plasma because of the un-uniformity of the toroidal magnetic field. The guiding-center orbits can be categorized into the following two types: a passing orbit and a trapped orbit. Figure 2.4 shows the schematic drawing of (a) the passing orbit and (b) the trapped orbit. The particles can circulate in both toroidal and poloidal directions when they have sufficiently higher $v_\parallel$ than $v_\perp$ as shown in Fig. 2.4(a). In this case, the particles are called passing particles. On the other hand, the particles cannot circulate in the poloidal direction when they have relatively low $v_\parallel$ as shown in Fig. 2.4(b). This is because the magnetic mirror formed by ∇B of the toroidal magnetic field can reflect the particles. In this situation, the particles

are trapped in the large R region and are called trapped particles. The trapped orbit is also called banana orbit from its orbit shape on the poloidal cross section.

If the plasma is axisymmetric and $|B_\varphi| \gg |B_\theta|$, the distances of the passing and trapped orbits from the flux surface at the midplane are given by [1],

$$\begin{aligned} \Delta_\mathrm{p} &= \sim r_\mathrm{L} q_\mathrm{safe} \\ \Delta_\mathrm{t} &= \sim r_\mathrm{L} q_\mathrm{safe} \frac{R_\mathrm{axis}}{r} \end{aligned} \tag{2.32}$$

where, Δ_p and Δ_t are the distances of the passing orbits and the trapped orbits from the flux surfaces, respectively. These distances become large when the energies of the particles increase because r_L becomes large. Namely, the orbits of the fast ions are different from the flux surface due to their high speeds. Note that Δ_t is larger than Δ_p because $R_\mathrm{axis} > r$, i.e., the fast ions can draw the trapped orbits which greatly differ from the flux surface. On the other hand, in general, the particles having the thermal energy order can be approximated to move on the flux surface because r_L is small.

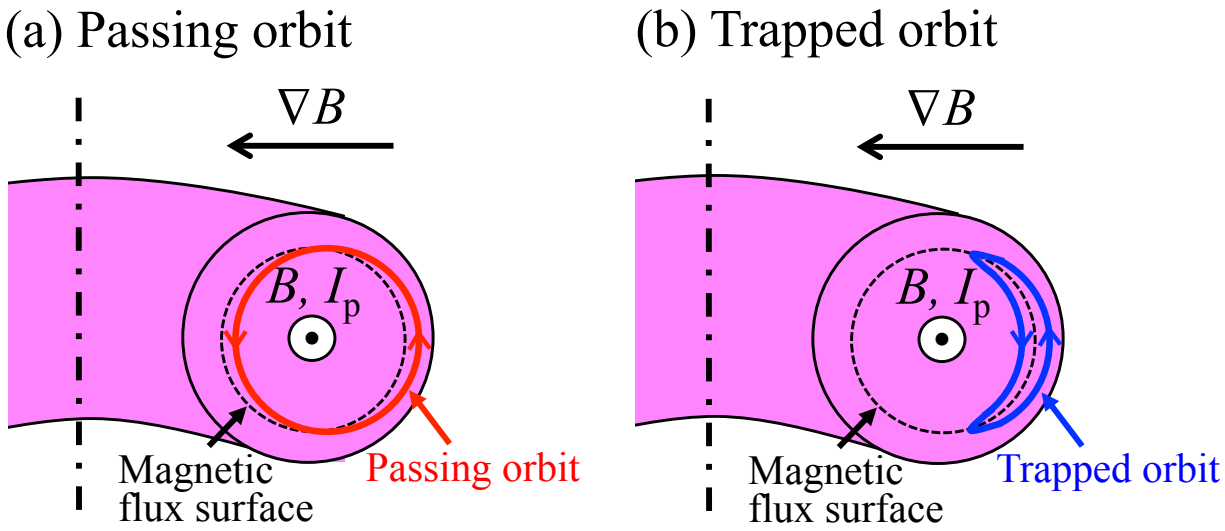

Figure 2.4. Schematic drawings of (a) a passing orbit and (b) a trapped orbit on the poloidal cross section of the tokamak plasma. A toroidal velocity of the passing particle is in the same directions as B_φ and I_p. The toroidal velocity of the trapped particle on an outer (/inner) part of the trapped orbit is in the same (/opposite) direction.

Here, the formation processes for non-thermal ion velocity distribution (the bump-on-tail structure and the pitch-angle anisotropy) near the plasma edge on the low field side in the tokamak device are explained. Figure 2.5 shows differences of guiding-center orbits of fast ^{3}He ions (a) in the energy and (b) in the pitch angle. These orbits are away from the magnetic flux surface. The fast ^{3}He ions can draw the large banana orbits from the region near the plasma center to the plasma edge on the low field side. The ^{3}He ions are produced mainly near the plasma center. Therefore, the large number of the fast ^{3}He ions produced near the plasma center can reach the plasma edge on the low field side. The trapped-orbits scale becomes small as the energy decreases as shown in Fig 2.5(a). The fast ^{3}He ion cannot reach the plasma edge when the scale of the banana orbit becomes small as the energy is decreased. Then, the number of relatively high-energy fast ^{3}He

ions is larger than that of the relatively low-energy fast ^{3}He ions near the plasma edge on the low field side. As a result, the fast ^{3}He ion distribution can have a positive gradient in the energy direction (the bump-on-tail structure). In addition, the orbit style strongly depends on the pitch angle as shown in Fig 2.5(b). The fast ^{3}He ion can draw the largest banana orbit when the pitch angle is near the boundary of the passing and banana orbits. Therefore, the number of the fast ^{3}He ions having the pitch angle near the boundary of the passing and banana orbits is relatively large near the plasma edge on the low field side. As a result, the fast ^{3}He ion distribution can have the strong anisotropy near the plasma edge on the low field side.

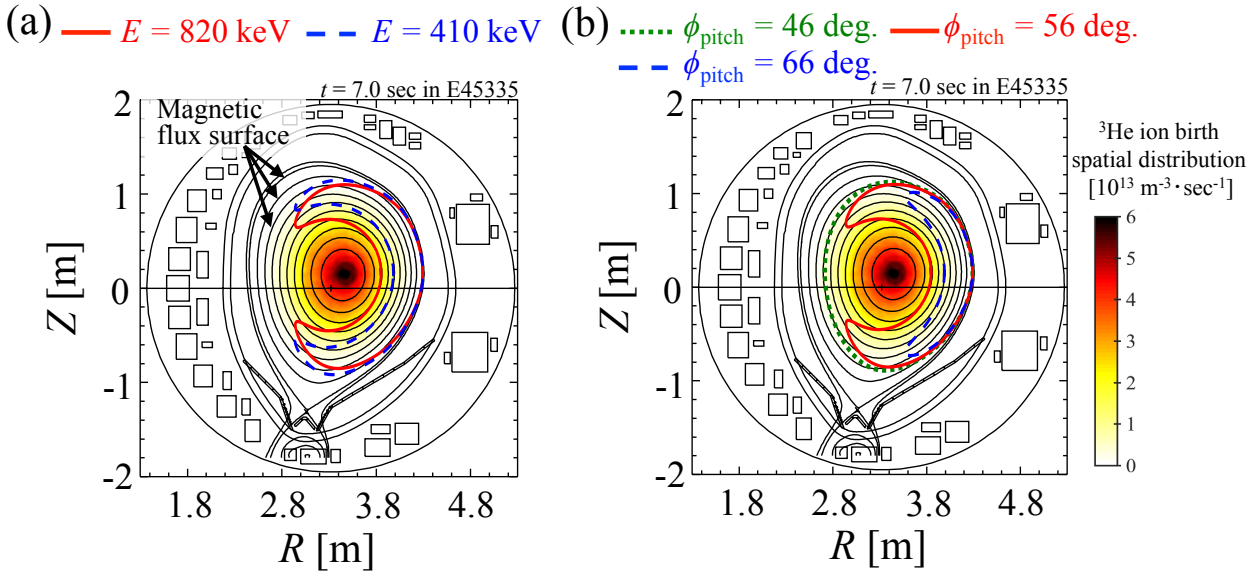

Figure 2.5. Guiding-center orbits of fast ^{3}He ions having (a) the energy E = 820 (solid line) and 420 keV (dashed line) and the pitch angle ϕ_{pitch} = 56 degree, and (b) E = 820 keV and ϕ_{pitch} = 46 (dotted line), 56 (solid line), and 66 (dashed line) degrees on the poloidal cross section in JT-60U. These pitch angles shown are values at the midplane edge of the plasma on the low field side. Black closed curves indicate the magnetic flux surfaces. Color maps are ^{3}He ion birth spatial distributions.

The toroidal magnetic field is strictly non-axisymmetric because the number of the toroidal magnetic field coils is finite. Variations of the magnetic field strength in the toroidal direction are called toroidal magnetic field ripples. The field ripples affect the fast ion orbits, and promote their transports as follows: i) ripple-trapping transport, ii) ripple-plateau transport and iii) banana-drift transport [9]. These transports deteriorate the confinement of the fast ions and lead to damage to the wall due to the fast ion loss.

i) Some charged particles are trapped between the ripple structures. The particle trapped between the ripple structure drifts with $v_d \sim r_{\mathrm{L}} v/R$ in the perpendicular direction to the magnetic field line due to the gradient of the toroidal magnetic field strength. The transport coefficient of the ripple-trapping transport D_{rt} is given by [10],

$$D_{\mathrm{rt}} \sim \frac{\delta_{\mathrm{r}}^{3/2} r_{\mathrm{L}}^2 v^2}{R^2 \nu_{\mathrm{c}}} \tag{2.33}$$

where, δ_{r} is the normalized ripple strength in the toroidal direction and ν_{c} is the collisional frequency.

ii) The field ripple also effectively changes the reflection point of the banana orbit (called a banana tip)

because a staying time at the banana tip is relatively long. If the collision with the bulk ion sufficiently frequently occurs, the collision can randomly change the orbit position at the banana tip, and its change can be regarded as random walk. The transport coefficient of the ripple-plateau transport D_{rp} is given by [11],

$$D_{\mathrm{rp}} \sim \frac{\delta_{\mathrm{r}}^2 r_{\mathrm{L}}^2 \nu q^2 N_{\mathrm{t}}}{R\epsilon_{\mathrm{r}}^2} \tag{2.34}$$

where, N_{t} is the number of the toroidal field coils, and ϵ_{r} is the normalized ripple strength in the poloidal direction. D_{rp} does not depend on the collisional frequency.

iii) If the collision seldom occurs, the particle can draw a closed orbit. Its transport coefficient is in proportional to the collisional frequency [12]. Therefore, the banana-drift transport is important rather than the ripple-plateau transport because the collision frequency of the fast ions with the bulk ions is relatively low due to its high speed.

2.3. Waves in the magnetized plasma

Here, we explain the wave equation in the ICRF in uniform magnetized plasma [1]. The electric flux density $\boldsymbol{D}$ is given by,

$$\boldsymbol{D} = \boldsymbol{\varepsilon} \cdot \boldsymbol{E} = \varepsilon_0 \boldsymbol{E} + \boldsymbol{P} \tag{2.35}$$

where $\boldsymbol{\varepsilon}$ is dielectric tensor, $\boldsymbol{E}$ is the electric field and $\boldsymbol{P}$ is the electric polarization. The Maxwell's equations are given by,

$$\nabla \times \boldsymbol{B} = \frac{\partial \boldsymbol{D}}{\partial t} \tag{2.36}$$

$$\nabla \times \boldsymbol{E} = -\frac{\partial \boldsymbol{B}}{\partial t} \tag{2.37}$$

Here, the electric field of the wave $\boldsymbol{E}$ is assumed to be given as $\boldsymbol{E} \propto \exp\{i(\boldsymbol{k} \cdot \boldsymbol{r} - \omega t)\}$, where $\boldsymbol{k}$ is the wavenumber, $\boldsymbol{r}$ is the space coordinates and ω is the wave angular frequency. In addition, we assumed the first-order quantities of the perturbation. Then, we can obtain the following wave equation under the linear approximation:

$$\boldsymbol{k} \times (\boldsymbol{k} \times \boldsymbol{E}) + \frac{\omega^2}{c^2} \boldsymbol{\varepsilon} \cdot \boldsymbol{E} = 0 \tag{2.38}$$

The current density $\boldsymbol{j}$ is given by,

$$\boldsymbol{j} = \sum_s q_s \int \boldsymbol{v} f(\boldsymbol{v}) d^3 \boldsymbol{v} = -i\omega \boldsymbol{P} \tag{2.39}$$

where, the subscription of s is the charged particle species and $f(\boldsymbol{v})$ is the arbitrary velocity distribution function. The general Vlasov equation is given by,

$$\frac{\partial f_s}{\partial t} + \boldsymbol{v}_s \cdot \nabla f_s + \frac{q_{\mathrm{s}}}{m_{\mathrm{s}}} (\boldsymbol{E} + \boldsymbol{v} \times \boldsymbol{B})_s \frac{\partial f_s}{\partial v_s} = 0 \tag{2.40}$$

Here, we define the velocity distribution f_s as $f_s = f_{s0} + f_{s1}$ and the magnetic field $\boldsymbol{B}$ as $\boldsymbol{B} = \boldsymbol{B}_0 + \boldsymbol{B}_1$, where the subscriptions of 0 and 1 are the zero-order and the first-order (the time-perturbation) components, respectively. The Vlasov equation can be linearized by substitution of $f_s = f_{s0} + f_{s1}$ and $\boldsymbol{B} = \boldsymbol{B}_0 + \boldsymbol{B}_1$ into Eq. (2.40).

$$\frac{\partial f_{s1}}{\partial t} + \boldsymbol{v}_s \cdot \nabla f_{s1} + \frac{q_s}{m_s} \boldsymbol{v} \times \boldsymbol{B}_0 \frac{\partial f_{s1}}{\partial t} + \frac{q_s}{m_s} (\boldsymbol{E} + \boldsymbol{v} \times \boldsymbol{B}_1) \frac{\partial f_{s0}}{\partial t} = 0 \tag{2.41}$$

From Eqs. (2.35), (2.38), (2.39) and (2.41), the dielectric tensor $\boldsymbol{\varepsilon}$ in the uniform plasma can be obtained as,

$$\varepsilon_{i,j} = \delta_{i,j} \left(1 - \sum_s \frac{\omega_{\mathrm{ps}}^2}{\omega^2} \right) + \sum_{s,l} \frac{\omega_{\mathrm{ps}}^2}{\omega^2} \int \frac{\left[\boldsymbol{\Lambda}_{s,l} \right]_{i,j}}{\omega - k_\parallel v_\parallel - l\Omega_s} \left(\frac{l\Omega_s}{v_\perp} \frac{\partial f_{s0}}{\partial v_\perp} + k_\parallel \frac{\partial f_{s0}}{\partial v_\parallel} \right) \frac{1}{n_s} d^3 v \tag{2.42}$$

$$\boldsymbol{\Lambda}_{s,l} = \begin{bmatrix} \frac{l^2 \Omega_s^2}{k_\perp^2} J_l^2 & i v_\perp \frac{l\Omega_s}{k_\perp} J_l J_l' & v_\parallel \frac{l\Omega_s}{k_\perp} J_l^2 \\ -i v_\perp \frac{l\Omega_s}{k_\perp} J_l J_l' & v_\perp^2 J_l'^2 & -i v_\parallel v_\perp J_l J_l' \\ v_\parallel \frac{l\Omega_s}{k_\perp} J_l^2 & i v_\parallel v_\perp J_l J_l' & v_\parallel^2 J_l^2 \end{bmatrix} \tag{2.43}$$

where l is the integer, and n_s is the density. $\omega_{\mathrm{ps}} = \sqrt{n_{\mathrm{e}} q_{\mathrm{e}}^2 / \varepsilon_0 m_{\mathrm{e}}}$ is the plasma angular frequency. $k_\perp$ and $k_\parallel$ are the wavenumbers in perpendicular and parallel directions to the magnetic field line, respectively. J_l is the Bessel function with the argument $k_\perp v_\perp / \Omega_s$, and J_l' is its first derivative. The cyclotron resonance, which is one of strong wave-particle interactions, occurs when the Doppler-shifted cyclotron resonance condition is satisfied as follows.

$$\omega - k_\parallel v_\parallel - l\Omega_s = 0 \tag{2.44}$$

The term of $k_\parallel v_\parallel$ is the Doppler shift. The energies are exchanged between the waves and the particles by the cyclotron resonance under the above condition. The particles stabilize (/ destabilize) the waves when the particles are accelerated (/decelerated) by the waves.

References in Chapter 2

[1] K. Miyamoto, *Plasma Physics and Controlled Nuclear Fusion,* Springer, New York (2005).

[2] D.V. Sivukhin, *Reviews of Plasma Physics (ed. by M. A. Leontovich)*, Consultant Bureau, New York (1996).

[3] K. Miyamoto, *Plasma Physics for Nuclear Fusion (Revised Edition)*, The MIT Press, Cambridge, Mass. (1989).

[4] T. H. Stix, Plasma Phys. **14**, 367 (1972).

[5] L. A. Arsimovitch, Nucl. Fusion **12**, 215 (1972).

[6] JET Team, Nucl. Fusion **32**, 187 (1992).

[7] T. Fujita *et al.*, Nucl. Fusion **39**, 1627 (1999).

[8] R. Aymar *et al.*, Plasma Phys. Control. Fusion **44**, 519 (2002).

[9] J. Wesson, *Tokamaks*, Oxford University Press, Oxford (1987).

[10] T. E. Stringer, Nucl. Fusion **12**, 689 (1972).

[11] A. H. Boozer, Phys. Fluids **23**, 2283 (1980).

[12] R. J. Goldston and H. H. Tower, J. Plasma Phys. **26**, 283 (1981).

Chapter 3
Experiments on JT-60U

In this chapter, experimental apparatus and an observation result of the ICEs on JT-60U are described. First, a brief outline of JT-60U is introduced. Then, heating systems and measurement equipment used for the experiments analyzed in this study are explained. Finally, an observation result of the ICEs in the typical D plasma experiment on JT-60U is introduced.

3.1. JT-60 / JT-60U

JT-60 / JT-60U is the largest tokamak device in Japan [1, 2]. JT-60U is an upgraded version of JT-60 [2]. The vacuum vessel is expanded in JT-60U so as to be able to flow larger plasma currents than that in JT-60. Figure 3.1 shows a schematic drawing of JT-60U [3]. JT-60U has several types of plasma heating and current drive systems: NB injection [4], ion cyclotron heating (ICH) [5], electron cyclotron heating and current drive (ECH and ECCD) [6] and lower hybrid current drive (LHCD) [7]. The ICH, ECH / ECCD and LHCD are classified as radio frequency (RF) wave heating and current drive system. Main parameters of JT-60U are as follows [8]: the toroidal magnetic field is 4 T, the plasma current is 3 MA, the major radius is 3.4 m, the minor radius is 1 m, the plasma volume is 90 m^3, the pulse length of the discharge is 65 sec, the heating power of the NB injection is 40 MW, and the heating power of the RF wave heating and current drive system is 15 MW. The material of its first wall is carbon. Ferritic steel tiles are installed on the wall to reduce the toroidal magnetic field ripples [9]. In JT-60U, the D plasma experiments have been implemented. The high performance plasma, which is equivalent to $Q \sim 1.25$, has been already produced in JT-60U [10].

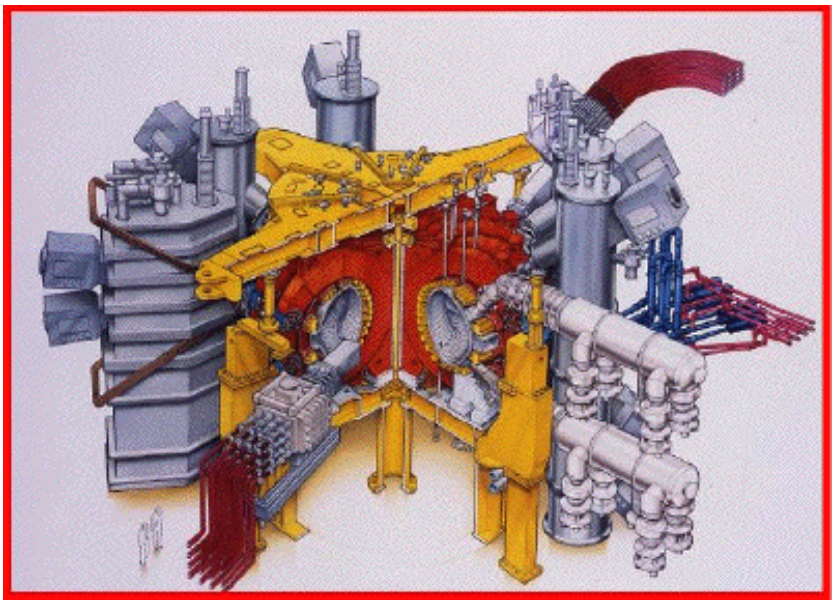

Figure 3.1. A bird's-eye view of JT-60U (cited from Ref. [3]).

3.2. Heating system

a) Neutral beam (NB) injection

The NB injection is one of the methods to heat the plasma by injecting the fast atoms from the region outside the plasma. A ratio of the fast ions in the bulk plasma increases as the injected fast atoms exchange the electric charge with the bulk ions by charge exchange reactions and ionization reactions. The charge exchange reaction between fast D atom and slow D ion is given by,

$$D^0_{\text{fast}} + D^+_{\text{slow}} \rightarrow D^+_{\text{fast}} + D^0_{\text{slow}} \tag{3.1}$$

where, the subscriptions of "fast" and "slow" indicate the ion velocity. The superscriptions of "0" and "+" indicate neutral atom and ion, respectively. The ionizations reaction is given by,

$$D^0_{\text{fast}} + D^+_{\text{slow}} \rightarrow D^+_{\text{fast}} + D^+_{\text{slow}} + e^- \tag{3.2}$$

where e^- is electron. The number of the fast ions increases in the plasma after the charge exchange reaction and the ionization reaction in the case of the NB injection. Then, the fast ions heat the bulk plasma via the collisions. Therefore, the NB injection can heat the plasma. In addition, the NBs in the tangential direction to the toroidal magnetic field are also used for the current drive in the plasma [11].

Figure 3.2 shows the schematic drawing of the NB systems on JT-60U. There are positive-ion sourced NBs (P-NBs) and negative-ion sourced NBs (N-NBs) on JT-60U [4]. The P-NBs consist of almost tangential beams and perpendicular beams to the toroidal magnetic field. The tangential P-NBs in co-current (CO) and counter-current (CTR) directions are installed. The perpendicular P-NB injections are slightly tilted in CO and CTR directions. Acceleration voltages of the P-NB and the N-NB are ~85 kV and ~350 kV, respectively. Usually, the P-NB and the N-NB mainly heat the bulk ions and the bulk electrons, respectively. This is because the birth energies of the fast ions originating from the P-NB and the N-NB injections are lower and higher than E_{cr}, respectively.

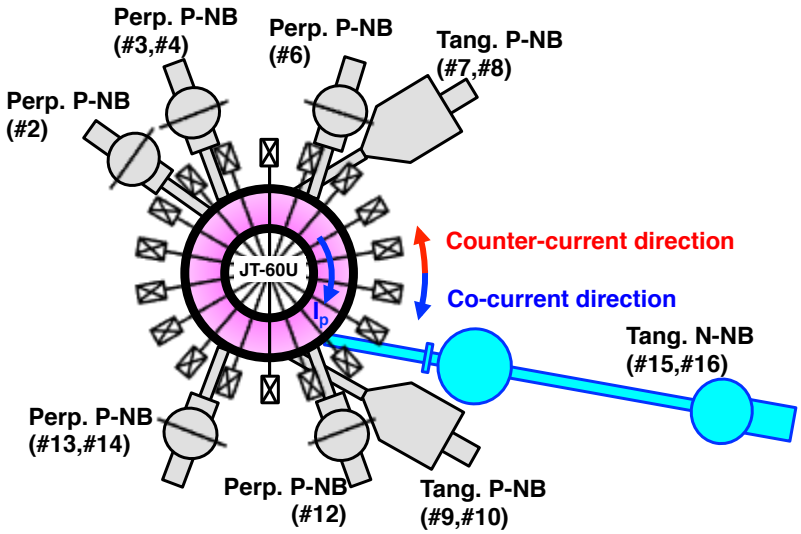

Figure 3.2. A schematic drawing of the NB systems on JT-60U. Positive-ion sourced NBs (P-NBs) and negative-ion sourced NBs (N-NB) are installed.

b) Ion cyclotron heating (ICH)

The ICH is one of the methods to heat the plasma. Ions in the magnetic field are resonantly accelerated with the electric fields of the ICRF waves. Its resonance condition is the ion cyclotron resonance of Eq. (2.44). Accelerated fast ions heat the plasma via the collisions. Usually, the ICRF waves are excited from the antenna installed near the plasma surface. Figure 3.3 shows the schematic drawing of the ICRF antenna straps on JT-60U [12]. These ICRF antennas are installed on the wall on the low field side. The antenna straps are arranged in both toroidal and poloidal directions. The straps are connected to the ground potential at the center of the straps arranged in the poloidal direction. On the other hand, both ends of the straps are connected to the ICRF power supply system.

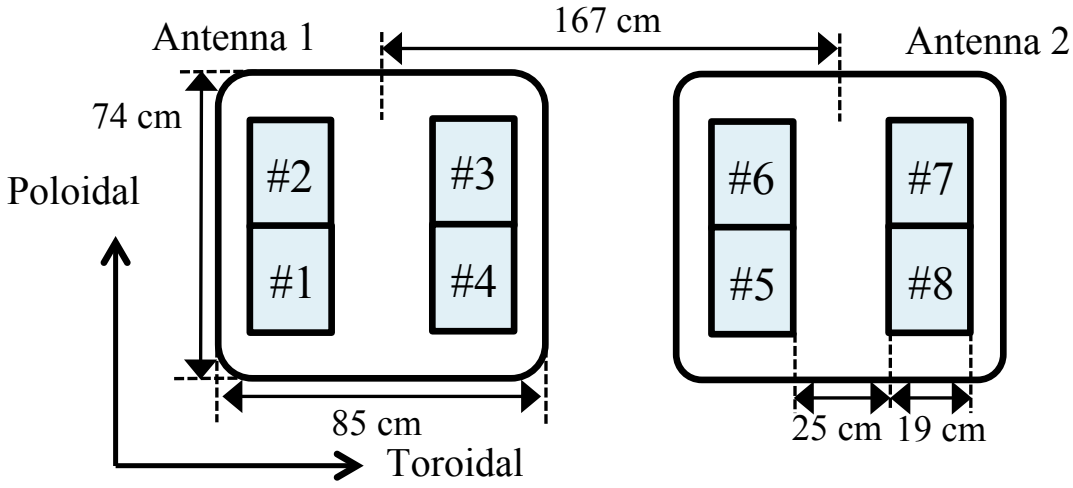

Figure 3.3. A schematic drawing of the ICRF antenna straps on JT-60U. The straps are arranged in both toroidal and poloidal directions.

3.3. Diagnostics

3.3.1. CO_2 laser interferometer

The wavelength of the wave changes when the wave is passing through the plasma because the plasma is a kind of dielectrics. This change of the wavelength depends on the plasma density. Therefore, line-integrated density of the plasma can be measured by using a microwave interferometer.

The dielectric of the plasma ε in the frequency range of the microwave is given by,

$$\varepsilon = 1 - \frac{\omega_{\mathrm{pe}}^2}{\omega^2} \tag{3.3}$$

If $\omega \gg \omega_{\mathrm{pe}}$, the wavelength of the microwave λ is given by,

$$\lambda = \frac{\lambda_0}{\sqrt{\varepsilon}} = \frac{2\pi c}{\omega\sqrt{\varepsilon}} \tag{3.4}$$

where, λ_0 is the wavelength of the microwave in the vacuum and c is the light speed in the vacuum. The phase difference between the microwaves passing through the plasma and only through the vacuum $\Delta\Phi_{\mathrm{p}}$ is given by,

$$\Delta\Phi_{\mathrm{p}} = 2\pi \int_{x_1}^{x_2} \left(\frac{1}{\lambda_0} - \frac{1}{\lambda}\right) dx \tag{3.5}$$

where, x is the space coordinate in the wave propagating direction. x_1 and x_2 are x positions where the microwaves penetrate into the plasma and pass out the plasma, respectively. Substituting Eqs. (3.3) and (3.4) into Eq. (3.5) yields,

$$\Delta\Phi_{\mathrm{p}} \sim \frac{\pi q_{\mathrm{e}}^2}{\varepsilon_0 m_{\mathrm{e}} \lambda_0 \omega^2} \int_{x_1}^{x_2} n_{\mathrm{e}}(x) dx \tag{3.6}$$

Thus, the phase difference of the microwaves indicates the line-integrated electron density.

To measure the line-integrated electron density including the density at the plasma center, an interferometer using a CO_2 laser is used on JT-60U [13]. Its measurement line is shown in Fig. 3.4.

3.3.2. Thomson scattering with ruby laser

The Thomson scattering is an elastic scattering with electrons. The Doppler effect due to the thermal motion of the electrons expands the scattering spectrum. The spectrum density function S_{TS} is given by,

$$S_{\mathrm{TS}}(\zeta) = \sqrt{\frac{m_{\mathrm{e}}c^2}{2\pi T_{\mathrm{e}}}} \frac{1}{\sqrt{2(1-\cos\theta_{\mathrm{TS}})}} \exp\left\{-\frac{m_{\mathrm{e}}c^2\zeta^2}{2T_{\mathrm{e}}\sqrt{2(1-\cos\theta_{\mathrm{TS}})}}\right\}\left(1-\frac{7}{2}\zeta\right) \tag{3.7}$$

where, $\zeta = (\lambda_{\mathrm{TS}} - \lambda_{\mathrm{i}})/\lambda_{\mathrm{i}}$ and θ_{TS} is the Thomson scattering angle. Here, λ_{TS} and λ_{i} are the wavelengths of the scattered light and of the injected light, respectively. T_{e} can be obtained from the spread of S_{TS}. In addition, n_{e} can be also obtained from the intensity of the scattered light since the intensity is proportional to n_{e}.

The Thomson scattering systems using ruby lasers are installed on JT-60U to simultaneously measure spatial profiles of n_e and T_e with high spatial resolutions of about 8~22 mm [14]. Its measurement positions are shown in Fig. 3.4.

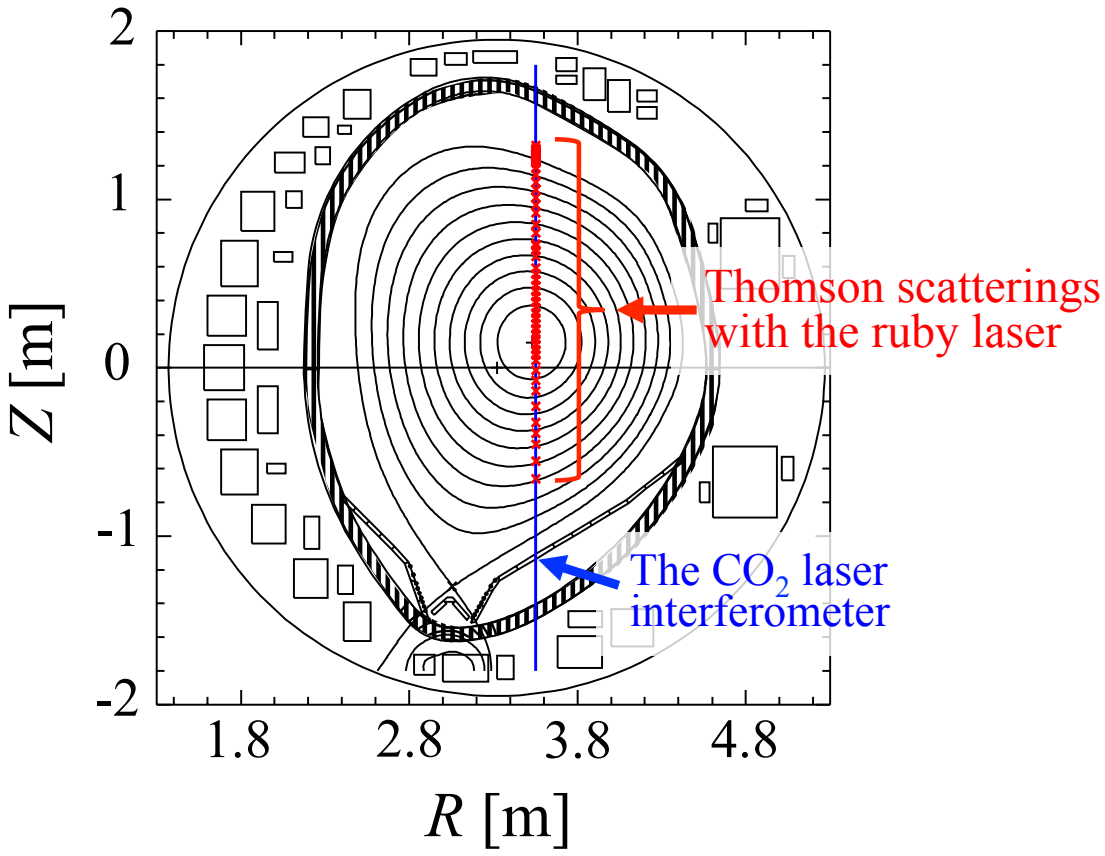

Figure 3.4. A measurement line of the CO_2 laser interferometer for the measurement of the line-integrated electron density including the density at the plasma center (blue line) and measurement positions of the Thomson scattering with the ruby laser (red crosses) on the poloidal cross section on JT-60U.

3.3.3. Diamagnetic loop

A diamagnetic loop is a magnetic coil surrounded the plasma column to detect a temporal change of the magnetic field caused by a diamagnetism of the plasma. The diamagnetism is an indicator of the stored energy (and the pressure) of the plasma. Thus, the diamagnetic loop is often used for the diagnostic of the stored energy.

The pressure balance equation for the magnetized plasma is given by,

$$\langle p \rangle = \frac{B_\theta^2(r_a)}{2\mu_0} + \frac{1}{2\mu_0}\left(B_\varphi^2(r_a) - \langle B_\varphi^2 \rangle\right) \tag{3.8}$$

where, p is the plasma pressure, r_a is the plasma minor radius, and μ_0 is the permeability of the vacuum. < > is a volume-averaged value. The change of the magnetic flux $\Delta\Phi_m$ is given by,

$$\Delta\Phi_{\mathrm{m}} = \pi r_{\mathrm{a}}^2 \langle B_\varphi^2 - B_\varphi^2(r_{\mathrm{a}}) \rangle \tag{3.9}$$

A plasma beta β is defined as a ratio of the plasma pressure to the magnetic pressure $\beta = \langle p \rangle / (B^2/2\mu_0)$. The poloidal beta of the plasma β_θ is given by,

$$\beta_\theta = \frac{\langle p \rangle}{B_\theta^2(r_{\mathrm{a}})/2\mu_0} \tag{3.10}$$

Substituting Eq. (3.8) and Eq. (3.10) into Eq. (3.9) yields,

$$\Delta\Phi_{\mathrm{m}} = (1 - \beta_\theta) \frac{\mu_0^2 I_{\mathrm{p}}^2}{8\pi B_\varphi} \tag{3.11}$$

Thus, the stored energy (and the pressure) of the plasma can be measured using the diamagnetic loop.

Four sets of the diamagnetic loops are installed on JT-60U and used for the measurement of the stored energy of the plasma [15].

3.3.4. ^{235}U fission chamber

A fission chamber is commonly used for a neutron detector. The fission chamber has an ionization chamber and a little amount of fissile materials. The fission reactions occur and high-energy fission fragments are emitted when the neutrons come into the fission chamber and collide with the fissile materials. Then, a thin gas is ionized in the ionization chamber by the fission fragments. Therefore, the neutrons can be detected by measuring the currents from the ionization chamber.

The neutrons having ~2.5 MeV are produced by D(d, n)^{3}He reactions in the D plasma experiments. On JT-60U, ^{235}U fission chambers are installed to measure the total neutron emission rate [16], which is an indicator of the fusion performance in the plasma. The absolute values of the fission chamber signals are calibrated by using a ^{252}Cf neutron source.

3.3.5. ICRF antenna straps

The ICRF antenna straps shown in Fig. 3.3 were also used for the measurement of the ICEs on JT-60U [17-19]. The ICH power was not supplied to the antennas when the antennas were used for the measurements. Signal cables were connected to the transmission cables behind the antenna straps. In this case, antenna-matching components were not connected between the antenna and the signal cables. An oscilloscope was used for recording the measured signals. Its sampling frequency and duration were 500 MHz and 100 μsec, respectively. The signal sampling was repeated at every 50 msec. The toroidal wavenumber of the ICE can be evaluated from the phase difference of the signals between the antenna straps arranged in the toroidal direction. The toroidal wavenumber k_φ is given by,

$$k_\varphi = \frac{\Delta\Phi_\varphi}{\Delta L_\varphi} \tag{3.12}$$

where, $\Delta\Phi_\varphi$ is the phase difference of signals between the antenna straps arranged in the toroidal direction

and ΔL_φ is the distance between the straps. Thus, three antenna straps (#1, #4 and #5) were often simultaneously used. The distance between the centers of the #1 strap and the #4 strap is 0.44 m in the toroidal direction and between the centers of the #4 strap and the #5 strap is 1.23 m.

3.4. Observation of ICEs

On JT-60U, the ICE(D), ICE(^{3}He), ICE(T) and ICE(H) have been observed [17-20]. Figure 3.5 shows the time evolution of the frequency spectrum of electrostatic and/or electromagnetic fluctuations in a typical discharge of E45334 where the ICE(D), ICE(^{3}He) and ICE(T) were observed. These electrostatic and/or electromagnetic fluctuations were measured with the ICRF antenna straps. Dotted, dashed and dotted-dashed lines indicate the cyclotron frequencies for D ion f_{cD}, ^{3}He ion f_{c3He} and T ion f_{cT} at the midplane edge of the plasma on the low field side, respectively. The time sequence of the N-NB, the perpendicular P-NB and the tangential P-NB is shown at the top of the figure. Figure 3.6 shows the time evolution of (a) the plasma current I_{p}, (b) the line-averaged density $\overline{n_{\mathrm{e}}}$, (c) the stored energy of the plasma W_{d} and (d) the total neutron emission rate S_{n} in E45334. $\overline{n_{\mathrm{e}}}$ was measured with the CO_2 laser interferometer of which the measurement line is shown in Fig. 3.4. W_{d} and S_{n} were measured with the diamagnetic loop and the ^{235}U fission chamber, respectively. The fluctuations in the frequencies around lf_{cD} $(l = 1, 2, 3)$ are observed. These fluctuations are the ICE(D) and its harmonics. The fluctuations in the frequencies slightly below $l'f_{\mathrm{c3He}}$ $(l' = 1, 2)$ and f_{cT} appear after S_{n} begins to increase and becomes relatively high, respectively. These fluctuations are interpreted as ICE(^{3}He) and ICE(T), respectively. Time periods of the observations of the ICE(D), ICE(^{3}He) and ICE(T) are clearly different. This would be attributed to the differences in the behaviors of the different fast ions. In this study, we investigated the emission mechanism for the ICE(^{3}He) in terms of the fast ^{3}He ion velocity distribution and the wave dispersion relation as mentioned in Section 1.6.

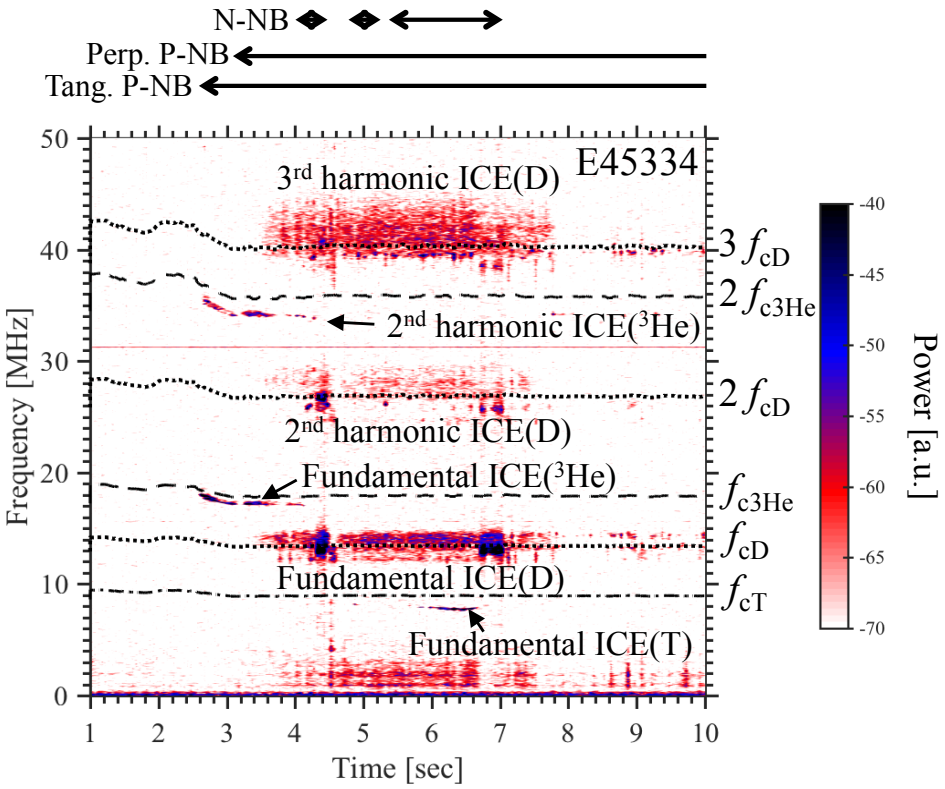

Figure 3.5. Time evolution of the frequency spectrum of the electrostatic and/or electromagnetic fluctuations measured with the ICRF antenna strap in E45334. Dotted, dashed and dotted-dashed lines indicate the cyclotron frequency and its harmonics for D ion, ^{3}He ion and T ion at the midplane edge of the plasma on the low field side, respectively.

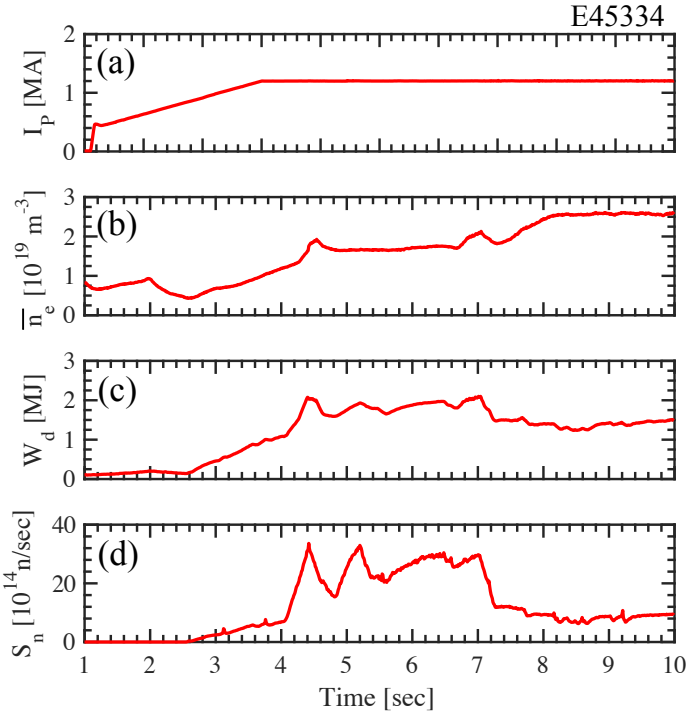

Figure 3.6. Time evolution of (a) the plasma current I_p, (b) the line-averaged density $\overline{n_\mathrm{e}}$, (c) the stored diamagnetic energy of the plasma W_d and (d) the total neutron emission rate S_n in E45334.

References in Chapter 3

[1] S. Ide and the JT-60 Team, Nucl. Fusion **45**, S48 (2005).

[2] H. Shirakata, Fusion Eng. Des. **14**, 7 (1991).

[3] JT-60 HOME PAGE, "http://www-jt60.naka.qst.go.jp/jt60/mecha/html/mecha0.html"

[4] T. Oikawa *et al.*, Nucl. Fusion **41**, 1575 (2001).

[5] H. Kimura *et al.*, Fusion Eng. Des. **26**, 95 (1995).

[6] K. Nagasaki *et al*., Nucl. Fusion **43**, L7 (2003).

[7] S. Ide *et al.,* Plasma Phys. Control. Fusion **38**, 1645 (1996).

[8] JT-60 HOME PAGE, "http://www-jt60.naka.qst.go.jo/english/jt60/project/html/parameter.html"

[9] K. Shinohara *et al*., Nucl. Fusion **47**, 997 (2007).

[10] T. Fujita *et al.*, Nucl. Fusion **39**, 1627 (1999).

[11] T. Ohkawa *et al.*, Nucl. Fusion **10**, 185 (1970).

[12] M. Saigusa *et al.*, Nucl. Fusion **34**, 276 (1994).

[13] Y. Kawano *et al*., Rev. Sci. Instrum. **67**, 1520 (1996).

[14] H. Yoshida *et al*., Rev. Sci. Instrum. **70**, 751 (1999).

[15] Y. Neyatani *et al.*, 14th Symp. On Fusion Eng., Vol.2, 1183 (1991).

[16] T. Nishitani *et al.*, Rev. Sci. Instrum **63**, 5270 (1992).

[17] M. Ichimura *et al.*, Nucl. Fusion **48**, 035012 (2008).

[18] M. Ichimura *et al*., Proc. 22nd IAEA Fusion Energy Conf. (Geneva, Switzerland, 2008) EX/P8-2 (2008).

[19] S. Sato *et al.*, Plasma Fusion Res. **5**, S2067 (2010).

[20] H. Kimura *et al.*, Nucl. Fusion **38**, 1303 (1998).

Chapter 4
Setup for Evaluation of Fast ^{3}He Ion Velocity Distribution

In this chapter, setups for the evaluation of the fast ^{3}He ion velocity distribution with OFMC are described. First, a brief outline of the OFMC is introduced, and its orbit equations and its validity are explained. Then, procedure for the evaluation of the fast ^{3}He ion velocity distribution is explained. Next, influences of a guiding-center approximation on orbit positions are discussed under a typical plasma condition analyzed in this study. Finally, birth energy of the fusion product in the laboratory system is explained toward the more quantitative evaluation of the fast ^{3}He ion distribution.

4.1. OFMC code

OFMC is a fast ion orbit following Monte-Carlo simulation code that has been developed in National Institutes for Quantum and Radiological Science and Technology, Japan [1]. The OFMC can trace the guiding-center orbits and/or the full-gyro orbits of the fast ions in the tokamak plasma. The explicit and implicit 4th order Runge-Kutta methods are used for numerical calculations of the guiding-center and full-gyro orbit equations, respectively. Changes of the orbits due to the collisions with the bulk plasma are treated using the Monte-Carlo method. The orbit calculations can be carried out with parallel computing methods. Three-dimensional magnetic field structure including the toroidal magnetic field ripples and the wall structure can be taken into account. We adopted the OFMC for calculations of the fast ion orbits to evaluate the spatial and velocity distribution of the fast ions.

4.1.1. Orbit equation

a) Guiding-center orbit

The velocity of the fast ion on the guiding-center orbit $\boldsymbol{v}_{\mathrm{g}}$ used in the OFMC is given by,

$$\boldsymbol{v}_{\mathrm{g}} = v_{\parallel}\boldsymbol{b} + \boldsymbol{v}_E + \boldsymbol{v}_{\nabla B} + \boldsymbol{v}_{\mathrm{c}} \tag{4.1}$$

$$\begin{cases} \boldsymbol{v}_E = \dfrac{\boldsymbol{E}\times\boldsymbol{b}}{B} \\ \boldsymbol{v}_B = \dfrac{m}{q}\dfrac{v_{\perp}^2/2}{B^2}(\boldsymbol{b}\times\nabla\boldsymbol{B}) \\ \boldsymbol{v}_{\mathrm{c}} = \dfrac{mv_{\parallel}^2}{qB^2}(\boldsymbol{b}\times\nabla\boldsymbol{B}) \end{cases}$$

The $E\times B$ drift, the ∇B drift and the curvature drift are adopted for the calculation of the guiding-center orbit in the OFMC. In the orbit calculations in this study, we assumed that there is no electric field $\boldsymbol{E}$ since the

energies of the fast ions are sufficiently higher than the electric potential in the plasma. In addition, we assumed that the magnetic field $\boldsymbol{B}$ does not temporally change. Then, the motion equation of the fast ion on the guiding-center orbit in the parallel direction to the magnetic field is given by,

$$\frac{dv_{g\parallel}}{dt} = -\frac{\mu_m}{m}\frac{\partial B}{\partial l_m} \tag{4.2}$$

where, $v_{g\parallel}$ is the parallel velocity of the guiding-center particle. The perpendicular velocity $v_{g\perp}$ is given by,

$$v_{g\perp} = \frac{1}{q}\left(\mu_m + \frac{m}{B}v_{g\parallel}^2\right)\boldsymbol{b}\times\frac{\partial \boldsymbol{b}}{\partial l_m} \tag{4.3}$$

The simultaneous equations in the cylindrical coordinate system (R, Z, φ) are derived from Eqs. (4.1)-(4.3).

$$\begin{cases} \dfrac{dR}{dt} = \dfrac{m}{2q}\left(v_\perp^2 + 2v_\parallel^2\right)\dfrac{1}{B^2}\left(\dfrac{B_\varphi}{B}\dfrac{\partial B}{\partial Z} - \dfrac{B_Z}{B}\dfrac{\partial B}{R\partial\varphi}\right) + \dfrac{B_R}{B}v_\parallel \\ \dfrac{dZ}{dt} = \dfrac{m}{2q}\left(v_\perp^2 + 2v_\parallel^2\right)\dfrac{1}{B^2}\left(\dfrac{B_R}{B}\dfrac{\partial B}{R\partial\varphi} - \dfrac{B_\varphi}{B}\dfrac{\partial B}{\partial R}\right) + \dfrac{B_Z}{B}v_\parallel \\ \dfrac{d\varphi}{dt} = \dfrac{1}{R}\left\{\dfrac{m}{2q}\left(v_\perp^2 + 2v_\parallel^2\right)\dfrac{1}{B^2}\left(\dfrac{B_Z}{B}\dfrac{\partial B}{\partial R} - \dfrac{B_R}{B}\dfrac{\partial B}{\partial Z}\right) + \dfrac{B_\varphi}{B}v_\parallel\right\} \\ \dfrac{dv_\parallel}{dt} = -\dfrac{v_\perp^2}{2B}\dfrac{\partial B}{\partial l_m} \end{cases} \tag{4.4}$$

Solving the above simultaneous equations with the explicit Runge-Kutta method, the OFMC can trace the guiding-center orbits.

b) Full-gyro orbit

The motion equation of the fast ion on the full-gyro orbit used in the OFMC is the same form as Eq. (2.1). If there is no electric field $\boldsymbol{E}$ and the magnetic field $\boldsymbol{B}$ does not temporally change, the motion equations in the R-Z-φ coordinate system are given by,

$$\begin{cases} \dfrac{d\boldsymbol{v}_R}{dt} = \dfrac{q}{m}(\boldsymbol{v}\times\boldsymbol{B})_R + \dfrac{\boldsymbol{v}_\varphi^2}{R} \\ \dfrac{d\boldsymbol{v}_\varphi}{dt} = \dfrac{q}{m}(\boldsymbol{v}\times\boldsymbol{B})_\varphi - \dfrac{\boldsymbol{v}_R\boldsymbol{v}_\varphi}{R} \\ \dfrac{d\boldsymbol{v}_Z}{dt} = \dfrac{q}{m}(\boldsymbol{v}\times\boldsymbol{B})_Z \end{cases} \tag{4.5}$$

where,

$$\begin{cases} \boldsymbol{v}_R = \dfrac{d\boldsymbol{R}}{dt} \\ \dfrac{\boldsymbol{v}_\varphi}{R} = \dfrac{d\boldsymbol{\varphi}}{dt} \\ \boldsymbol{v}_Z = \dfrac{d\boldsymbol{Z}}{dt} \end{cases} \tag{4.6}$$

Solving these equations with the implicit Runge-Kutta method, the full-gyro orbits are traced in the OFMC.

4.1.2. Validation

The OFMC has been validated with several tokamak experiments such as JFT-2M [2], JT-60U [3-5], and DIII-D [6] in terms of heat loads on the wall due to fast ion loss and driven plasma currents by confined fast ions. In addition, the calculation results of the heat loads on DIII-D have been compared between the OFMC and a few fast-ion simulation codes [6]. As the results, it has been confirmed that the calculation results of the OFMC agrees well with those of other codes.

These heat loads and beam driven currents strongly depend on the fast ion spatial and velocity distribution. Namely, the evaluations of the fast ion distribution with the OFMC are considered to be reasonable, although the OFMC is not directly validated with the experiment in terms of the fast ion distribution so far because of the difficulty of its measurement in the experiment.

4.2. Procedure for evaluation of velocity distribution of DD fusion produced fast ^{3}He ions

4.2.1. Flowchart

Although the OFMC is usually used for the orbit calculations of the fast D ions originating from the NB injections, the fast ^{3}He ion orbit calculations are needed in this study. Thus, we newly developed a fast ^{3}He ion orbit calculation system with the OFMC. Birth spatial and velocity distribution of the fast ^{3}He ions is necessary as initial conditions to calculate the fast ^{3}He ion orbits and evaluate their slowing-down distribution. The fast ^{3}He ions are produced by the DD fusion reaction (the D(d, n)^{3}He reaction) of Eq. (1.3b) on JT-60U.

The fusion reaction in the plasma experiments consists of i) a beam-thermal component (fusion reaction between a fast ion originating from the NB injection and an ion in the bulk plasma), ii) a thermal-thermal component (fusion reaction of ions in the bulk plasma) and iii) a beam-beam component (fusion reaction of the fast ions). i) Usually, the beam-thermal fusion reaction rate is dominant in the DD fusion reaction in the D plasma experiments. Thus, the beam-thermal fusion reactions must be evaluated before the orbit calculations of the fast ^{3}He ions. To evaluate the beam-thermal fusion reaction, the fast D ion spatial and velocity distribution is needed. The fast D ion distribution can be evaluated from the orbit calculations of the fast D ions originating from the NB injections. Namely, the fast D ion orbits must be calculated before the fast ^{3}He ion orbit calculations. ii) The thermal-thermal fusion component can be evaluated from the plasma parameters measured in the experiment. iii) A ratio of the beam-beam fusion reaction rate to the total fusion reaction rate is small even near the plasma axis, where the beam-beam component is the highest. Here, we did not take into account the beam-beam DD fusion reaction for the evaluation of the ^{3}He ion birth distribution since the influence of the beam-beam fusion reactions is estimated to be small and the calculation method of the beam-beam fusion component is very complicated. In this study, we took into account the beam-thermal and thermal-thermal fusion reactions for the evaluation of the birth distribution of the fast ^{3}He ions.

We calculated the guiding-center orbits with the OFMC. Influences of the guiding-center approximation on orbit positions are discussed in Section 4.2.2. The orbits were calculated until test particles hit the wall or

until their energies are decreased to around the bulk ion temperature.

Figure 4.1 shows the flowchart for the evaluation of the fast ^{3}He ion velocity distribution. At first, the orbit calculations of the fast D ions originating from the NB injections were carried out with the OFMC. The number of test particles for the fast D ion orbit calculations was 10^5. Its initial condition for the test particles was given based on geometries of the NB system, and the powers and the accelerated voltages of the NB injections in the experiments. We evaluated the birth spatial and velocity distribution of the beam-thermal fusion produced ^{3}He ions from the fast D ion orbit calculation results. The detailed evaluation method of the ^{3}He ion birth velocity distribution is described in Section 4.2.3. In addition, we evaluated the thermal-thermal fusion components for the ^{3}He ion birth distribution from the plasma parameters in the experiment. Next, we calculated the fast ^{3}He ion orbits with the OFMC by using the evaluated ^{3}He ion birth distribution as the initial condition. The number of the test particles for the fast ^{3}He ion orbit calculations was 5×10^5. Then, we evaluated the fast ^{3}He ion velocity distribution from the fast ^{3}He ion orbit calculations. We used a sampling box for the evaluation of the fast ^{3}He ion velocity distribution (see Fig. 5.4 as examples). The sampling box is a square on the poloidal cross section. In the orbit calculations of the fast ^{3}He ions, the velocity vectors of the test particles that come into the sampling box are measured for the evaluation of the velocity distribution. Its velocity distribution is averaged in the toroidal direction.

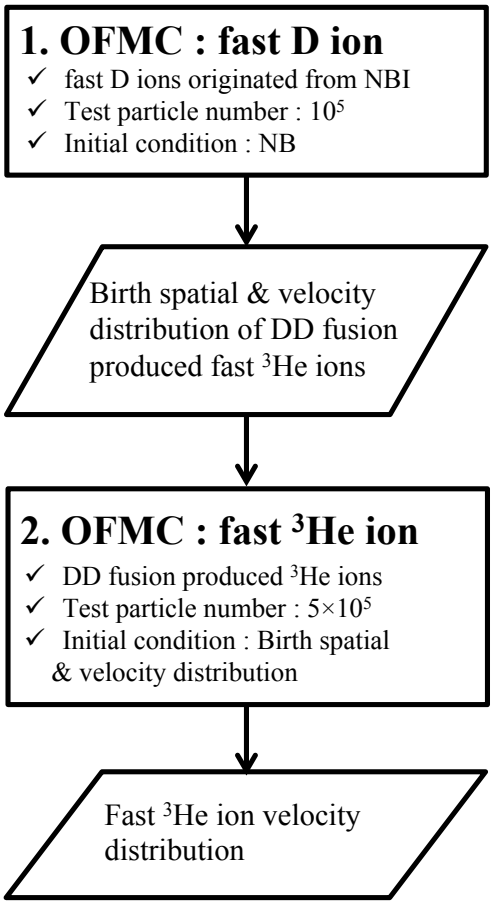

Figure 4.1. A flowchart for the evaluation of the velocity distribution of the DD fusion produced fast ^{3}He ions with the OFMC.

4.2.2. Influence of guiding-center approximation on orbit position

Here, we confirm whether the guiding-center approximation is reasonable under a typical plasma condition analyzed in this study. We compared orbit positions of collisionless full-gyro and guiding-center orbits of the fast ^{3}He ions passing through the midplane edge of the plasma on the low field side. In these calculations, the toroidal magnetic field ripples were taken into account. The plasma equilibrium used for these calculations is a typical case analyzed in this study (see Fig. 6.7(a)). The initial position, energy and pitch angle of the fast ^{3}He ion were set to be at the midplane edge of the plasma on the low field side, 500 keV and 54 degree, respectively. Here, the energy of 500 keV is an energy almost corresponding to the largest population of the bump-on-tail structure in the case of the more quantitatively evaluated distributions (see Figs. 6.3(b) and 6.10(a) as examples). Figure 4.2 shows the calculated full-gyro and guiding-center orbits of the fast ^{3}He ions on the poloidal cross section. We can see a small gyro radius, which is about 0.03 m at the plasma edge on the low field side, and about 3% of the minor radius.

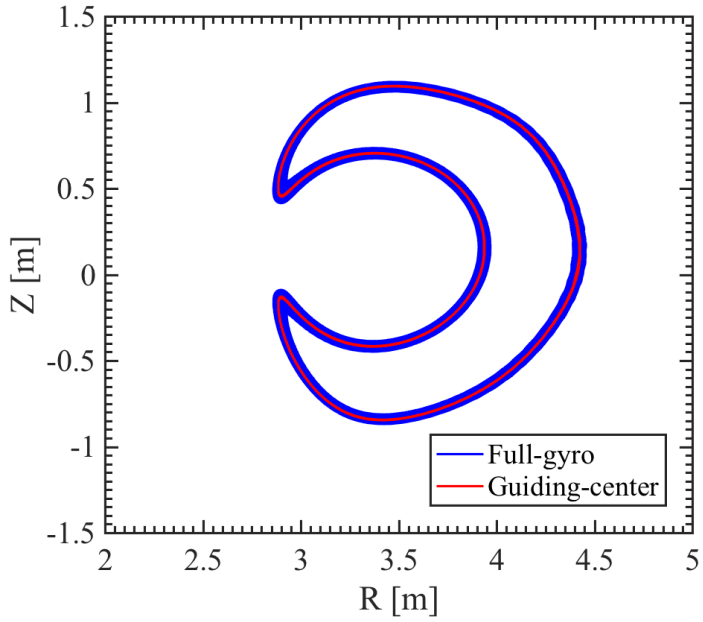

Figure 4.2. The full-gyro (blue line) and guiding-center orbits (red line) of the fast ^{3}He ions passing through the midplane edge of the plasma on the low field side on the poloidal cross section. The initial position, energy and pitch angle of the fast ^{3}He ion are at the midplane edge of the plasma on the low field side, 500 keV and 54 degree, respectively.

Here, we focus on the canonical angular momentum P_φ since P_φ is an indicator of the radial position of the orbit [7]. P_φ is given by,

$$P_\varphi = mRv_\varphi - q\psi \tag{4.7}$$

where, v_φ is the toroidal velocity of the fast ion and ψ is the poloidal magnetic flux. Figure 4.3 shows time evolution of P_φ of the calculated orbits. We cannot take exact same initial values for the full-gyro and

guiding-center orbit calculations since the relation of the particle positions between the full-gyro and guiding-center orbits are complicated in the inhomogeneous magnetic field. The initial P_φ in the guiding-center orbit case is set to be as close value to that in the full-gyro case. We set the initial P_φ to ~7.39×10^{-20} kg m^2/sec in the guiding-center orbit case and ~7.43×10^{-20} kg m^2/sec in the full-gyro case. The field ripples cause the temporal variations of P_φ. There are small differences of P_φ between the full-gyro and guiding-center orbits at t = 1 msec, which almost corresponds to the time scale that the particle energy is decreased by about 5 keV due to collisions with mainly bulk electrons. The collisions can "reset" the orbit position many times on this time scale. Hence, the difference between the collisionless full-gyro and guiding-center orbits from the results in Fig. 4.3 can be considered as the largest difference caused by the guiding-center approximation. P_φ is equal to $-q\psi$ since v_φ is zero when the trapped fast ions are located at the banana-tip positions. Thus, the value of $\psi_\mathrm{b} = -P_\varphi/q$ is a poloidal magnetic flux at the banana-tip position and can be an intuitive index of the orbit position. The difference of ψ_b between the full-gyro and guiding-center orbits, $\Delta\psi_\mathrm{b}$ is ~2.4×10^{-3} Wb at t = 1 msec. The ratio of $\Delta\psi_\mathrm{b}/|\psi_0 - \psi_\mathrm{s}|$ is ~0.39% where ψ_0 and ψ_s are ψ at the plasma axis and at the plasma surface, respectively. From the ratio $\Delta\psi_\mathrm{b}/|\psi_0 - \psi_\mathrm{s}|$, we can estimate the difference of the orbit position at the plasma edge on the low field side between the full-gyro and guiding-center orbits. The estimated difference is ~3 mm, which can be the largest difference as discussed above. Hence, the influences of the differences between the full-gyro and guiding-center orbits on the fast ^{3}He ion distribution are expected to be small. Namely, it was confirmed that the guiding-center approximation is reasonable under the conditions analyzed in this study.

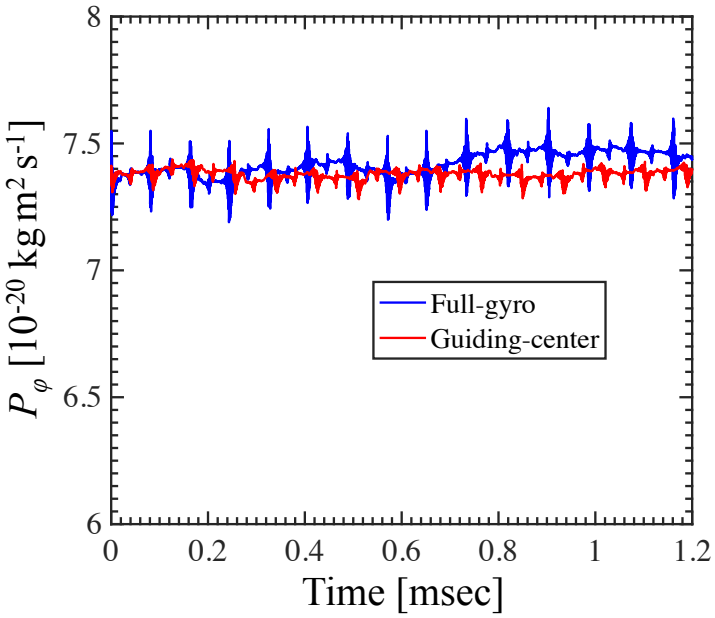

Figure 4.3. Time evolution of the toroidal canonical angular moments P_φ of the full-gyro (blue line) and guiding-center orbits (red line) of the fast ^{3}He ions passing through the midplane edge of the plasma on the low field side.

4.2.3. Birth energy of the fusion product in the laboratory system

The birth energy of the fusion products strictly depends on velocity vectors of fuel ions and a scattering angle of the fusion reaction. Thus, the birth energy of beam-thermal fusion produced ions can have a spread and anisotropy because the fast fuel ions originating from the beam have relatively high energies and their pitch-angle distribution are anisotropic. The birth energy of the DD fusion produced ^{3}He ion in the laboratory system $E_{3\mathrm{He}}$ is given by [8],

$$E_{3\mathrm{He}} = \frac{1}{2} m_{3\mathrm{He}} V_{\mathrm{c}}^2 + \frac{m_{\mathrm{n}}}{m_{\mathrm{n}} + m_{3\mathrm{He}}} (W_{\mathrm{f}} + K_{\mathrm{r}}) + V_{\mathrm{c}} \mu_{\mathrm{s}} \sqrt{\frac{2 m_{\mathrm{n}} m_{3\mathrm{He}}}{m_{\mathrm{n}} + m_{3\mathrm{He}}} (W_{\mathrm{f}} + K_{\mathrm{r}})} \tag{4.8}$$

where, $m_{3\mathrm{He}}$ and m_{n} are the mass of the ^{3}He ion and the neutron, respectively. V_{c} is the velocity of the center-of-mass system, W_{f} is the generated energy by the fusion reaction, and K_{r} is the relative energy of the D ions that are fuels for the DD fusion reaction. μ_{s} is the cosine of the scattering angle of the fusion reaction. This scattering angle is defined as an angle between V_{c} and the ^{3}He ion velocity vector in the center-of-mass system. Figure 4.4 shows the scattering angle dependences of the ^{3}He ion birth energy in the cases when the beam D ions with the energy E_{beam} of 350 keV (solid line) and 85 keV (dashed line) are injected to static D ions. The ^{3}He ion birth energy distributions have anisotropy, and the anisotropy becomes stronger as the D ion energy increases.

The scattering-angle distribution is not uniform function, but is given by the probability density based on the differential cross section for the DD fusion reaction. The differential cross section for the neutron produced by the DD fusion reaction $d\sigma/d\Omega'$ is often approximated by,

$$\frac{d\sigma}{d\Omega'} \propto \sum_j A_j P_j(\mu_{\mathrm{s}}) \tag{4.9}$$

where, σ is the cross section of the fusion reaction, Ω' is the solid angle, A_j is the reduced Legendre coefficients and P_j is the Legendre polynomials. In this study, we adopted A_j for the neutron of the D(d,n)^{3}He reaction from the work by Drosg and Otuka (2015) [9] and calculated neutron birth velocity distributions. Then, we calculated the ^{3}He ion birth velocity distribution from the neutron birth velocity distribution based on the energy conservation law and the momentum conservation law.

In Chapter 5, we did not take into account the influence of the scattering angle and the fast D ion velocity vectors on the ^{3}He ion birth velocity distribution, and assumed the birth energy and birth pitch angle distribution of the ^{3}He ion to be 820 keV and uniform, respectively. On the other hand, we took into account this influence in Chapter 6 to more quantitatively assess the characteristics of the fast ^{3}He ion velocity distribution.

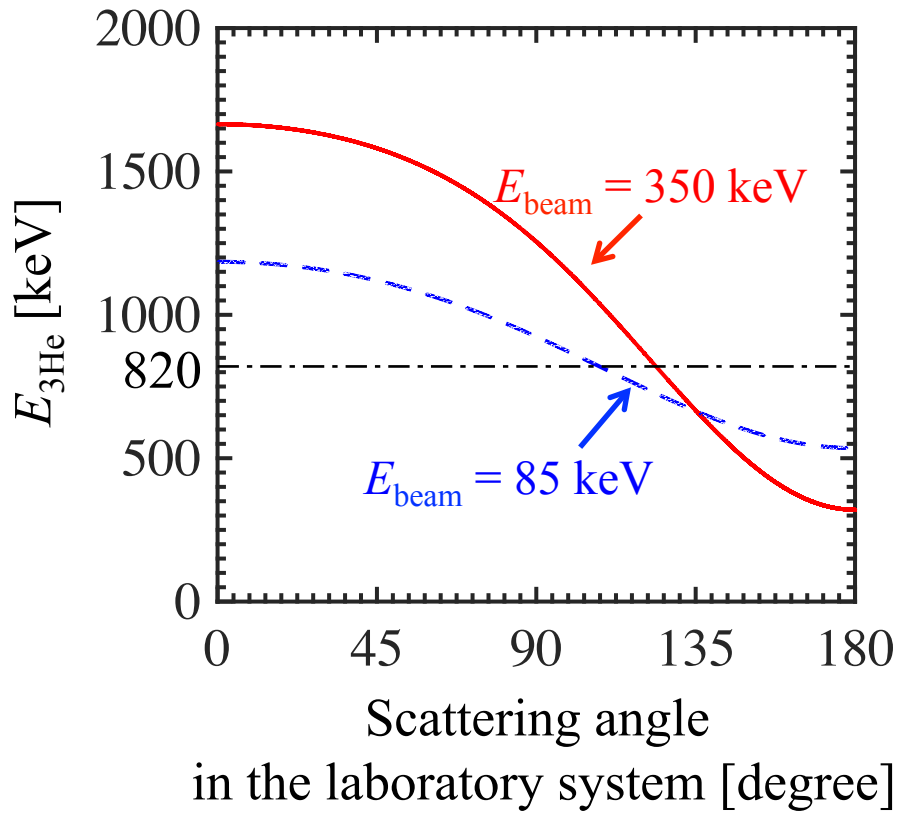

Figure 4.4. Scattering-angle dependences of the ^{3}He ion birth energy in the laboratory system. Solid and dashed lines indicate the cases when the 350 keV and 85 keV D ions are injected to the static D ions, respectively.

References in Chapter 4

[1] K. Tani *et al.*, J. Phys. Soc. Jpn. **50**, 1726 (1981).

[2] K. Shinohara *et al.*, Nucl. Fusion **43**, 586 (2003).

[3] K. Tobita *et al.*, Nucl. Fusion **35**, 1585 (1995).

[4] T. Oikawa *et al*., Nucl. Fusion **41**, 1575 (2001).

[5] K. Shinohara *et al.*, Nucl. Fusion **47**, 997 (2007).

[6] G. J. Kramer *et al*., Nucl. Fusion **53**, 123018 (2013).

[7] J. Wesson, *Tokamaks*, Oxford University Press, Oxford (1987)..

[8] H. Brysk, Plasma Phys. **15**, 611 (1973).

[9] M. Drosg and N. Otuka, *Evaluation of the Absolute Angle-Dependent Differential Neutron Production Cross Sections by the Reactions ^{3}H(p,n)^{3}He, ^{1}H(t,n)^{3}He, ^{2}H(d,n)^{3}He, ^{3}H(d,n)^{4}He, and ^{2}H(t,n)^{4}He and of the Cross Sections of Their Time-Reversed Counterparts up to 30 MeV and Beyond*, Vienna: IAEA Nuclear Data Section, Vienna International Centre, INDC(AUS)-0019 (2015).

Chapter 5
Comparison of Dispersions of Observed ICE(^{3}He) with the MCI

In this chapter, we have evaluated the fast ^{3}He ion velocity distribution and compared the dispersions of the observed ICE(^{3}He) with those of the calculated MCI. First, we explain a typical discharge where the ICE(^{3}He) is observed under an almost stationary plasma condition, and the evaluation results of the fast ^{3}He ion distribution. Then, we discuss the reproducibility of the evaluated fast ^{3}He ion distribution with the OFMC. Next, we explain wave equations in our wave dispersion code, and its calculation methods. Finally, we explain the comparison results of the dispersions of the observed ICE(^{3}He) with those of the calculated MCI, and discuss the emission mechanism for the ICE(^{3}He) in terms of the dispersion.

5.1. Evaluation of fast ^{3}He ion velocity distribution under a stationary condition

5.1.1. Observation of ICE(^{3}He) under an almost stationary plasma condition

We evaluate the fast ^{3}He ion slowing-down velocity distribution in a discharge where the ICE(^{3}He) is observed under the stationary plasma condition to collect good statistics. Figure 5.1 shows the time evolution of (a) the plasma current I_p, (b) the safety factor at 95% the magnetic flux q_{95} and (c) R at the midplane edge of the plasma on the low field side R_{edge} in a discharge of E48461, which is a typical discharge where the ICE(^{3}He) is observed under the almost stationary condition. In this discharge, I_p and q_{95} become almost stationary after t = ~2.5 sec. R_{edge} is also almost constant after t = ~4.0 sec. Namely, the plasma equilibrium is considered to be almost stationary after t = ~4.0 sec.

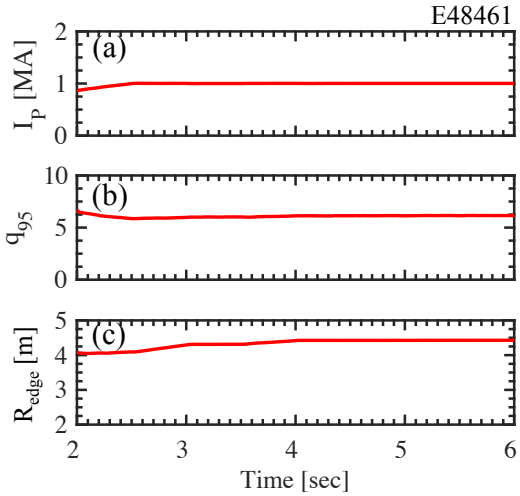

Figure 5.1. Time evolution of (a) the plasma current I_p, (b) the safety factor at 95 % the magnetic flux q_{95} and (c) the major radius position R at the midplane edge of the plasma on the low field side R_{edge} in E48461.

Figure 5.2 shows the time evolution of (a) the P-NB power, (b) the line-averaged density $\overline{n_e}$, (c) the stored energy of the plasma W_d, and (d) the neutron emission rate S_n in E48461. The perpendicular and tangential P-NBs were injected from t = ~3.5 sec. The plasma parameters such as $\overline{n_e}$ and W_d are almost stationary after t = ~4.5 sec. S_n drastically increases just after the NB injection and also becomes stationary from t = ~4.5 sec. The temporal behavior of S_n indicates that the number of the DD fusion reactions increases due to the NB injection. Both of the plasma equilibrium and parameters are almost stationary from t = ~4.5 sec.

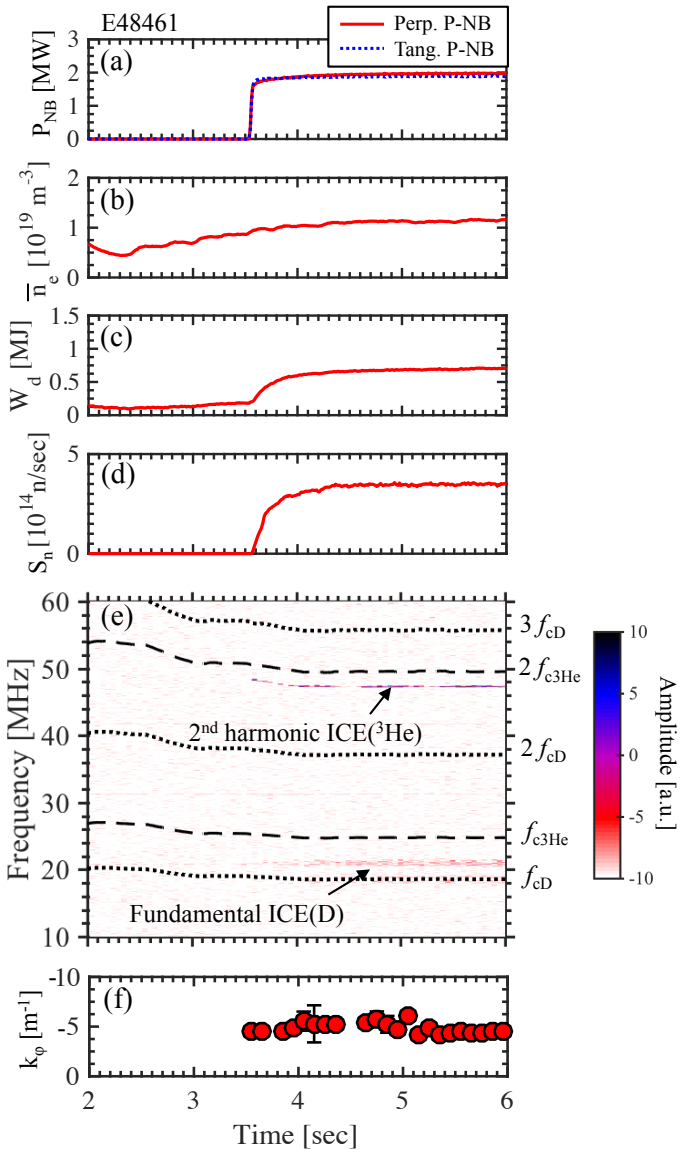

Figure 5.2. Time evolution of (a) the perpendicular (solid line) and tangential P-NB powers (dotted line) P_{NB}, (b) the line-averaged electron density $\overline{n_e}$, (c) the stored diamagnetic energy of the plasma W_d, (d) the total neutron emission rate S_n, (e) the frequency spectrum of the electrostatic and/or electromagnetic fluctuations and (f) the toroidal wavenumber k_φ of the 2nd harmonic ICE(^{3}He) in E48461. (e) Dotted and dashed lines indicate the cyclotron frequencies and its harmonics for the D ion f_{cD} and the ^{3}He ion f_{c3He} at the midplane edge of the plasma on the low field side, respectively.

Figure 5.2(e) shows the time evolution of the ICRF fluctuations measured with the ICRF antenna strap. A strong fluctuation in the frequency slightly below $2f_{c3He}$ is observed just after S_n begins to significantly increase (t = ~3.5 sec). This fluctuation is interpreted as 2nd harmonic ICE(^{3}He). The 2nd harmonic ICE(^{3}He) continues to be observed under the almost stationary plasma condition. Also, a fluctuation in the frequency around f_{cD} appears, and is interpreted as fundamental ICE(D). Figure 5.2(f) shows the measured toroidal wavenumber k_φ of the 2nd harmonic ICE(^{3}He).

Radial profiles of n_e and T_e were simultaneously measured with the ruby laser Thomson scattering at t = 5.1 sec in E48461. Figure 5.3 shows radial profiles of (a) q_{safe}, and (b) n_e and T_e at t = 5.1 sec. Using Eq. (2.31) and the plasma parameters of n_e and T_e shown in Fig. 5.3, we estimated the slowing-down time τ_s of the fast ^{3}He ions having 820 keV at the plasma axis (τ_{s0}) around t = 5.1 sec. τ_{s0} around t = 5.1 sec is estimated to be about 0.3-0.4 sec. The 2nd harmonic ICE(^{3}He) continues to be observed even on the time scale longer than τ_{s0} after S_n has become almost constant. This indicates that the 2nd harmonic ICE(^{3}He) appears even when the fast ^{3}He ion velocity distribution becomes the slowing-down distribution. Thus, we evaluate the fast ^{3}He ion slowing-down velocity distribution at t = 5.1 sec in E48461 as a typical case for the excitation of the ICE(^{3}He) by using the plasma parameter shown in Fig. 5.3.

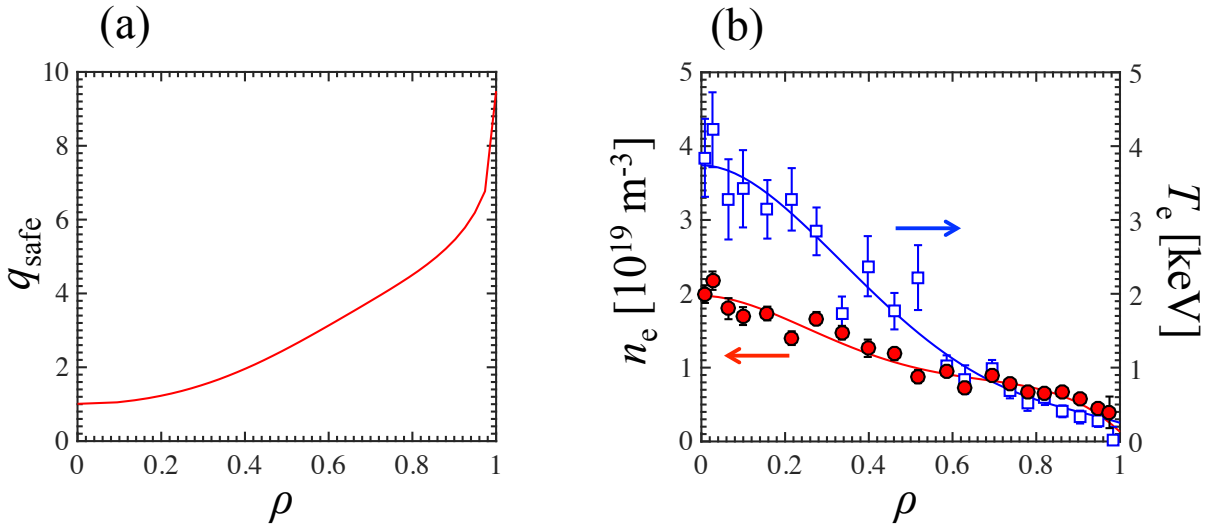

Figure 5.3. Radial profiles of (a) the safety factor q_{safe} and (b) the electron density n_e (circles) and temperature T_e (squares) at t = 5.1 sec in E48461. Here, ρ is the normalized minor radius.

Figure 5.4 shows the plasma equilibrium and typical sampling boxes at t = 5.1 sec in E48461. Centers of the sampling boxes shown in Fig. 5.4 are located at $R = R_{axis}$, 4.25 m and R_{edge}. At t = 5.1 sec, R_{axis} = ~3.53 m and R_{axis} = ~4.43 m. Their Z locations are the same as that of the plasma axis. Lengths of the sampling boxes are 0.08 m in the R direction and 0.2 m in the Z direction. The plasma equilibrium and these sampling boxes shown in Fig. 5.4 were used for the evaluations of the fast ^{3}He ion slowing-down velocity distributions at t = 5.1 sec in E48461.

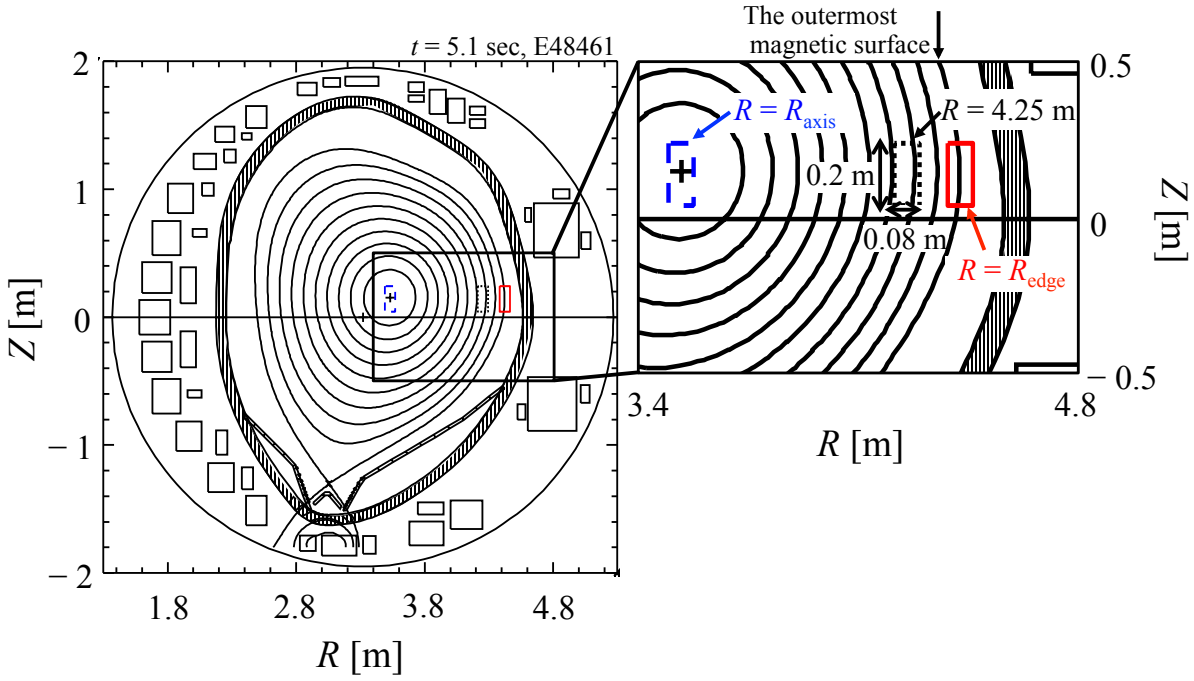

Figure 5.4. The plasma equilibrium (left) and typical sampling boxes (right) for the evaluation of the fast ^{3}He ion velocity distribution at t = 5.1 sec in E48461. These sampling boxes are located at $R = R_{\mathrm{axis}}$ (dashed box), 4.25 m (dotted box) and R_{edge} (solid box). At t = 5.1 sec, R_{axis} and R_{edge} are ~3.53 m and ~4.43 m, respectively.

5.1.2. Evaluation results of the fast ^{3}He ion velocity distribution

As mentioned in Section 5.1.1, we firstly calculated fast D ion orbits to evaluate the ^{3}He ion birth spatial distribution by using the plasma parameters shown in Fig. 5.3 and the equilibrium shown in Fig. 5.4 at t = 5.1 sec in E48461. In these orbit calculations, the toroidal magnetic field ripples were not taken into account and the toroidal symmetry was assumed. Figure 5.5 shows the evaluated birth spatial distribution of the ^{3}He ion at t = 5.1 sec in E48461. The ^{3}He ions are mainly produced near the plasma center. We used Fig. 5.5 for the initial condition of the fast ^{3}He ion orbit calculation. As mentioned in Section 4.2.3, we assumed its birth energy and pitch angle distribution to be 820 keV and uniform, respectively.

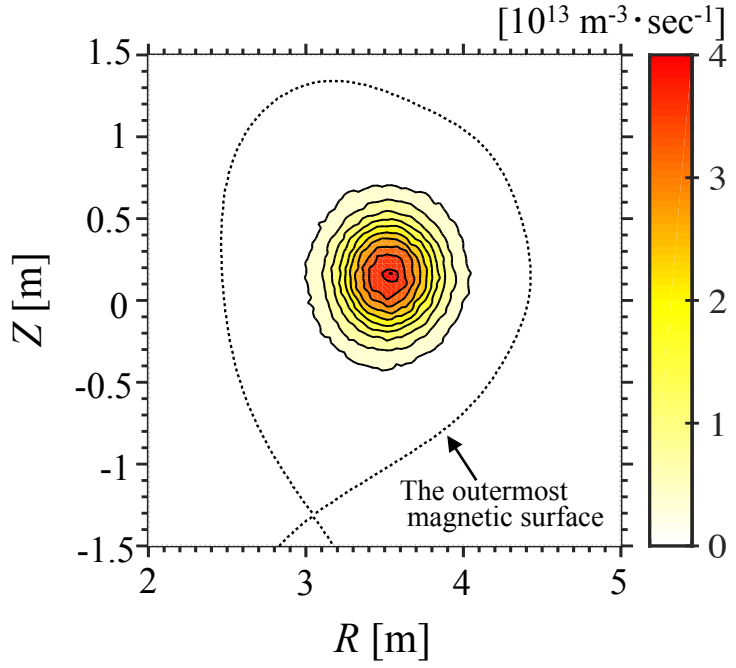

Figure 5.5. The evaluated ^{3}He ion birth spatial distribution on the poloidal cross section at t = 5.1 sec in E48461.

Figure 5.6 shows the evaluated fast ^{3}He ion energy E and pitch-angle ϕ_{pitch} slowing-down distributions at (a) $R = R_{\mathrm{axis}}$, (b) $R = 4.25$ m and (c) $R = R_{\mathrm{edge}}$ at t = 5.1 sec in E48461. These distributions were evaluated at the sampling boxes shown in Fig. 5.4. Most of the fast ^{3}He ions are located in relatively low energy region and its pitch-angle distribution structure is broad at $R = R_{\mathrm{axis}}$ as shown in Fig. 5.6(a). The population of the fast ^{3}He ions is relatively less in a region near ϕ_{pitch} = ~104 degrees. Figure 5.7 shows the guiding-center orbits of the fast ^{3}He ions passing through the plasma axis and the ^{3}He ion birth spatial distribution (same distribution as Fig. 5.5). The fast ^{3}He ion with ϕ_{pitch} = 104 degree draws the large banana orbits and passes through a region where the number of the ^{3}He ion productions is relatively small by comparison with the fast ^{3}He ions having ϕ_{pitch} = 94 and 114 degrees. Therefore, the population of the fast ^{3}He ions becomes relatively less in the region near ϕ_{pitch} = ~104 degrees. At $R = 4.25$ m, a width of the pitch-angle distribution of relatively high-energy fast ^{3}He ions is narrow as shown in Fig. 5.6(b). Namely, the

distribution has strong anisotropy in the relatively high-energy region. The width of the pitch-angle distribution becomes broader as the energy is decreases. This is because the probability of the pitch-angle scatterings due to the collisions with the bulk ions increases in the relatively low-energy region. The largest population of its pitch-angle distribution is located around ϕ_{pitch} = 60 degrees. On the other hand, relatively low-energy fast ^{3}He ions are dominant and no bump-on-tail structure is formed in the energy direction. In the case of $R = R_{\mathrm{edge}}$, the most of the fast ^{3}He ions are located in relatively high-energy region and the bump-on-tail structure is formed as shown in Fig. 5.6(c). In addition, the pitch-angle distribution is narrow there, i.e., the fast ^{3}He ion distribution at $R = R_{\mathrm{edge}}$ has both of the bump-on-tail structure and the strong pitch-angle anisotropy. The population of the pitch-angle distribution is the largest around ϕ_{pitch} = 56 degrees.

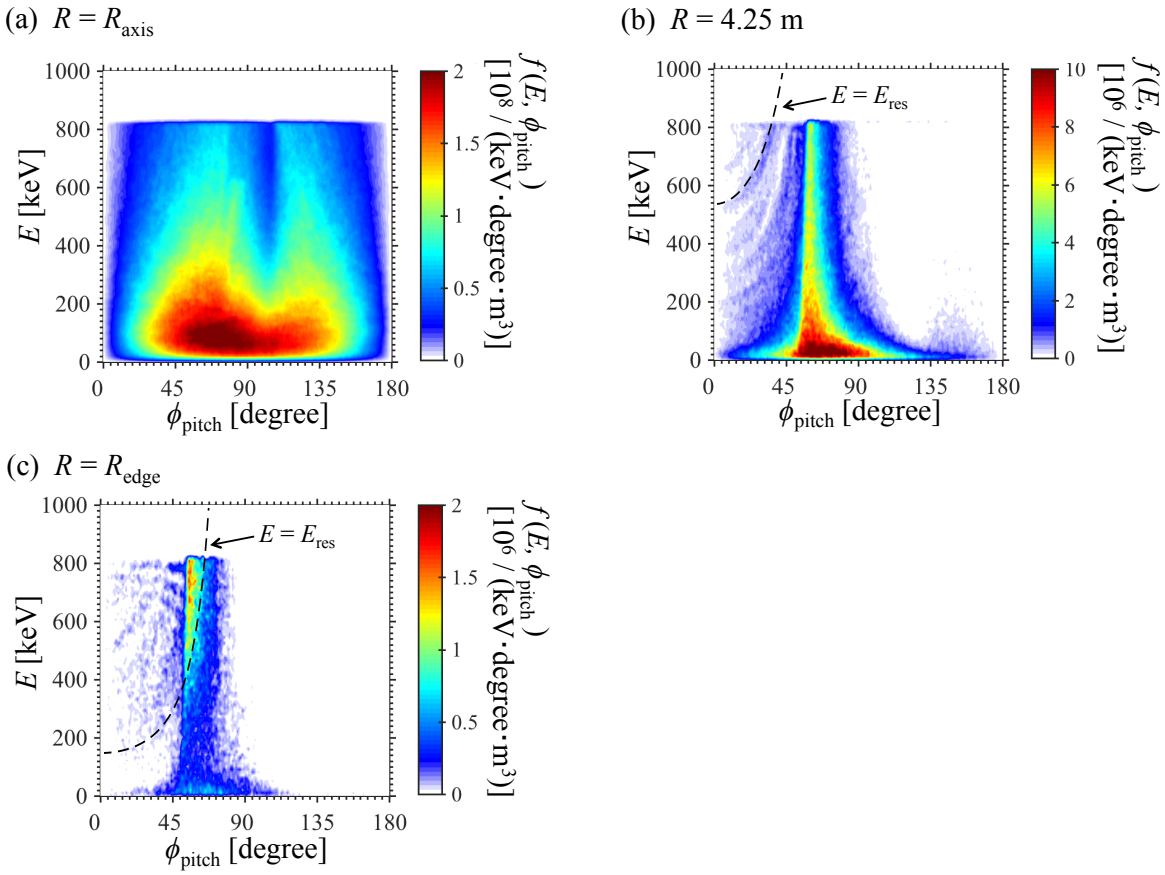

Figure 5.6. Evaluated energy E and pitch-angle ϕ_{pitch} slowing-down distributions of the fast ^{3}He ions at (a) $R = R_{\mathrm{axis}}$, (b) R = 4.25 m and (c) $R = R_{\mathrm{edge}}$ at t = 5.1 sec in E48461. Here, R_{axis} and R_{edge} are ~3.53 m and ~4.43 m, respectively. Dashed lines indicate resonant energies E_{res} that satisfy the Doppler-shifted cyclotron resonance condition of Eq. (2.44) for fast ^{3}He ion. E_{res} is calculated by using the measured frequency and toroidal wave number k_φ of the 2$^{\mathrm{nd}}$ harmonic ICE(^{3}He) and the ^{3}He ion cyclotron frequencies f_{c3He} averaged during t = 5-6 sec in E48461.

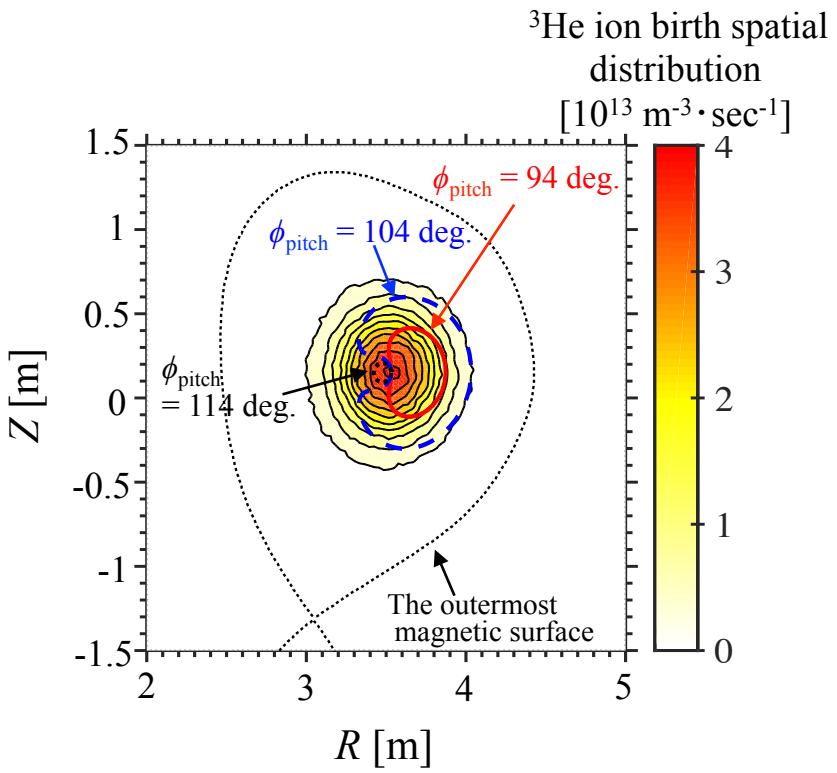

Figure 5.7. Guiding-center orbits of the fast ^{3}He ion with E = 820 keV passing through the plasma axis and the ^{3}He ion birth spatial distribution at t = 5.1 sec in E48461. Their pitch angles are 94 (solid line), 104 (dashed line) and 114 degrees (dotted line) at the plasma axis. A contour map is the evaluated ^{3}He ion birth spatial distribution.

Figure 5.8 shows the energy distributions at $R = 4.25$ m and R_{edge} at t = 5.1 sec in E48461. These distributions are the distributions at ϕ_{pitch} = ~60 degrees in the case of $R = 4.25$ m shown in Fig. 5.6(b) and at ϕ_{pitch} = ~56 degrees in the case of $R = R_{edge}$ shown in Fig. 5.6(c). A gradient of the energy distribution in the relatively high-energy region is negative in the case of $R = 4.25$ m. On the contrary, the gradient of the energy distribution is positive (the bump-on-tail structure) in the relatively high-energy region in the case of $R = R_{edge}$.

Figure 5.9 shows the guiding-center orbits of the fast ^{3}He ions passing through the midplane edge of the plasma on the low field side and the ^{3}He ion birth spatial distribution (same distribution as Fig. 5.5). As we mentioned in Section 2.2.3, the processes for the formation of the bump-on-tail structure and the strong anisotropy of the fast ^{3}He ions near the midplane edge of the plasma on the low field side are considered as follows. The ^{3}He ions are produced mainly near the plasma center. The large number of the fast ^{3}He ions having the pitch angles only near the trapped-passing boundary draw the large trajectories from the region near the plasma center to the plasma edge on the low field side. Then, the fast ^{3}He ion cannot reach the plasma edge when the scales of the trajectories become small as E is decreased by the collisions. Therefore, the number of relatively high-energy fast ^{3}He ions is larger than that of the relatively low-energy fast ^{3}He ions near the plasma edge on the low field side. As a result, the fast ^{3}He ion distribution has both of a positive gradient in the energy direction (the bump-on-tail structure) and the strong pitch-angle anisotropy near the plasma edge on the low field side.

We calculated resonant energies E_{res} satisfying the cyclotron resonance condition of Eq. (2.44) for the ^{3}He ions by using averaged values of measured frequency and toroidal wavenumber k_φ of the 2$^{\mathrm{nd}}$ harmonic ICE(^{3}He) and the ^{3}He ion cyclotron frequencies f_{c3He} during t = 5-6 sec. E_{res} is given by,

$$E_{\mathrm{res}} = \frac{1}{2} m_{3\mathrm{He}} v_{\mathrm{res}}^2 = \frac{1}{2} m_{3\mathrm{He}} \left(\frac{v_{\mathrm{res}\parallel}}{\cos \phi_{\mathrm{pitch}}} \right)^2 = \frac{1}{2} m_{3\mathrm{He}} \left(\frac{\omega - l\Omega_{3\mathrm{He}}}{k_\parallel \cos \phi_{\mathrm{pitch}}} \right)^2 \tag{5.1}$$

where, v_{res} is a resonant velocity of the fast ^{3}He ion and $v_{\mathrm{res}\parallel}$ is its parallel velocity component to the magnetic field line. The 2$^{\mathrm{nd}}$ harmonic ICE(^{3}He) frequency averaged during t = 5-6 sec is ~47.3 MHz . The averaged values of $2f_{\mathrm{c3He}}$ at $R = 4.25$ m and $R = R_{\mathrm{edge}}$ are ~51.6 MHz and ~49.5 MHz, respectively. The averaged k_φ of the 2$^{\mathrm{nd}}$ harmonic ICE(^{3}He) is about -4.60 m^{-1}. k_φ is negative when the waves of the 2$^{\mathrm{nd}}$ harmonic ICE(^{3}He) propagate in the CTR direction. Here, we assumed $k_\parallel = k_\varphi$. The Doppler shift $k_\parallel v_\parallel$ is negative in the frequency since $v_\parallel$ of the most fast ^{3}He ions is positive as shown in Fig. 5.6(b) and (c) and $k_\parallel < 0$. The sign of the Doppler shift is consistent with the experimental observation that the frequency of the 2$^{\mathrm{nd}}$ harmonic ICE(^{3}He) is lower than $2f_{\mathrm{c3He}}$. Then, we calculated E_{res} of Eq. (5.1) as shown in Fig. 5.6(b) and (c). At $R = 4.25$ m, E_{res} is not located near the fast ^{3}He ion distribution. On the other hand, E_{res} passes through the bump-on-tail structure of the fast ^{3}He ion distribution at $R = R_{\mathrm{edge}}$, i.e., the bump-on-tail structure of the fast ^{3}He ion distribution can satisfy the destabilization condition for the MCI [1-5] at $R = R_{\mathrm{edge}}$. Hence, the evaluated fast ^{3}He ion distribution at the plasma edge on the low field side is consistent with the destabilization condition for the MCI.

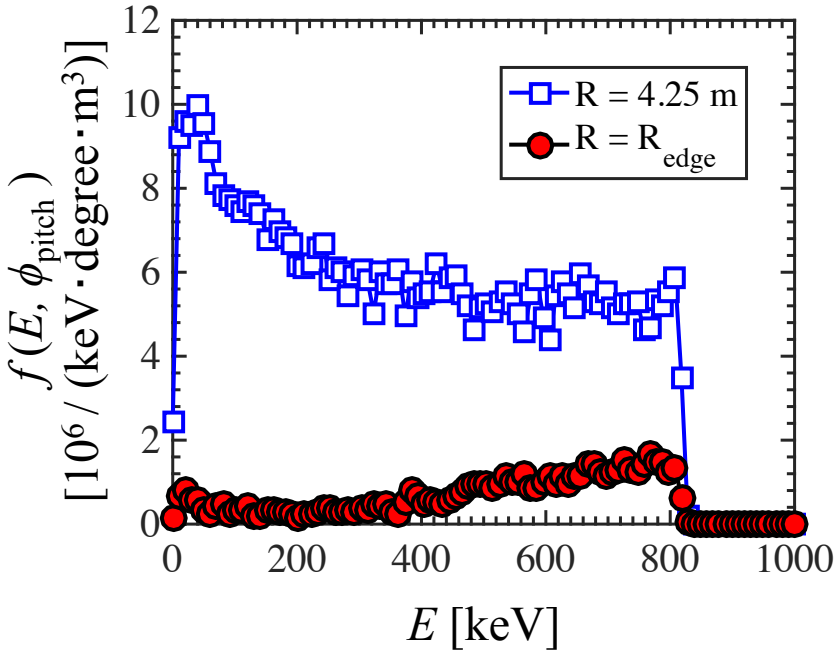

Figure 5.8. The energy slowing-down distributions at $R = 4.25$ m (squares) and $R = R_{\mathrm{edge}}$ (circles) at t = 5.1 sec in E48461. These distributions are the energy distributions at ϕ_{pitch} = ~60 degrees in the case of $R = 4.25$ m shown in Fig. 5.6(b), and at ϕ_{pitch} = ~56 degrees in the case of $R = R_{\mathrm{edge}}$ shown in Fig. 5.6(c).

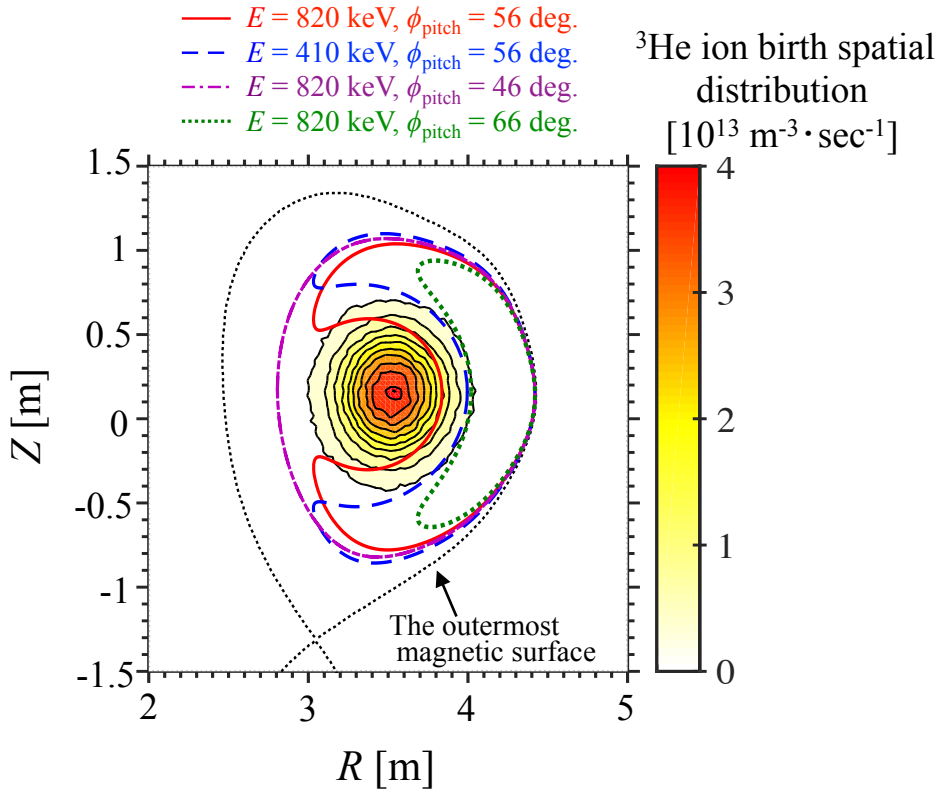

Figure 5.9. Guiding-center orbits of the fast ^{3}He ions passing through the midplane edge of the plasma on the low field side and the evaluated ^{3}He ion birth spatial distribution at t = 5.1 sec in E48461. Solid and dashed lines indicate orbits of fast ^{3}He ions having E = 820 keV and 410 keV with ϕ_{pitch} = 56 degree, respectively. Dotted-dashed and dotted lines are the orbits of the fast ^{3}He ions having E = 820 keV with ϕ_{pitch} = 46 degree and 56 degree, respectively. Their pitch angles are values at the plasma edge on the low field side. A contour map is the evaluated ^{3}He ion birth spatial distribution.

5.1.3. Reproducibility of the evaluation of the fast ^{3}He ion distribution with the OFMC

Here, we discuss reproducibility of the evaluated fast ^{3}He ion slowing-down distribution with the OFMC. We can confirm the reproducibility by carrying out the orbit calculations several times with different random seeds. To confirm the reproducibility of the distribution at $R = R_{\mathrm{edge}}$, we calculated the fast ^{3}He ion orbits several times with the different random seeds. These orbit calculations were conducted under the same condition as that used for the calculation of Fig. 5.6 except for the random seed. Figure 5.10 shows the energy distributions of the fast ^{3}He ions $f(E)$ at $R = R_{\mathrm{edge}}$ in the cases with the different random seeds. Here, we calculated these energy distributions by integrating the energy and pitch-angle distributions in the pitch-angle direction. The case 1 (thick line) is a case where the random seed is the same as that used for the calculation of Fig. 5.6. The differences in characteristics (e.g. the shape of the bump-on-tail structure) between the distributions in these cases are small. The small differences come from the Monte-Carlo error and have little influence on the discussion of the distribution in this study. Hence, the orbit calculation of the fast ^{3}He ions with the OFMC has the sufficient reproducibility.

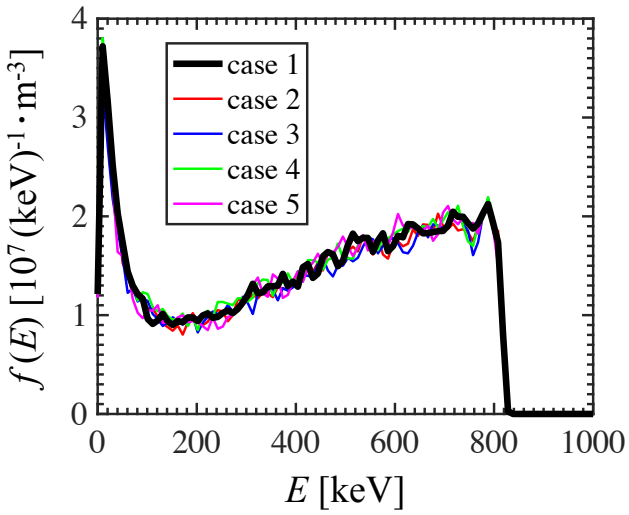

Figure 5.10. The energy slowing-down distributions of the fast ^{3}He ions $f(E)$ at $R = R_{\mathrm{edge}}$ in the cases with the different random seeds. A thick line and thin lines indicate the case 1 and the other cases, respectively. The case 1 is a case where the random seed is the same as that used for the calculation of Fig. 5.6.

5.2. Calculation of MCI dispersion and comparison with experimental observation

5.2.1. Equations in wave dispersion code

For the calculation of the dispersions of the MCI, we newly developed a wave dispersion code that can numerically solve the linearized wave equation with both of a shifted bi-Maxwell velocity distribution function and of a drifting-ring-type distribution function under the homogeneous plasma condition. This wave dispersion code has been developed based on the code that was developed by Prof. Dr. T. Watanabe and Dr. S. Kakimoto. Their code can numerically calculate the dispersion relation of the uniform plasma in the case when its velocity distribution function is given by the shifted bi-Maxwell distribution function [6, 7]. We have improved the code so as to treat fast ions with the drifting-ring-type distribution function. In this section, we explain equations in the wave dispersion code.

a) Shifted bi-Maxwell velocity distribution

Here, we derive the dielectric tensor elements for the shifted bi-Maxwell distribution function. The shifted bi-Maxwell function is given by [8],

$$f_0 = \sum_s n_s \sqrt{\frac{m_s}{2\pi T_{s\parallel}}} \exp\left\{-\frac{m_s(v_z - v_{\parallel 0})^2}{2T_{s\parallel}}\right\} \frac{m_s}{2\pi T_{s\perp}} \exp\left\{-\frac{m_s\left(v_x + v_y\right)^2}{2T_{s\perp}}\right\} \tag{5.2}$$

where, $T_{s\parallel}$ and $T_{s\perp}$ are the temperature in the parallel and perpendicular direction to the magnetic field line, respectively. $v_{\parallel 0}$ is the shifted parallel velocity of the bi-Maxwell distribution function. The wave equation of Eq. (2.38) can be expressed by,

$$\boldsymbol{H} \cdot \boldsymbol{E} = \begin{pmatrix} H_{xx} & H_{xy} & H_{xz} \\ H_{yx} & H_{yy} & H_{yz} \\ H_{zx} & H_{zy} & H_{zz} \end{pmatrix} \begin{pmatrix} E_x \\ E_y \\ E_z \end{pmatrix} = 0 \tag{5.3}$$

Eq. (5.3) has nontrivial solutions if

$$D(\omega, \boldsymbol{K}) = \det \begin{vmatrix} H_{xx} & H_{xy} & H_{xz} \\ H_{yx} & H_{yy} & H_{yz} \\ H_{zx} & H_{zy} & H_{zz} \end{vmatrix} = 0 \tag{5.4}$$

The matrix elements of $\boldsymbol{H}$ for the shifted-bi-Maxwell function can be obtained by substitution of Eq. (5.2) into Eq. (2.42). If $\boldsymbol{B} = (0, 0, B)$ and $\boldsymbol{k} = \left(k_x, k_y, k_z\right)$ in the orthogonal coordinate system, the matrix elements of $\boldsymbol{H}$ is given by,

$$
\begin{cases}
H_{xx} = 1 - \dfrac{c^2\left(k_y^2 + k_z^2\right)}{\omega^2} + \displaystyle\sum_{s,l} \frac{\omega_{ps}^2}{\omega^2}\left(\frac{l^2}{\vartheta}\eta_l - 2\frac{T_{s\perp}k_y^2}{m_s\Omega_s^2}\eta_l'\right)W_l \\
H_{xy} = \dfrac{c^2 k_x k_y}{\omega^2} + \displaystyle\sum_{s,l} \frac{\omega_{ps}^2}{\omega^2}\left(-il + 2\frac{T_{s\perp}k_x k_y}{m_s\Omega_s^2}\right)\eta_l' W_l \\
H_{xz} = \dfrac{c^2 k_x k_z}{\omega^2} + \displaystyle\sum_{s,l} \frac{\omega_{ps}^2}{\omega^2}\left(\frac{k_x l}{k_z\vartheta}\eta_l - i\frac{k_y}{k_z}\eta_l'\right)F_l \\
H_{yx} = \dfrac{c^2 k_y k_x}{\omega^2} + \displaystyle\sum_{s,l} \frac{\omega_{ps}^2}{\omega^2}\left(il + 2\frac{T_{s\perp}k_y k_x}{m_s\Omega_s^2}\right)\eta_l' W_l \\
H_{yy} = 1 - \dfrac{c^2\left(k_z^2 + k_x^2\right)}{\omega^2} + \displaystyle\sum_{s,l} \frac{\omega_{ps}^2}{\omega^2}\left(\frac{l^2}{\vartheta}\eta_l - 2\frac{T_{s\perp}k_x^2}{m_s\Omega_s^2}\eta_l'\right)W_l \\
H_{yz} = \dfrac{c^2 k_y k_z}{\omega^2} + \displaystyle\sum_{s,l} \frac{\omega_{ps}^2}{\omega^2}\left(\frac{k_y l}{k_z\vartheta}\eta_l + i\frac{k_x}{k_z}\eta_l'\right)F_l \\
H_{zx} = \dfrac{c^2 k_z k_x}{\omega^2} + \displaystyle\sum_{s,l} \frac{\omega_{ps}^2}{\omega^2}\left(\frac{k_x l}{k_z\vartheta}\eta_l + i\frac{k_y}{k_z}\eta_l'\right)F_l \\
H_{zy} = \dfrac{c^2 k_z k_y}{\omega^2} + \displaystyle\sum_{s,l} \frac{\omega_{ps}^2}{\omega^2}\left(\frac{k_y l}{k_z\vartheta}\eta_l - i\frac{k_x}{k_z}\eta_l'\right)F_l \\
H_{zz} = 1 - \dfrac{c^2\left(k_x^2 + k_y^2\right)}{\omega^2} + \displaystyle\sum_{s,l} \frac{\omega_{ps}^2}{\omega^2}\eta_l G_l
\end{cases}
\tag{5.5}
$$

where, η_l, ϑ, W_l, F_l, and G_l are defined as follows:

$$\eta_l = \exp(-\vartheta)\, I_l(\vartheta)$$

$$\eta_l' = \frac{d\eta_l}{d\vartheta}$$

$$\vartheta = \frac{T_{s\perp}\left(k_x^2 + k_y^2\right)}{m_s\Omega_s^2}$$

$$W_l = \frac{\omega - k_z v_\parallel}{\sqrt{2T_{s\parallel}k_z^2/m_s}} Z_l(\xi_l) + \frac{1}{2}\left(1 - \frac{T_{s\perp}}{T_{s\parallel}}\right) Z_l'(\xi_l)$$

$$F_l = \frac{l k_z v_\parallel}{\sqrt{2T_{s\parallel}k_z^2/m_s}} Z_l(\xi_l) + \frac{1}{2}\left\{\frac{\omega T_{s\perp}}{\Omega_s T_{s\parallel}} + l\left(\frac{T_{s\perp}}{T_{s\parallel}} - 1\right)\right\} Z_l'(\xi_l)$$

$$G_l = \frac{\omega + l\Omega_s\left(1 - \dfrac{T_{s\parallel}}{T_{s\perp}} - \dfrac{m_s v_\parallel}{T_{s\perp}}\right)}{\sqrt{2T_{s\parallel}k_z^2/m_s}} Z_l'(\xi_l)$$

$$\frac{\left\{\omega + l\Omega_s\left(1 - 2\dfrac{T_{s\parallel}}{T_{s\perp}}\right)\right\}k_z v_\parallel}{2T_{s\parallel}k_z^2/m_s} Z_l'(\xi_l) + \frac{1}{2}\frac{\omega + l\Omega_s\left(1 - \dfrac{T_{s\parallel}}{T_{s\perp}}\right)}{\sqrt{2T_{s\parallel}k_z^2/m_s}} Z_l''(\xi_l)$$

where, I_l is the modified Bessel function with the argument ϑ. Here, ξ_l, Z_l' and Z_l'' are,

$$\xi_l = \frac{\omega + l\Omega_s - k_z v_\parallel}{\sqrt{2T_{s\parallel}k_z^2/m_s}}$$
$$Z_l' = \frac{dZ_l}{d\xi_l}$$
$$Z_l'' = \frac{d^2 Z_l}{d\xi_l^2}$$

The function of $Z_l(\xi_l)$ is called the plasma dispersion function, and is defined as,

$$Z_l(\xi) = 2i \exp(-\xi^2) \int_{-\infty}^{i\xi} \exp(-x^2)\, dx \tag{5.6}$$

Numerically solving the determinant of Eq. (5.4), we can obtain the dispersion relation for the waves in the homogeneous plasma with the shifted bi-Maxwell distribution.

b) Drifting-ring-type velocity distribution

In the theoretical analysis of the MCI, the distribution having the bump-on-tail structure and the strong anisotropy at the plasma edge is often approximated by the drifting-ring-type ion velocity distribution function. One of the drifting-ring-type distribution functions normalized by the density is given by [1],

$$f_0 = \frac{1}{2\pi^{3/2} u v_{\parallel \mathrm{s}}} \exp\left\{-\frac{(v_\parallel - v_{\parallel \mathrm{c}})^2}{v_{\parallel \mathrm{s}}^2}\right\} \delta(v_\perp - u) \tag{5.7}$$

where $v_{||\mathrm{c}}$ is the center of the fast ion parallel velocity, $v_{||\mathrm{s}}$ is the spread of the distribution in the parallel velocity direction and u is the perpendicular velocity to the magnetic field. This distribution is expressed by a Gaussian in the parallel velocity direction and a delta function in the perpendicular velocity direction.

We derive the dielectric tensor elements for the above drifting-ring-type distribution function if $\boldsymbol{B} = (0, 0, B)$ and $\boldsymbol{k} = (k_\perp, 0, k_\parallel)$ in the orthogonal coordinate system. The dielectric tensor $\boldsymbol{\varepsilon}$ for the drifting ring-type distribution can be obtained by substitution of Eq. (5.7) into Eq. (2.42).

$$\varepsilon_{i,j} = \delta_{i,j}\left(1 - \sum_s \frac{\omega_{\mathrm{p}s}^2}{\omega^2}\right) + \varepsilon_{i,j}' \tag{5.8}$$

where,

$$
\begin{cases}
\varepsilon'_{xx} = \sum_{s,l} \dfrac{\omega_{\mathrm{ps}}^2}{\omega^2} \dfrac{l^2}{\lambda_0^2} \left[2(\xi'_0 - \xi'_l)\lambda_0 J_l J'_l Z_l + \dfrac{2u^2}{v_{\parallel \mathrm{s}}^2} J_l^2 (1 + \xi'_l Z_l) \right] \\
\varepsilon'_{xy} = i \sum_{s,l} \dfrac{\omega_{\mathrm{ps}}^2}{\omega^2} \left(\dfrac{l\Omega_s}{k_\perp} \right) \dfrac{1}{u v_{\parallel \mathrm{s}}} \left[\dfrac{l\Omega_s}{k_\parallel} \left(J_l J'_l + \lambda_0 {J'_l}^2 + \lambda_0 J_l J''_l \right) Z_l + \dfrac{2u^2}{v_{\parallel \mathrm{s}}^2} J_l J'_l (1 + \xi'_l Z_l) \right] \\
\varepsilon'_{xz} = \sum_{s,l} \dfrac{\omega_{\mathrm{ps}}^2}{\omega^2} \left(\dfrac{l\Omega_s}{k_\perp} \right) \dfrac{2}{u v_{\parallel \mathrm{s}}} \left[\dfrac{l k_\perp}{k_\parallel} J_l J'_l \{ v_{\parallel \mathrm{s}} (1 + \xi'_l Z_l) + v_{\parallel \mathrm{c}} Z_l \} + \dfrac{u(\xi'_l v_{\parallel \mathrm{s}} + v_{\parallel \mathrm{c}})}{v_{\parallel \mathrm{s}}} J_l^2 (1 + \xi'_l Z_l) \right] \\
\varepsilon'_{yx} = -\varepsilon'_{xy} \\
\varepsilon'_{yy} = \sum_{s,l} \dfrac{\omega_{\mathrm{ps}}^2}{\omega^2} \dfrac{2}{v_{\parallel \mathrm{s}}} J'_l \left[\dfrac{l\Omega_s}{k_\parallel} (J'_l + \lambda_0 J''_l) Z_l + \dfrac{u^2}{v_{\parallel \mathrm{s}}} J'_l (1 + \xi'_l Z_l) \right] \\
\varepsilon'_{yz} = -i \sum_{s,l} \dfrac{\omega_{\mathrm{ps}}^2}{\omega^2} \dfrac{1}{u v_{\parallel \mathrm{s}}} \left[\dfrac{l\Omega_s}{k_\parallel} \left(J_l J'_l + \lambda_0 {J'_l}^2 + \lambda_0 J_l J''_l \right) \{ v_{\parallel \mathrm{s}} (1 + \xi'_l Z_l) + v_{\parallel \mathrm{c}} Z_l \} + \dfrac{2u^2}{v_{\parallel \mathrm{s}}^2} (\xi'_l v_{\parallel \mathrm{s}} + v_{\parallel \mathrm{c}}) J_l J'_l (1 + \xi'_l Z_l) \right] \\
\varepsilon'_{zx} = \varepsilon'_{xz} \\
\varepsilon'_{zy} = -\varepsilon'_{yz} \\
\varepsilon'_{zz} = \sum_{s,l} \dfrac{\omega_{\mathrm{ps}}^2}{\omega^2} \dfrac{2}{u v_{\parallel \mathrm{s}}} J_l \\
\quad \left[\dfrac{l\Omega_s}{k_\parallel u} J_l J'_l \left\{ (\xi'_l v_{\parallel \mathrm{s}} + v_{\parallel \mathrm{c}}) \left(v_{\parallel \mathrm{s}} + Z_l (\xi'_l v_{\parallel \mathrm{s}} + v_{\parallel \mathrm{c}}) \right) + v_{\parallel \mathrm{s}} v_{\parallel \mathrm{c}} \right\} + \dfrac{u}{v_{\parallel \mathrm{s}}} J_l \left\{ \dfrac{v_{\parallel \mathrm{s}}^2}{2} + (\xi'_l v_{\parallel \mathrm{s}} + v_{\parallel \mathrm{c}})^2 (1 + \xi'_l Z_l) \right\} \right]
\end{cases}
$$

where, Z_l is the plasma dispersion function of Eq. (5.6) with argument of ξ'_l, and J_l is the Bessel function with argument of λ_0. J'_l and J''_l are the first and the second derivatives of J_l, respectively. ξ'_l, ξ'_0 and λ_0 are defined as follows.

$$
\xi'_l = \frac{\omega - k_\parallel v_{\parallel \mathrm{c}} - l\Omega_s}{k_\parallel v_{\parallel \mathrm{s}}}
$$

$$
\xi'_0 = \frac{\omega - k_\parallel v_{\parallel \mathrm{c}}}{k_\parallel v_{\parallel \mathrm{s}}}
$$

$$
\lambda_0 = \frac{k_\perp u}{\Omega_s}
$$

Equation (5.8) was used for calculations of the dielectric tensor component of the drifting-ring-type velocity distribution.

5.2.2. Numerical solving method for the wave equation

In this wave dispersion code, an initial solution for the wave equation of Eq. (5.4) is numerically calculated by using the residue theorem. Then, the wave equation is numerically solved by using the Newton's method with the calculated initial solution.

a) The residue theorem

To obtain the initial solution for the wave equation of Eq. (5.4), a method using the residue theorem is adopted in this code. If an arbitrary function $f(z)$ with argument of a complex number z is regular except at singular points α_1, α_2, ..., α_l inside a simple closed contour C, the residue theorem is expressed by,

$$\int_C f(z)dz = 2\pi i(\mathrm{Res}[f,\alpha_1] + \mathrm{Res}[f,\alpha_2] + \cdots \mathrm{Res}[f,\alpha_l]) \tag{5.9}$$

where, $\mathrm{Res}[f,\alpha_l]$ is a residue of $f(z)$ at $z = \alpha_l$. As we mentioned in Section 5.2.1, the solution of the wave equation exists when $\det|\boldsymbol{H}| = 0$. Therefore, if a value of integral of $1/\det|\boldsymbol{H}|$ over C in a complex space of the dispersion is not zero, the solution exists inside C. Figure 5.11 shows the schematic drawing of the residue theorem used for the calculation of the initial solution of the wave equation.

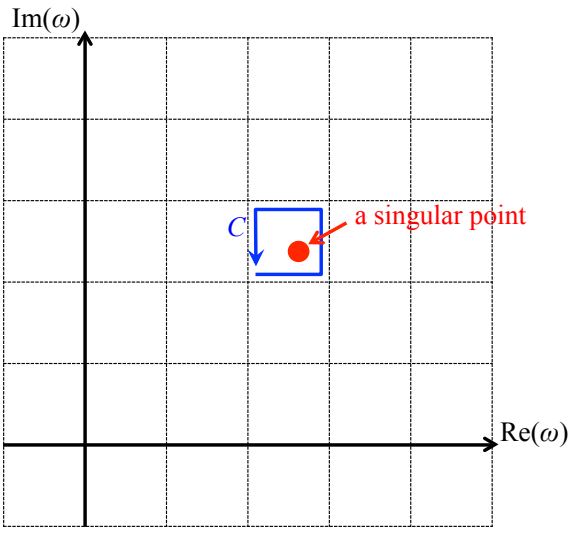

Figure 5.11. A schematic drawing of the residue theorem used for the calculation of the initial solution of the wave equation.

b) The Newton's method

Based on the initial solution obtained from the residue theorem method, the wave equation is numerically solved by using the Newton's method. Here, $f(x)$ is an arbitrary function with argument of x and we defined its solution X as $f(X) \equiv 0$. Figure 5.12 shows the schematic drawing of the general Newton's method. A recursion relation that converges $x_l \to X$ is given by,

$$x_{l+1} = x_l - f(x_l) / \frac{df(x_l)}{dx} \tag{5.10}$$

The initial position x_0 is the calculated initial solution with the residue theorem method. The solution of the wave equation can be numerically obtained by repeating the Newton's method.

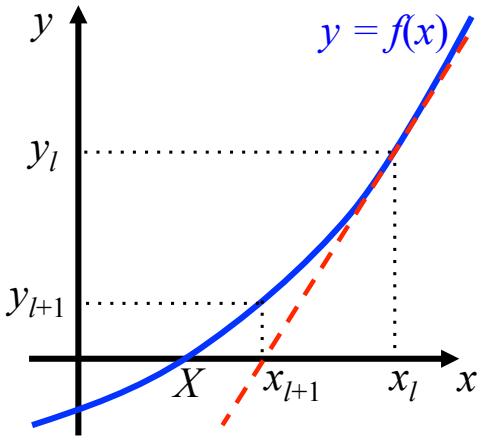

Figure 5.12. A schematic drawing of the Newton's method.

5.2.3. Measurement results of dispersions of ICE(^{3}He)

In general, the dispersion of the ICRF waves is strongly affected by the plasma density as shown in Eq. (2.42) and the wavenumber of the ICRF wave becomes large as the density increases. Figure 5.13 shows $\overline{n_e}$ dependences of (a) normalized wave angular frequencies $\omega/l\Omega_{^3He}(l = 1, 2)$ and (b) toroidal wavenumbers k_φ of the measured ICE(^{3}He). These dependences consist of the observations in several discharges where the plasma density and S_n gradually increase. Error bars of the $\omega/l\Omega_{^3He}$ are small well and negligible. $\omega/l\Omega_{^3He}$ of the fundamental and the 2nd harmonic ICE(^{3}He) is below the unity and that of the fundamental ICE(^{3}He) tends to decrease as $\overline{n_e}$ increases. On the other hand, k_φ of the ICE(^{3}He) increases in the CTR direction with $\overline{n_e}$. As we mentioned in Section 5.1.2, the values of the Doppler shifts $k_\parallel v_\parallel$ are negative. Therefore, the relation between the observed k_φ and $\omega/\Omega_{^3He}$ implies that the ICE(^{3}He) is excited under a condition which is close to the Doppler-shifted ^{3}He ion cyclotron resonance condition because $\omega/\Omega_{^3He}$ tends to decrease as the Doppler shifts becomes large in the negative direction.

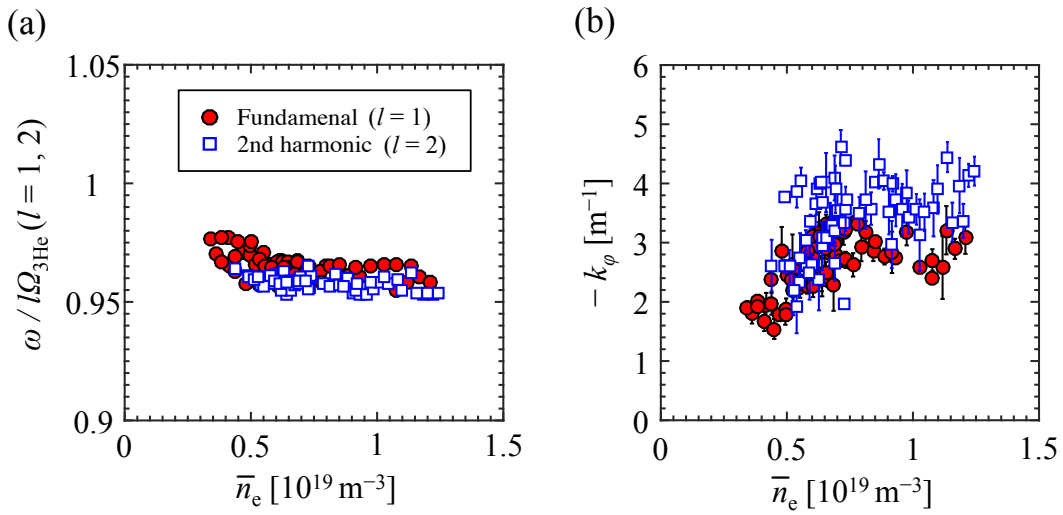

Figure 5.13. Line-averaged density $\overline{n_e}$ dependences of (a) wave angular frequency ω and (b) toroidal wavenumber k_φ of the measured fundamental (circles) and 2nd harmonic ICE(^{3}He) (squares). The angular frequency ω is normalized by the ^{3}He ion cyclotron angular frequencies at the midplane edge of the plasma on the low field side $l\Omega_{^3He}$ $(l = 1, 2)$.

5.2.4. Comparison of dispersions of the calculated MCI with experimental observation

We calculate the dispersions of the MCI driven by the fast ^{3}He ions with the drifting-ring-type velocity distribution, and compare the calculated dispersions with the experimental observations shown in Fig. 5.13. In this section, bulk plasma parameters estimated at the plasma edge on the low field side in the experiments were used for the calculations, and the dispersions (angular frequency ω and parallel wavenumber $k_\parallel$) of the MCI were calculated under the maximum linear growth rate condition. Here, we assumed $k_\parallel \sim k_\varphi$,

$n_{3He}/n_D = 10^{-4}$, $T_D = T_e = 300$ eV and $v_{\|s} = 0.01 v_{3He}$, where $v_{3He} = \sqrt{v_{\|c}^2 + u^2}$ = ~7.2×10^6 m/sec which corresponds to the speed of the fast ^{3}He ions with E = 820 keV. The pitch angle $\phi_{pitch} = \sin^{-1}(u/v_{3He})$ is set to be a pitch angle where the population in the pitch-angle distribution of the fast ^{3}He ions at the plasma edge on the low field side is the largest. A ratio of the bulk plasma density at the plasma edge to the line-averaged density $\overline{n_e}$ is assumed to be constant in order to estimate the temporal change of the density at the plasma edge.

Figure 5.14 shows the comparison results of (a) normalized wave angular frequencies ω/Ω_{3He} and (b) parallel wavenumber of the ICE(^{3}He) between the experimental observations and the MCI calculations. ω/Ω_{3He} of the calculated MCI is close to the experimental observation. In addition, $k_\|$ of the calculated MCI is consistent in a range of ± 1 m^{-1} with the observations. Hence, the comparison results suggest that the measured dispersions of the ICE(^{3}He) is consistent with the MCI.

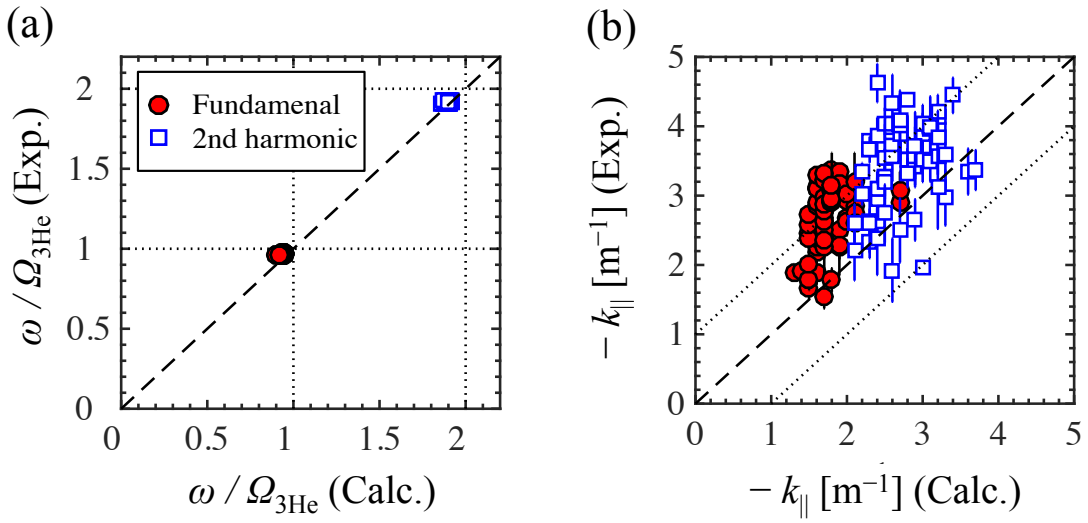

Figure 5.14. Comparisons of (a) wave angular frequency ω and (b) parallel wavenumber $k_\|$ between the observations of the ICE(^{3}He) (Exp.) and the calculations of the MCI (Calc.). The angular frequency ω is normalized by the ^{3}He ion cyclotron angular frequencies at the midplane edge of the plasma on the low field side Ω_{3He}. Here, $k_\|$ is assumed to be k_φ. Circles and squares are the dispersions of the fundamental and 2nd harmonic ICE(^{3}He), respectively. Dashed lines indicate values where the dispersions of the observed ICE(^{3}He) and of the calculated MCI are equal.

The above comparison results suggest that the emission mechanism for the ICE(^{3}He) on JT-60U is the MCI in terms of the dispersion. However, several assumptions were used for these calculations of the dispersions of the MCI: the drifting-ring-type velocity distribution was adopted, the dispersions of the uniform plasma were calculated under the maximum growth rate condition, and the plasma parameters such as the density at the plasma edge were roughly estimated. In addition, the density ratio n_{3He}/n_D and the birth energy of the fast ^{3}He ions were assumed. Further quantitative investigations of the dispersion of the ICE using wave models, in which wave mode structures in the tokamak plasma are taken into account, would be necessary to realize the application of the ICE to the fast ion diagnostics. These investigations of the dispersion using the above wave models are future works.

References in Chapter 5

[1] R. O. Dendy *et al.*, Phys. Plasmas **1**, 1918 (1994).

[2] N. N. Gorelenkov and C. Z. Cheng, Phys. Plasmas **2**, 1961 (1995).

[3] N. N. Gorelenkov and C. Z. Cheng, Nucl. Fusion **35**, 1743 (1995).

[4] K. G. McClements *et al*., Phys. Plasmas **3**, 543 (1996).

[5] K. G. McClements *et al.*, Phys. Rev. Lett. **82**, 2099 (1999).

[6] S. Kakimoto *et al*., Trans. Fusion Sci. Technol. **43-1T**, 86 (2003).

[7] S. Kakimoto *et al*., J. Plasma Fusion Res. SERIES **6**, 741 (2004).

[8] K. Miyamoto, *Plasma Physics and Controlled Nuclear Fusion,* Springer, New York (2005).

Chapter 6
Identification of Key Characteristics of Fast ^{3}He Ion Velocity Distribution Driving ICE(^{3}He)

It is suggested in the previous chapter that the emission mechanism for the ICE(^{3}He) is the MCI in terms of the dispersion. In this chapter, we have investigated the characteristics of the fast ^{3}He ion velocity distribution driving the ICE(^{3}He) in order to reveal whether the observed ICE(^{3}He) is consistent with the MCI even in terms of the fast ^{3}He ion velocity distribution. First, we describe setup for the more quantitative evaluation of the fast ^{3}He ion velocity distribution than that in the previous chapter. Then, we explain a typical discharge where ICE(^{3}He) disappears in spite of a relatively high neutron emission rate, and evaluation results of the distributions in both cases with and without the ICE(^{3}He) excitation. Finally, we compare the distributions between the cases with and without the ICE(^{3}He) excitation to identify the key characteristics of the distribution driving the ICE(^{3}He), and discuss the emission mechanism for the ICE(^{3}He) in terms of the fast ^{3}He ion velocity distribution.

6.1. Setup for more quantitative evaluation of the distributions

In this chapter, to more quantitatively evaluate the fast ^{3}He ion velocity distributions than those in the previous chapter, we additionally took into account the following effects: i) the effects of the toroidal magnetic field ripples, and ii) the influences of the scattering angle of the fusion reaction and the fast D ion velocity vectors on the ^{3}He ion birth velocity distribution. In addition, in order to more locally evaluate the fast ^{3}He ion velocity distribution, iii) influences of the Larmor motions of the fast ^{3}He ions near the sampling box were also taken into account.

i) As we mentioned in Section 3.1, the ferritic steel tiles are installed on the wall on JT-60U [1]. We considered the toroidal magnetic field ripples including the influences of the steel tiles on the wall to calculate the fast ion orbits under the more detailed magnetic configuration. ii) The birth energy of the fusion product strongly depends on the scattering angle of the fusion reaction and the fuel ion velocity vectors [2] as we mentioned in Section 4.2.3. The influence of the scattering angle and the fast D ion velocity vectors were taken into account to more quantitatively evaluate the ^{3}He ion birth velocity distribution, which affects the fast ^{3}He ion slowing-down distribution. iii) To more locally evaluate the fast ^{3}He ion velocity slowing-down distribution, we made the sampling box smaller. Its lengths are 0.02 m in both R and Z directions. The effects of the Larmor motions of the fast ^{3}He ions on the evaluation of the distribution must be taken into account since some fast ^{3}He ions have larger Larmor radii than the size of the sampling box. Thus, we took into account the influence of the Larmor motions of the fast ^{3}He ions on the evaluation of the distributions as follows. We evenly distribute the weight of the test particle into 64 weight elements on a one-cycle full-gyro orbit when the test particle is located near the sampling box. Here, we approximated this full-gyro orbit as a circle with the Larmor radius on the poloidal cross section, and assumed that the center of the full-gyro orbit

is located at the position of the guiding-center orbit. We accumulate the weight elements located inside the sampling box to evaluate the slowing-down velocity distribution.

In this section, taking into account the above effects, we firstly evaluate the fast ^{3}He ion slowing-down distribution at t = 5.1 sec in E48461 as a typical case. We have been already evaluated the distribution at t = 5.1 sec in E48461 in the previous chapter (see Fig. 5.6) without taking into account the above effects. Figure 6.1 shows the sampling boxes at R = 4.25 m and R_{edge} used for the local evaluation of the fast ^{3}He ion distribution. The plasma parameters shown in Fig. 5.3 and the equilibrium shown in Fig 5.4 were used for the fast ion orbit calculations.

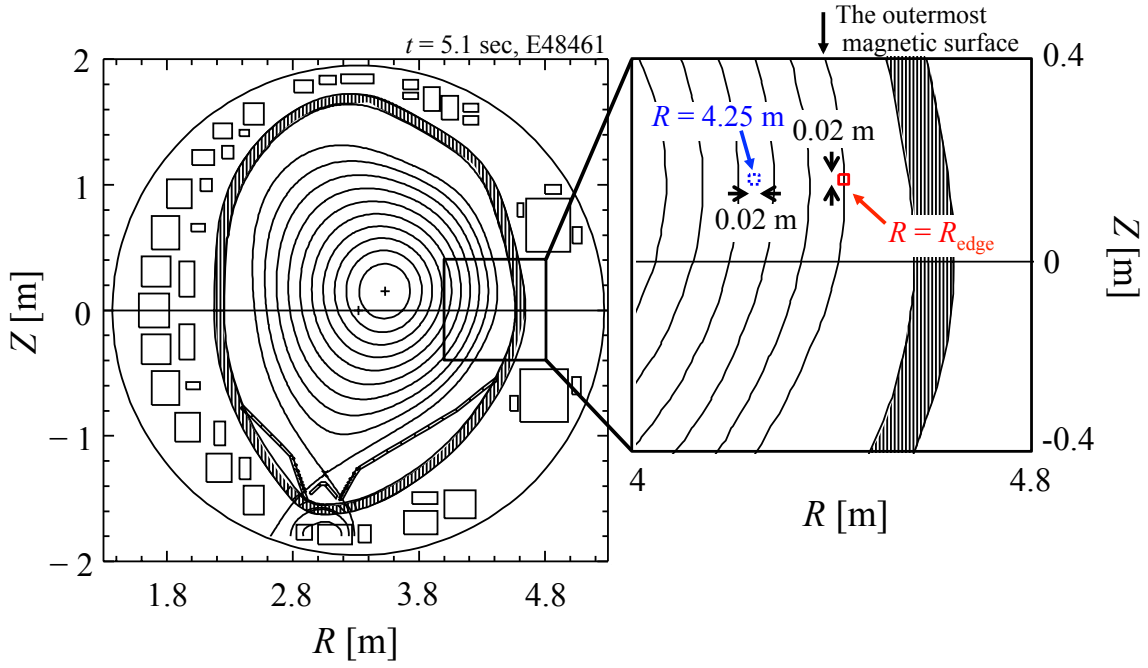

Figure 6.1. A schematic drawing of sampling boxes at R = 4.25 m (dotted box) and $R = R_{edge}$ (solid box) used for the local evaluation of the fast ^{3}He ion velocity distribution at t = 5.1 sec in E48461.

Figure 6.2 shows the ^{3}He ion birth energy and pitch-angle distribution at t = 5.1 sec in E48461. This birth energy and pitch-angle distribution shown in Fig. 6.2 is the birth distribution integrated in the whole plasma region. The birth distribution has a broad structure in the energy direction and a pitch-angle anisotropy due to the influence of the scattering angle and the fast D ion velocity vectors. We used Fig. 6.2 for the initial velocity condition of the fast ^{3}He ion orbit calculations. Figure 6.3 shows the evaluated fast ^{3}He ion slowing-down distributions at (a) $R = 4.25$ m and (b) $R = R_{edge}$ at t = 5.1 sec in E48461. Both distributions have the strong anisotropies in the relatively high-energy region. At $R = 4.25$ m, the distribution has no bump-on-tail structure in the energy direction. On the contrary, the bump-on-tail structure is formed in the distribution at $R = R_{edge}$. These characteristics of the evaluated distributions shown in Fig. 6.3 are the same as those in Fig. 5.6. On the other hand, in the case of $R = R_{edge}$, the energy at the highest distribution density of the bump-on-tail structure is shifted from E = 820 keV to about 500 keV. This is because the birth energy is less than 820 keV in $\phi_{pitch} > 90$ degree as shown in Fig. 6.2. In $\phi_{pitch} > 90$ degree, the fast ^{3}He ions near the plasma center can draw the banana orbits and move toward the low field side as shown in Fig. 5.9. E_{res} is passing nearer the largest population of the bump-on-tail structure than

that in Fig. 5.6(c). Therefore, the evaluations of the distributions shown in Fig. 6.3 can be considered as more quantitative evaluations than those of the distributions shown in Fig. 5.6, while characteristics of these distributions are qualitatively same.

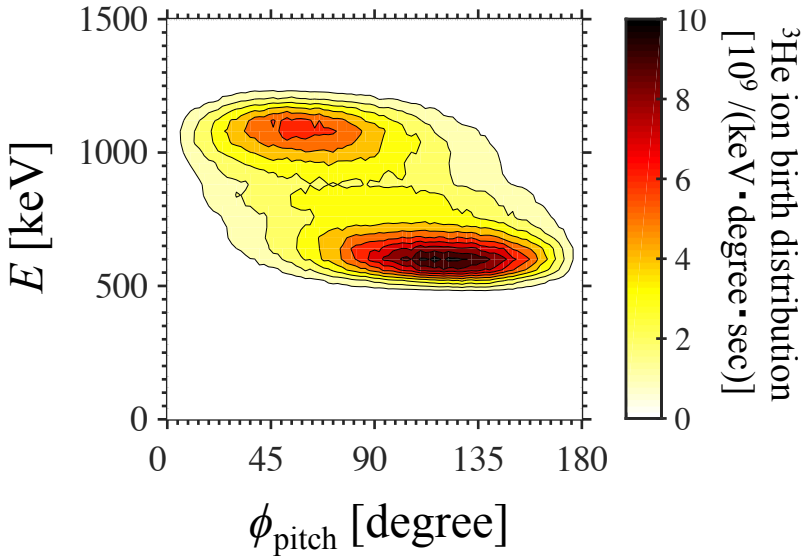

Figure 6.2. The evaluated birth energy E and pitch-angle ϕ_{pitch} distributions of the ^{3}He ions at t = 5.1 sec in E48461.

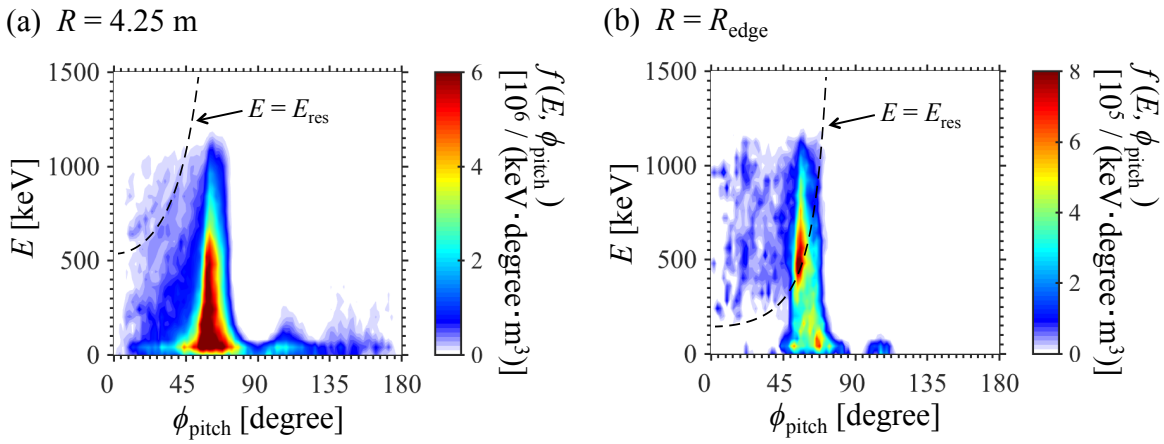

Figure 6.3. Evaluated energy E and pitch-angle ϕ_{pitch} slowing-down distributions of the fast ^{3}He ions at (a) R = 4.25 m and (b) $R = R_{\mathrm{edge}}$ at t = 5.1 sec in E48461. Dashed lines indicate the resonant energies E_{res}. The toroidal magnetic field ripples and the influence of the scattering angle and the fast D ion velocity vectors on the ^{3}He ion birth velocity distribution are taken into account. The sampling boxes shown in Fig. 6.2 are used for these evaluations.

6.2. Disappearance of ICE(^{3}He) in spite of relatively high neutron emission rate

On JT-60U, disappearances of the ICE(^{3}He) were observed in spite of relatively high neutron emission rates. The amount of the ^{3}He ion productions by the DD fusion reactions is almost equal to the neutron emission rate S_n because neutrons and ^{3}He ions are produced by the same DD fusion reaction of Eq. (1.3b) and the DD fusion reactions are dominant. Therefore, it is expected that the intensity of the ICE(^{3}He) becomes stronger as S_n increases if the characteristics of the fast ^{3}He ion distribution are not changed. Thus, we focused on a possibility that the ICE(^{3}He) disappears due to the change of the characteristics of the fast ^{3}He ion velocity distribution. The change of the characteristics of the distribution may decrease the growth rate of the MCI and lead to the disappearance of the ICE(^{3}He).

Figure 6.4 shows the time evolution of (a) the plasma current I_p, (b) the safety factor at 95 % the magnetic flux q_{95} and (c) R at the plasma edge on the low field side R_{edge} in E48473, where the ICE(^{3}He) disappears in spite of the relatively high S_n. R_{edge} decreases from t = ~7.0 sec to ~9.2 sec, indicating that the plasma surface on the low field side moves toward the high field side. I_p, q_{95} and R_{edge} are simultaneously almost constant until t = ~7.0 sec, and become almost constant again from t = 9.2 sec. Namely, the plasma equilibrium is stationary until t = ~7.0 sec and from t = 9.2 sec in E48473.

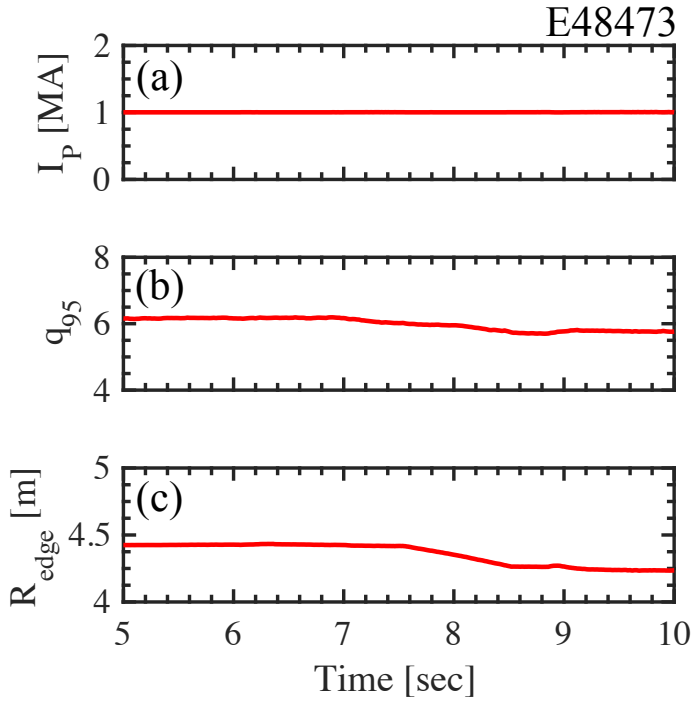

Figure 6.4. Time evolution of (a) the plasma current I_p, (b) q_{safe} at 95 % the magnetic flux q_{95} and (c) R position at the midplane edge of the plasma on the low field side R_{edge} in E48473.

Figure 6.5 shows the time evolution of (a) the P-NB powers P_{NB}, (b) the line-averaged density $\overline{n_e}$, (c) the stored energy W_d, and (d) the neutron emission rate S_n in E48473. The plasma parameters of $\overline{n_e}$ and W_d, and S_n are almost constant until t = 7.0 sec and from t = 9.2 sec as well as the plasma equilibrium. The perpendicular P-NBs are additionally injected from t = 8.8 sec after its temporary stop, and S_n drastically

increases due to the additional P-NB injections. Then, S_n from t = 9.2 sec is much larger than that until t = 7.0 sec. Figure 6.5(e) shows the time evolution of the ICRF fluctuations measured with the ICRF antenna strap. Dotted and dashed lines are f_{cD} and f_{c3He} at the plasma edge on the low field side, respectively. The 2nd harmonic ICE(^{3}He) is clearly observed. However, the 2nd harmonic ICE(^{3}He) is not observed at t = 9.2 sec, at which S_n is relatively high. Figure 6.5(f) shows the time evolution of the toroidal wavenumber k_φ of the 2nd harmonic ICE(^{3}He).

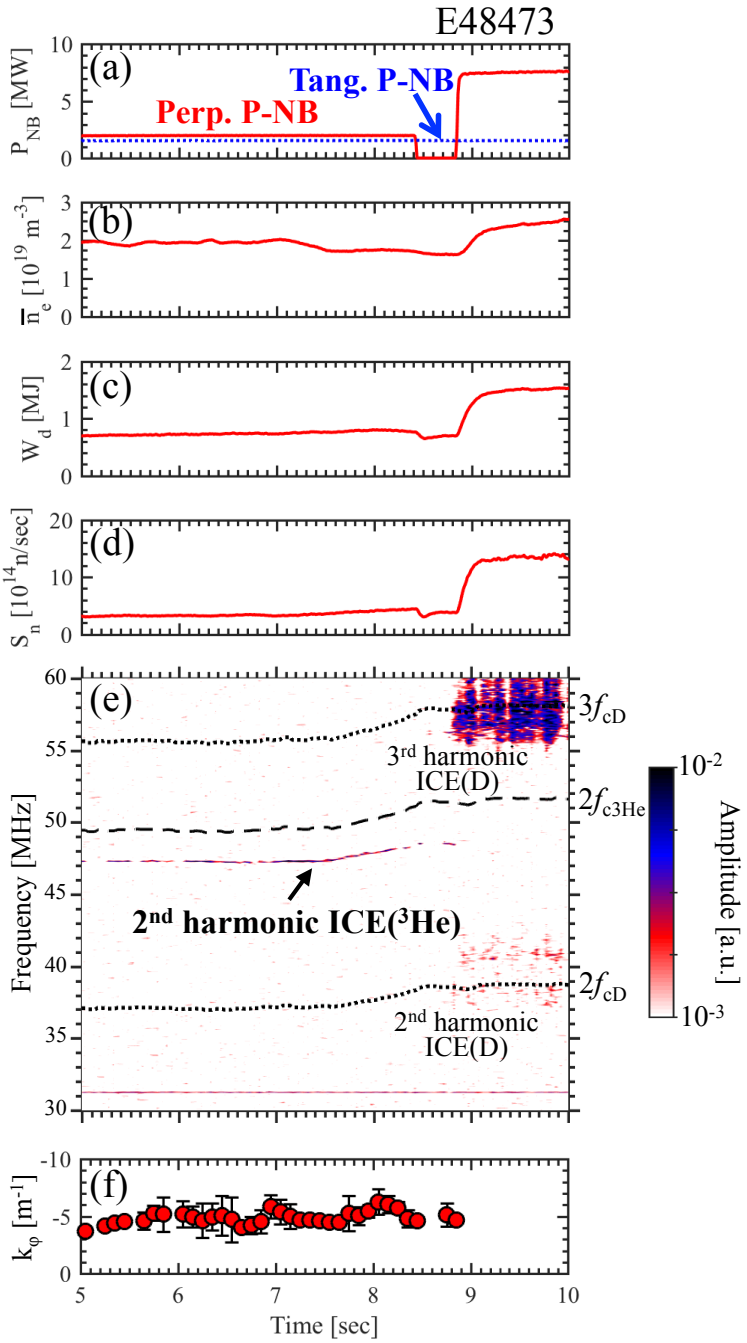

Figure 6.5. Time evolution of (a) the perpendicular (solid line) and tangential P-NB powers (dotted line) P_{NB}, (b) the line-averaged density $\overline{n_e}$, (c) the diamagnetic stored energy W_d, (d) the neutron emission rate S_n, (e) the frequency spectrum of the fluctuations and (f) the toroidal wavenumber k_φ of the 2nd harmonic ICE(^{3}He) in E48473. (e) Dotted and dashed lines are the cyclotron frequencies f_{cD} and f_{c3He} at the midplane edge of the plasma on the low field side, respectively.

Radial profiles of the electron density n_e and temperature T_e were simultaneously measured at t = 5.4 sec and at t = 9.4 sec in E48473. Figure 6.6 shows the radial profiles of (a) n_e, (b) T_e and (c) the safety factor q_{safe} at t = 5.4 sec and 9.4 sec. We calculated the slowing-down times of the fast ^{3}He ions with E = 820 keV at the plasma axis τ_{s0} around t = 5.4 sec and t = 9.4 sec by using the plasma parameters of n_e and T_e shown in Fig. 6.6 and Eq. (2.31). τ_{s0} around t = 5.4 sec and t = 9.4 sec are estimated to be about 0.15-0.2 sec and about 0.2-0.25 sec, respectively. The 2nd harmonic ICE(^{3}He) continues to be observed until t = 7.0 sec and is not observed from t = 9.2 sec even on the time scale longer than τ_{s0}. This indicates that the 2nd harmonic ICE(^{3}He) is observed under the plasma condition around t = 5.4 sec and not observed under the plasma condition around t = 9.4 sec even when the fast ^{3}He ion velocity distributions become the slowing-down distributions. Thus, we evaluated the fast ^{3}He ion slowing-down distributions around t = 5.4 sec for a case with the ICE(^{3}He) excitation, and around t = 9.4 sec for a case without the excitation in E48473. We used the plasma parameters shown in Fig. 6.6 for the fast ion orbit calculations for the cases with and without the ICE(^{3}He) excitation in E48473. In these orbit calculations, we took into account the toroidal magnetic field ripples and the influence of the scattering angle and the fast D ion velocity vectors on the birth velocity distribution to more quantitatively evaluate the fast ^{3}He ion velocity distribution as we mentioned in Section 6.1.

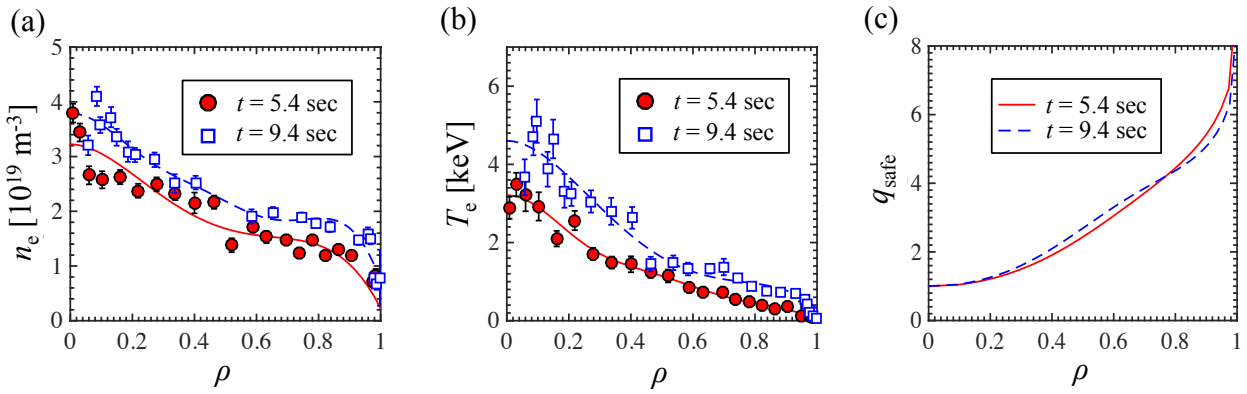

Figure 6.6. Radial profiles of (a) the electron density n_e, (b) the electron temperature T_e, and (c) the safety factor q_{safe} at t = 5.4 sec (circles and solid lines) and at t = 9.4 sec (squares and dashed lines) in E48473.

Figure 6.7 shows the plasma equilibriums at (a) t = 5.4 sec and (b) t = 9.4 sec in E48473. The plasma surface on the low field side at t = 9.4 sec is located at relatively higher field side than that at t = 5.4 sec. Figure 6.7 also shows the sampling boxes used for the evaluation of the fast ^{3}He ion slowing-down distributions in the cases with and without the ICE(^{3}He) excitation in E48473. The small sampling boxes are located at the midplane edge of the plasma on the low field side, and were used to locally evaluate the fast ^{3}He ion slowing-down distributions there. The influences of the Larmor motions of the fast ^{3}He ions on the evaluation of the distributions were also taken into account.

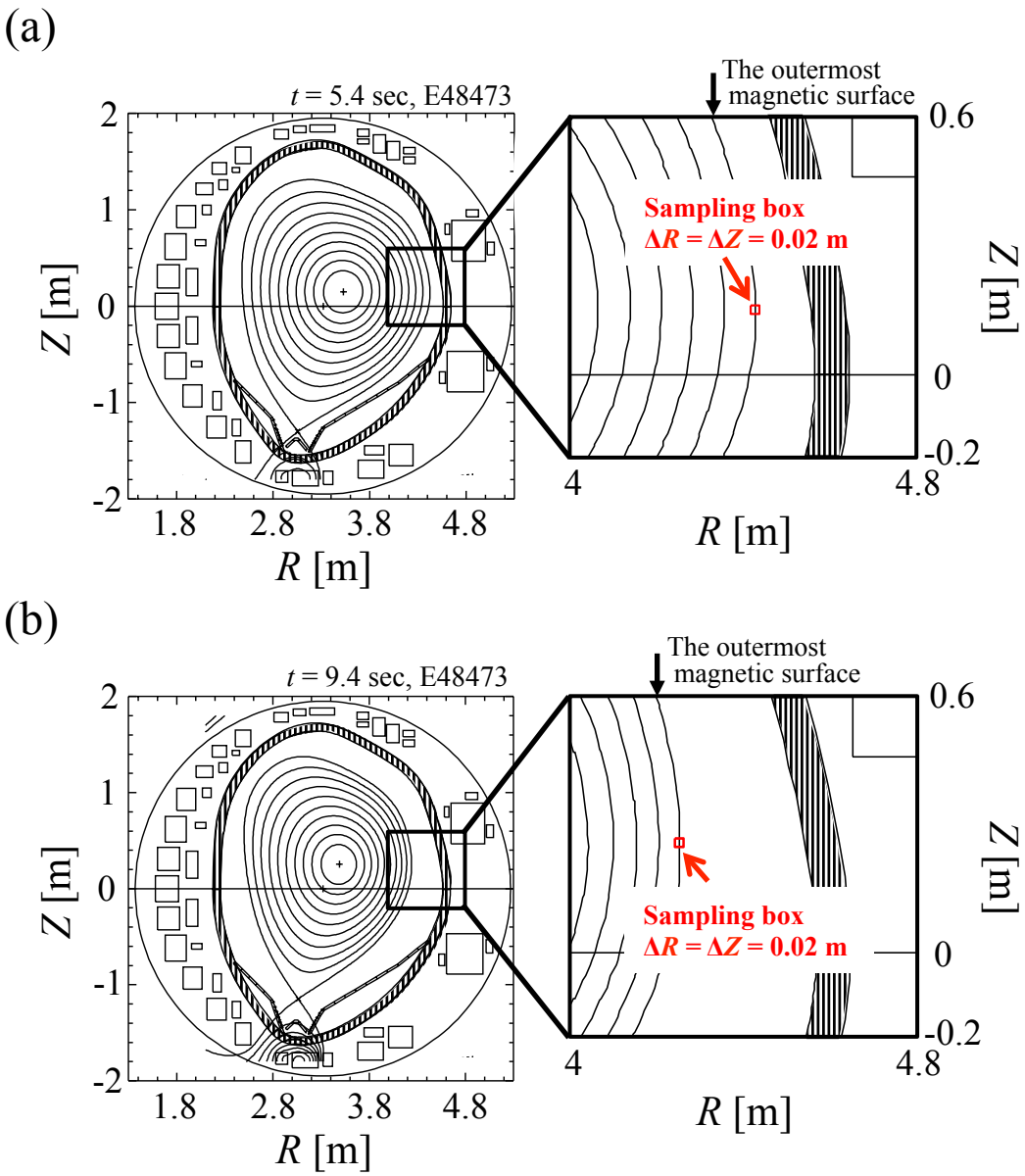

Figure 6.7. The plasma equilibriums (left) and sampling boxes (right) used for the evaluation of the fast ^{3}He ion velocity distribution (a) at t = 5.4 sec and (b) at t = 9.4 sec in E48473. The sampling boxes are located at $R = R_{\mathrm{edge}}$.

6.3. Evaluation results of the distributions

The ^{3}He ion birth spatial and velocity distributions in the cases with and without the ICE(^{3}He) excitation in E48473 were evaluated from the fast D ion orbit calculations. Figure 6.8 shows the ^{3}He ion spatial distributions in the cases (a) with and (b) without the ICE(^{3}He) excitation in E48473. These ^{3}He ion birth spatial distributions shown in Fig. 6.8 are the birth distributions integrated over birth energy and pitch angle of the ^{3}He ions. The ^{3}He ions are produced mainly near the plasma core. Figure 6.9 shows the ^{3}He ion birth energy and pitch-angle distributions in the cases (a) with and (b) without the ICE(^{3}He) excitation in E48473. These ^{3}He ion birth energy and pitch-angle distributions shown in Fig. 6.9 are the birth distributions integrated in the whole plasma regions. We used these ^{3}He ion birth spatial and velocity distributions for the initial conditions of the fast ^{3}He ion orbit calculations.

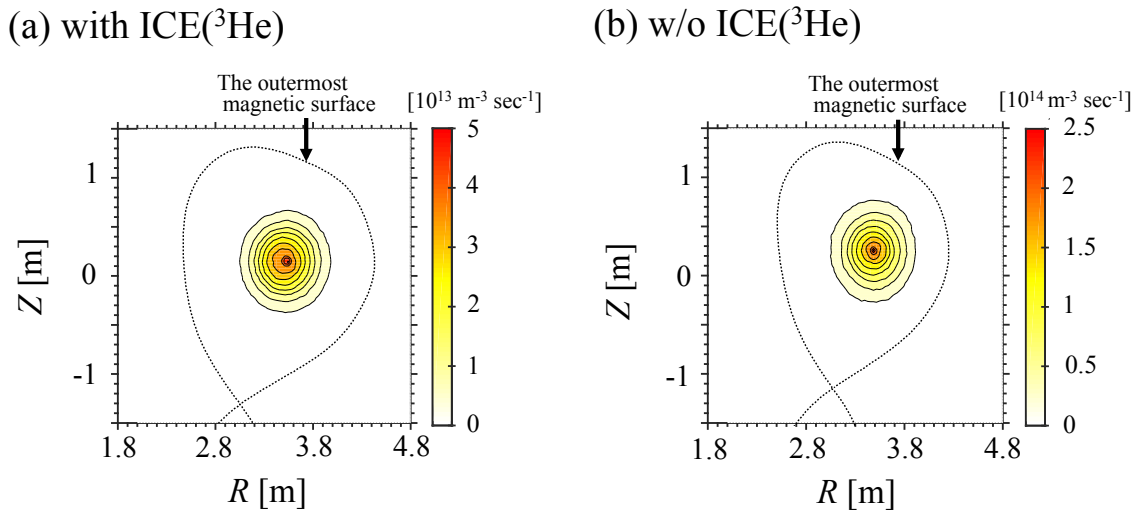

Figure 6.8. The evaluated ^{3}He ion birth spatial distributions on the poloidal cross section in the cases (a) with the ICE(^{3}He) excitation and (b) without the excitation in E48473. Dotted lines are the outermost magnetic surface.

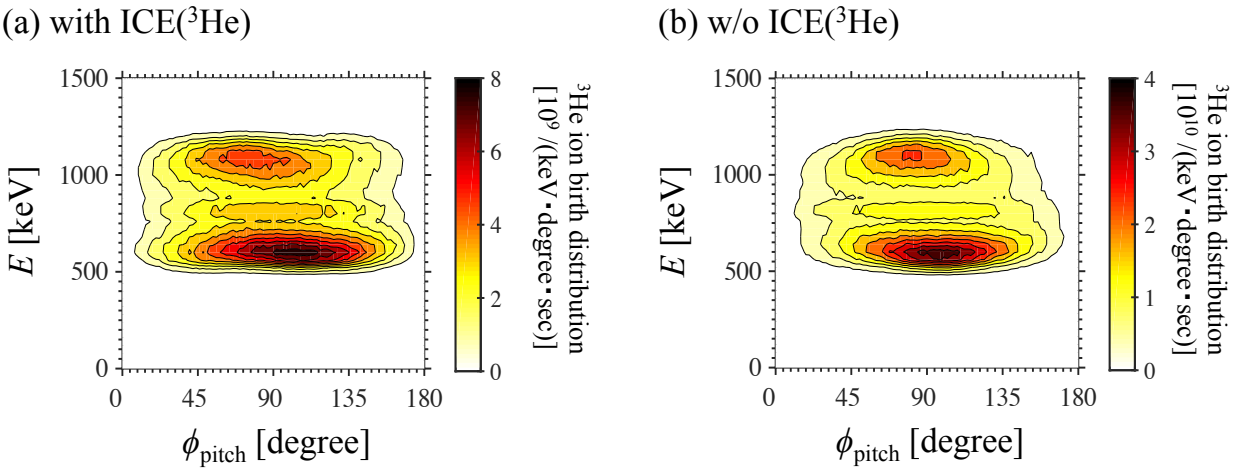

Figure 6.9. The evaluated birth energy E and pitch-angle ϕ_{pitch} distributions of the ^{3}He ions in the cases (a) with the ICE(^{3}He) excitation and (b) without the excitation in E48473.

Figure 6.10 shows the evaluation results of the fast ^{3}He ion energy E and pitch-angle ϕ_{pitch} slowing-down distributions at the plasma edge on the low field side in the cases (a) with and (b) without the ICE(^{3}He) excitation in E48473. Here, we define E_{cr0} as the critical energy E_{cr} at the plasma axis at t = 5.4 sec and 9.4 sec in E48473. E_{cr0} is calculated by using the plasma parameters in Fig. 6.6 and Eq. (2.30). The calculated E_{cr0} is about 90 keV at t = 5.4 sec and is about 130 keV at t = 9.4 sec in E48473. The widths of the pitch-angle distributions of the relatively high-energy fast ^{3}He ions ($E > E_{\mathrm{cr0}}$) are narrow in the both cases, indicating that both distributions are strongly anisotropic in the relatively high-energy region. The pitch-angle distribution densities are the largest around ϕ_{pitch} = 54 degrees in the case with the excitation, and around ϕ_{pitch} = 58 degrees in the case without the excitation. In the relatively low-energy region ($E < E_{\mathrm{cr0}}$), both pitch-angle distributions become broader. This is because the pitch-angle scatterings due to the collisions with the bulk ions frequently occur particularly when $E < E_{\mathrm{cr0}}$. In the case with the excitation, the bump-on-tail structure is formed in the relatively high-energy region. We calculated the resonant energy E_{res} of Eq. (5.1) by using the frequency and the toroidal wavenumber k_φ of the 2$^{\mathrm{nd}}$ harmonic ICE(^{3}He) and the ^{3}He ion cyclotron frequency f_{c3He} at the midplane edge of the plasma on the low field side during t = 5-7 sec in E48473. The 2$^{\mathrm{nd}}$ harmonic ICE(^{3}He) frequency and $2f_{\mathrm{c3He}}$ averaged during t = 5-7 sec in E48473 are ~47.3 MHz and ~49.4 MHz, respectively. The averaged k_φ is about -4.75 m^{-1}. Then, we assumed $k_\parallel = k_\varphi$ for the calculation of E_{res}. E_{res} is passing near the largest population of the bump-on-tail structure, indicating that the evaluated distribution in the case with the excitation can satisfy the destabilization condition for the MCI [3-7]. On the other hand, in the case without the excitation, the energy distribution is a broad structure around ϕ_{pitch} = 58 degrees. The process of the formation of the broader energy distribution in this case is considered as follows. The fast ^{3}He ions with relatively low energies can pass through the plasma edge on the low field side when the plasma surface on the low field side moves toward the high field side. As a result, the proportion of the relatively low-energy fast ^{3}He ions becomes large in the distribution at the plasma edge on the low field side. Then, the relatively low-energy fast ^{3}He ions would make the bump-on-tail structure in the energy distribution broader. In the next section, we compare the distributions between the cases with and without the ICE(^{3}He) excitation in detail.

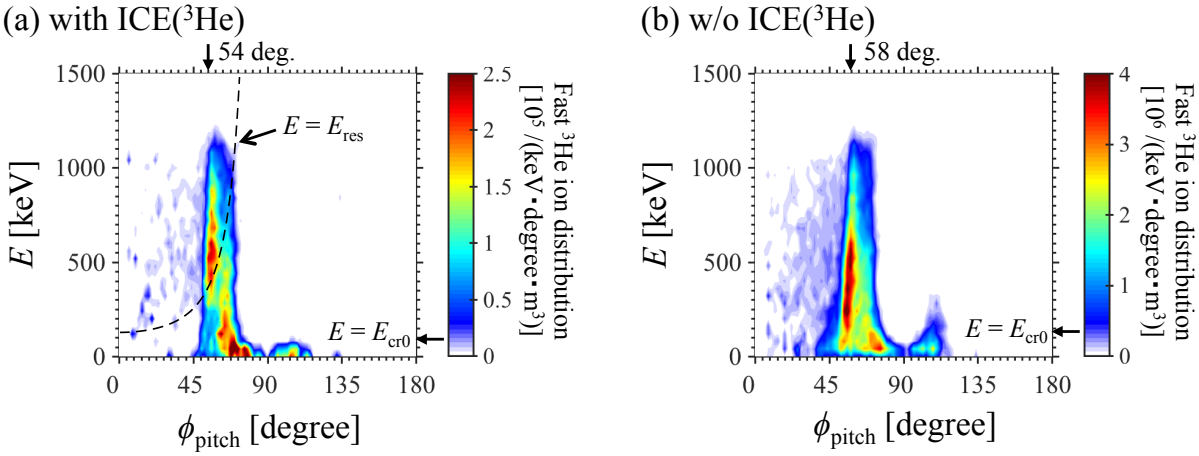

Figure 6.10. Evaluated energy E and pitch-angle ϕ_{pitch} slowing-down distributions of the fast ^{3}He ions at the midplane edge of the plasma on the low field side (see Fig. 6.7) in the cases (a) with the ICE(^{3}He) excitation and (b) without the excitation in E48473. Dashed line is the resonant energy E_{res}. E_{cr0} is the critical energy E_{cr} of Eq. (2.30) at the plasma axis.

6.4. Comparisons of the distributions between the cases when ICE(^{3}He) is observed and not

First, we compared the fast ^{3}He ion slowing-down distributions at the plasma edge on the low field side between the cases with the ICE(^{3}He) excitation and without the excitation in E48473 in terms of characteristics of the pitch-angle distribution and of the energy distribution. Figure 6.11 shows (a) normalized pitch-angle distributions and (b) normalized energy distributions of the fast ^{3}He ions in the cases with and without the ICE(^{3}He) excitation in E48473. Here, the pitch-angle distributions are the distributions averaged from E = 480 keV to 520 keV. The energy distributions are the distributions averaged around $\phi_{\mathrm{pitch}} = 54$ degrees in the case with the excitation, and around $\phi_{\mathrm{pitch}} = 58$ degrees in the case without the excitation. These distributions shown in Fig. 6.11 are normalized with the maximum distribution densities f_{max}. Almost same sharply peaked structures are formed in both normalized pitch-angle distributions. In the case with the excitation, the normalized energy distribution has the bump-on-tail structure peaked around E = 500 keV. On the other hand, the normalized energy distribution has a relatively flat structure in the energy region of $E_{\mathrm{cr0}} < E <$ ~500 keV in the case without the excitation. Therefore, the characteristics of the energy distributions are clearly different between the cases with and without the excitation. Thus, we focused on the bump-on-tail structure formed in the energy distribution, and investigated the difference of its characteristics between the cases with and without the excitation.

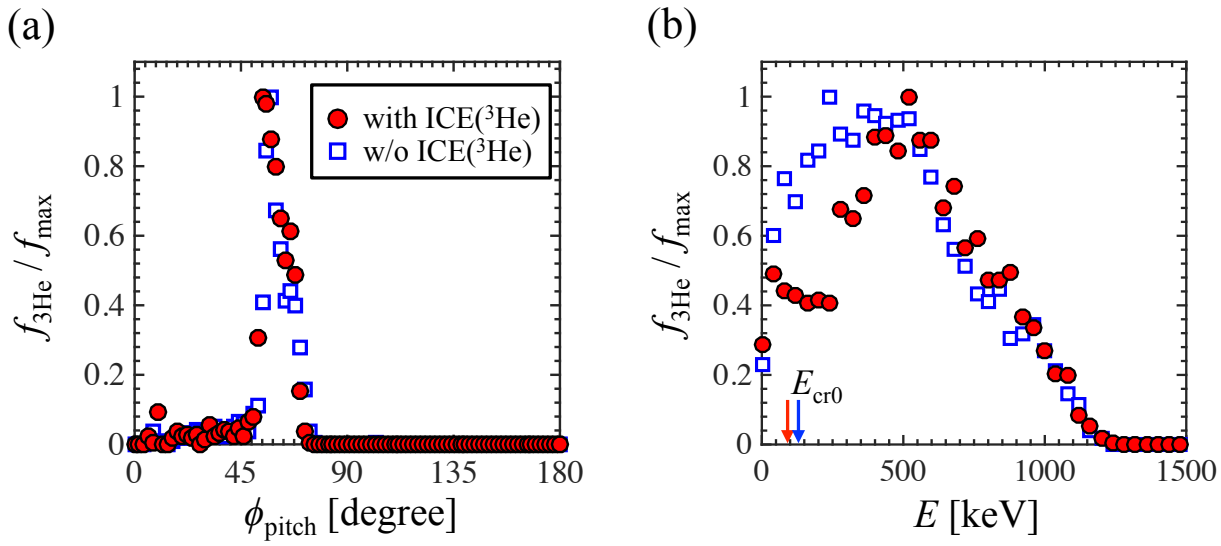

Figure 6.11. Normalized (a) pitch-angle ϕ_{pitch} distributions and (b) energy E distributions of the fast ^{3}He ions at the midplane edge of the plasma on the low field side in the cases with the ICE(^{3}He) excitation (circles) and without the excitation (squares) in E48473. The pitch-angle distributions are the distributions averaged in $E = 500 \pm 20$ keV. The energy distributions are the distributions averaged in $\phi_{\mathrm{pitch}} = 54 \pm 3$ degrees in the case with the excitation, and averaged in $\phi_{\mathrm{pitch}} = 58 \pm 3$ degrees in the case without the excitation. These averaged distributions are normalized with their largest value of the distribution densities f_{max}.

Here, we define a normalized gradient of the energy distribution as $(\Delta f/\Delta E)/f_{\mathrm{N}}$, where $\Delta f/\Delta E$ is a gradient of the energy distribution from E = 200 keV to 500 keV and f_{N} is the energy distribution density at E = 500 keV. $(\Delta f/\Delta E)/f_{\mathrm{N}}$ becomes large in the positive direction when the sharply peaked bump-on-tail structure is formed in the energy direction. $(\Delta f/\Delta E)/f_{\mathrm{N}}$ is negative when no bump-on-tail structure is formed. Figure 6.12 shows R position dependences of the normalized gradients $(\Delta f/\Delta E)/f_{\mathrm{N}}$ in the cases with and without the ICE(^{3}He) excitation. The energy distributions are the distributions averaged around the pitch angles where the distribution density is the largest. $(\Delta f/\Delta E)/f_{\mathrm{N}}$ near the plasma edge on the low field side in the case with the excitation is larger than that in the case without the excitation. In addition, positive values of $(\Delta f/\Delta E)/f_{\mathrm{N}}$ are localized near the plasma edge on the low field side in the case with the excitation. The region near the plasma edge on the low field side is considered as the emission region for the ICE(^{3}He) based on the relation between the observed ICE(^{3}He) frequency and the ^{3}He ion cyclotron frequency [8-10]. Hence, it is suggested that the peaked bump-on-tail structure formed in the energy distribution contributes to the ICE(^{3}He) excitation. Thus, we evaluated $(\Delta f/\Delta E)/f_{\mathrm{N}}$ at the midplane edge of the plasma on the low field side in several discharges, and compared $(\Delta f/\Delta E)/f_{\mathrm{N}}$ between the cases with and without the ICE(^{3}He) excitation.

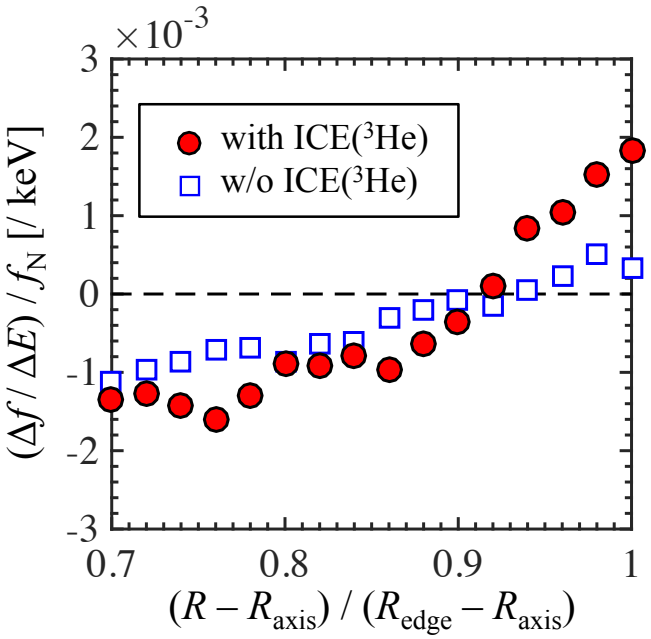

Figure 6.12. R position dependences of normalized gradients of the energy distributions $(\Delta f/\Delta E)/f_{\mathrm{N}}$ in the case with the ICE(^{3}He) excitation (circles) and without the excitation (squares) in E48473. Here, $\Delta f/\Delta E$ is the gradient of the energy distribution from E = 200 keV to 500 keV and f_{N} is the energy distribution density at E = 500 keV.

Figure 6.13 shows the relation between $(\Delta f/\Delta E)/f_{\mathrm{N}}$ of the evaluated fast ^{3}He ion energy distributions and measured amplitudes of the 2$^{\mathrm{nd}}$ harmonic ICE(^{3}He) in the several discharges where one or more NBs are injected and $S_{\mathrm{n}} > 2\times10^{14}$ n/sec. The amplitudes in the case without the ICE(^{3}He) excitation are set to be on the horizontal axis. The ICE(^{3}He) tends to be observed in the relatively large region of $(\Delta f/\Delta E)/f_{\mathrm{N}}$. Hence, the analysis results of the fast ^{3}He ion velocity distributions indicate that the formation of the relatively peaked bump-on-tail structure in the energy distribution is necessary for the ICE(^{3}He) excitation.

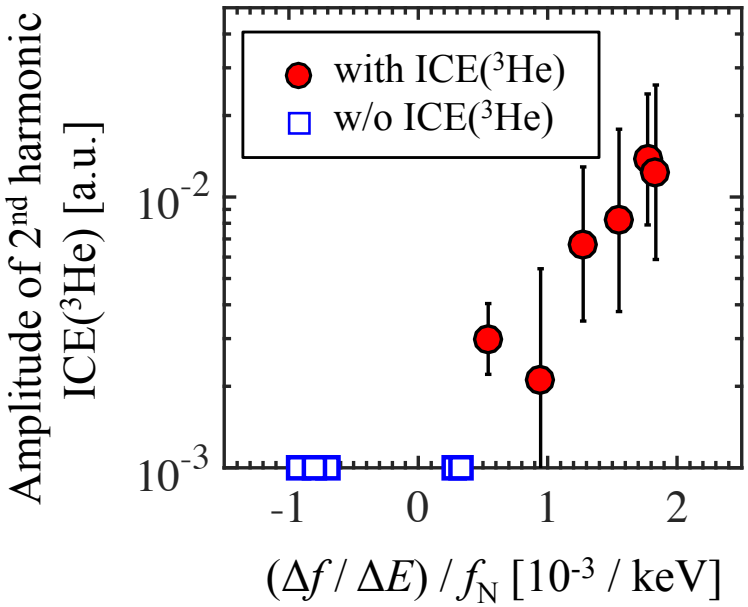

Figure 6.13. A relation between the normalized gradients of the evaluated fast ^{3}He ion energy distributions $(\Delta f/\Delta E)/f_{\mathrm{N}}$ and measured amplitude of the 2nd harmonic ICE(^{3}He) in several discharges. Circles and squares are data points in the cases with the ICE(^{3}He) excitation and without the excitation, respectively. The data points of the case without the excitation are set to be on the horizontal axis.

References in Chapter 6

[1] K. Shinohara *et al.*, Nucl. Fusion **47**, 997 (2007).

[2] H. Brysk, Plasma Phys. **15**, 611 (1973).

[3] R. O. Dendy *et al.*, Phys. Plasmas **1**, 1918 (1994).

[4] N. N. Gorelenkov and C. Z. Cheng, Phys. Plasmas **2**, 1961 (1995).

[5] N. N. Gorelenkov and C. Z. Cheng, Nucl. Fusion **35**, 1743 (1995).

[6] K. G. McClements *et al*., Phys. Plasmas **3**, 543 (1996).

[7] K. G. McClements *et al.*, Phys. Rev. Lett. **82**, 2099 (1999).

[8] M. Ichimura *et al.*, Nucl. Fusion **48**, 035012 (2008).

[9] M. Ichimura *et al*., Proc. 22nd IAEA Fusion Energy Conf. (Geneva, Switzerland, 2008) EX/P8-2 (2008).

[10] K. G. McClements *et al*., Nucl. Fusion **58**, 096020 (2018).

Chapter 7
Influence of Gradient of Bump-on-Tail Structure in the Energy Direction on Linear Growth Rate of the MCI

The analysis results of the fast ^{3}He ion velocity distribution in the previous chapter indicate that the formation of the relatively peaked bump-on-tail structure in the energy direction is necessary to drive the ICE(^{3}He) and the characteristics of the bump-on-tail structure are important to understand the emission condition for the ICE(^{3}He) on JT-60U. In this chapter, we have improved our wave dispersion code to numerically calculate the dispersion with a fast ^{3}He ion velocity distribution function that can have the narrow-width pitch-angle distribution and express both broad and sharply peaked bump-on-tail structures in the energy direction. Then, we have investigated influences of the gradient of the bump-on-tail structure in the fast ^{3}He ion velocity distribution on the linear growth rate of the MCI by using the improved code.

First, we explain improvement methods of our wave dispersion code so that the dispersion can be numerically calculated for an arbitrary velocity distribution function. Then, we describe results of its benchmark tests. Next, we introduce the function for the fast ^{3}He ion velocity distribution. Finally, we explain calculation results of the growth rate of the MCI by using the improved wave dispersion code, and discuss the influences of the gradient of the bump-on-tail structure on the growth rate.

7.1. Extension of velocity distribution function used in the wave dispersion code to arbitrary function

The analysis result of the fast ^{3}He ion velocity distribution shows that the emission condition for the ICE(^{3}He) strongly depends on the gradient (or the spread) of the bump-on-tail structure in the energy direction as shown in Fig. 6.13. In the previous theoretical studies using the drifting-ring-type distribution, the necessity of the sharply peaked fast ion velocity distribution for the excitation of the ICE has been suggested [1, 2]. The linear growth rate of the MCI increases as the spread of the distribution becomes smaller. In other words, the MCI growth rate increases as the gradient of the distribution becomes steep. These calculations were carried out with a general wave model, in which the linear theory and the homogeneous plasma model are assumed as in our wave dispersion code. In these studies, not only the spreads of the bump-on-tail structure in the energy direction, but also the widths of the pitch-angle distribution were simultaneously changed. The drifting-ring-type distribution function such as Eq. (5.7), which is adopted in our wave dispersion code, cannot express the broad bump-on-tail structure in the energy direction while the narrow width of the pitch-angle distribution is kept. Therefore, the influences originating from the changes in the spread of the bump-on-tail structure and in the width of the pitch-angle distribution cannot be distinguished when the drifting-ring-type distribution function is used for the calculations. In other studies, it has been reported that the spread of the bump-on-tail structure in the energy direction has large

influence on the linear growth rate of the MCI [3, 4]. In these calculations, the width of the pitch-angle distribution was assumed to be sufficiently narrow and the pitch-angle distribution was expressed by a delta function. In addition, a wave model for compressional Alfvén eigenmodes localized at the plasma edge on the low field side and $|k_\parallel| \ll k_\perp$ were assumed. In order to simply understand the emission mechanism for the ICE(^{3}He), it is important to investigate the influence of the gradient of the bump-on-tail structure on the growth rate of the MCI under the general wave model. Thus, we extended the velocity distribution function model used in the wave dispersion code to the arbitrary one in order to investigate the contribution of the gradient of the bump-on-tail structure to the emission condition for the ICE(^{3}He) in terms of the growth rate of the MCI under the general wave model.

7.1.1. Numerical calculation methods with tent function for the analytic continuation

An issue is known that the second term in the right side of Eq. (2.42) cannot be numerically calculated with a simple trapezoidal integration method for the arbitrary distribution function f_{s0} when the solution is $\mathrm{Im}(\omega) \leq 0$ [5]. This is because singular points exist at the cyclotron resonance conditions $\omega = l\Omega_s + k_\parallel v_\parallel$ in the integrand. To resolve this issue, a numerical calculation method with linear tent functions has been often used [6, 7]. In this method, the numerator is approximated as a sum of the linear tent functions. Then, the second term can be numerically calculated even when $\mathrm{Im}(\omega) \leq 0$. We adopted the numerical calculation method with the linear tent functions and improved the wave dispersion code used in Chapter 5 so that the dispersion relation can be numerically solved even when f_{s0} is the arbitrary distribution function and $\mathrm{Im}(\omega) \leq 0$.

The second term in the right side of Eq. (2.42) can be expressed by,

$$\boldsymbol{I}_{s,l} = \int \frac{\boldsymbol{C}(v_\parallel)}{\omega - k_\parallel v_\parallel - l\Omega_s} dv_\parallel \tag{7.1}$$

where,

$$\boldsymbol{C}(v_\parallel) = 2\pi \frac{\omega_{ps}^2}{\omega^2} \int v_\perp \boldsymbol{\Lambda}_{s,l} \left(\frac{l\Omega_s}{v_\perp} \frac{\partial f_{s0}}{\partial v_\perp} + k_\parallel \frac{\partial f_{s0}}{\partial v_\parallel} \right) \frac{1}{n_s} dv_\perp \tag{7.2}$$

Here, we define meshes of the parallel velocity $v_\parallel$ at equal velocity spaces as $v_{\parallel j} = v_{\parallel j-1} + \Delta v_\parallel$, where j is the mesh number and $\Delta v_\parallel$ is the velocity mesh space. Then, we approximated $\boldsymbol{C}(v_\parallel)$ with the linear tent function T_j as follows:

$$\boldsymbol{C}(v_\parallel) = \sum_j \boldsymbol{C}(v_{\parallel j}) T_j \tag{7.3}$$

where, the linear tent function T_j is given by,

$$T_j = \begin{cases} 1 - \dfrac{|v_\parallel - v_{\parallel j}|}{\Delta v_\parallel} & \text{if} |v_\parallel - v_{\parallel j}| \leq \Delta v_\parallel, \\ 0 & \text{otherwise.} \end{cases} \tag{7.4}$$

Here, we define the parallel velocity $v_{\parallel j_m}$ at the mesh number j_m as $v_{\parallel j_m} \equiv (\omega - l\Omega_s)/k_\parallel$. Substituting

Eq. (7.3) into Eq. (7.1) yields,

$$\boldsymbol{I}_{s,l} = \sum_j \frac{\boldsymbol{C}(v_{\parallel j})}{-k_\parallel} K_{j-j_m} = \sum_j \frac{\boldsymbol{C}(v_{\parallel j+j_m})}{-k_\parallel} K_j \tag{7.5}$$

where, K_j is given by,

$$K_j = \int_{-1}^{1} \frac{1-|\chi|}{\chi + j} dX = \begin{cases} \ln\left(\frac{j+1}{j-1}\right) - j \ln\left(\frac{j^2}{j^2-1}\right) & |j| > 1, \\ \pm \ln 4 & j = \pm 1, \\ i\pi & j = 0. \end{cases} \tag{7.6}$$

$$\chi \equiv \frac{v_\parallel - v_{\parallel j}}{\Delta v_\parallel} \tag{7.7}$$

The dielectric tensor for the arbitrary distribution function can be numerically calculated by substitution of $\boldsymbol{I}_{s,l}$ of Eq. (7.5) into the second term in the right side of Eq. (2.42).

7.1.2. Benchmark test

We carried out benchmark tests to validate our improved wave dispersion code in which the numerical calculation method with the tent function is adopted. In these benchmark tests, we compared analytical and numerical solutions of the wave equations. Here, we used the model for the homogeneous D plasma including the minority ^{3}He ions.

Two cases of the benchmark tests were carried out. i) The first one is a case when the velocity distribution function of the minority ^{3}He ions is the isotropic Maxwell distribution and its temperature is 10 keV. ii) The second one is a case when the ^{3}He ion velocity distribution function is the bi-Maxwell distribution. In this case, the parallel and perpendicular temperatures are 10 keV and 300 keV to the magnetic field line, respectively. Namely, the distribution has a strong temperature anisotropy. The velocity distribution functions of the bulk D plasma are assumed to be the isotropic Maxwell distribution in both cases. The dielectric components can be analytically calculated when the velocity distribution function is the (bi-) Maxwell distribution. Thus, we calculated the dielectric components of the minority ^{3}He ion by using both of the analytical method and the numerical method with the tent function, while we calculated the bulk plasma component only analytically.

The common parameters used for the benchmark tests are as follows. The magnetic field strength B is 3 T, densities of the electron n_e and the D ion n_D are 1×10^{19} m^{-3}, their temperatures are $T_\mathrm{e} = T_\mathrm{D} = 300$ eV, and the wave propagation angle $\phi_k = \sin^{-1}(k_\perp/|k|)$ is 80 degree. The density of the minority ^{3}He ions $n_{^3\mathrm{He}}$ is 1×10^{11} m^{-3}.

Figure 7.1 shows the calculation results of the real angular frequency $\mathrm{Re}(\omega/\Omega_{^3\mathrm{He}})$ and the linear growth rate $\mathrm{Im}(\omega/\Omega_{^3\mathrm{He}})$ as a function of the wavenumber k in the cases when the ^{3}He ion velocity distribution functions are (a) the Maxwell distribution and (b) the bi-Maxwell distribution. The values on the vertical axes are normalized with the ^{3}He ion cyclotron angular frequency $\Omega_{^3\mathrm{He}}$. It is clearly shown that the numerical solution almost reproduces the analytical one even if $\mathrm{Im}(\omega) \leq 0$ in both cases. It was confirmed that our improved wave dispersion code can numerically solve the dispersion even if $\mathrm{Im}(\omega) \leq 0$.

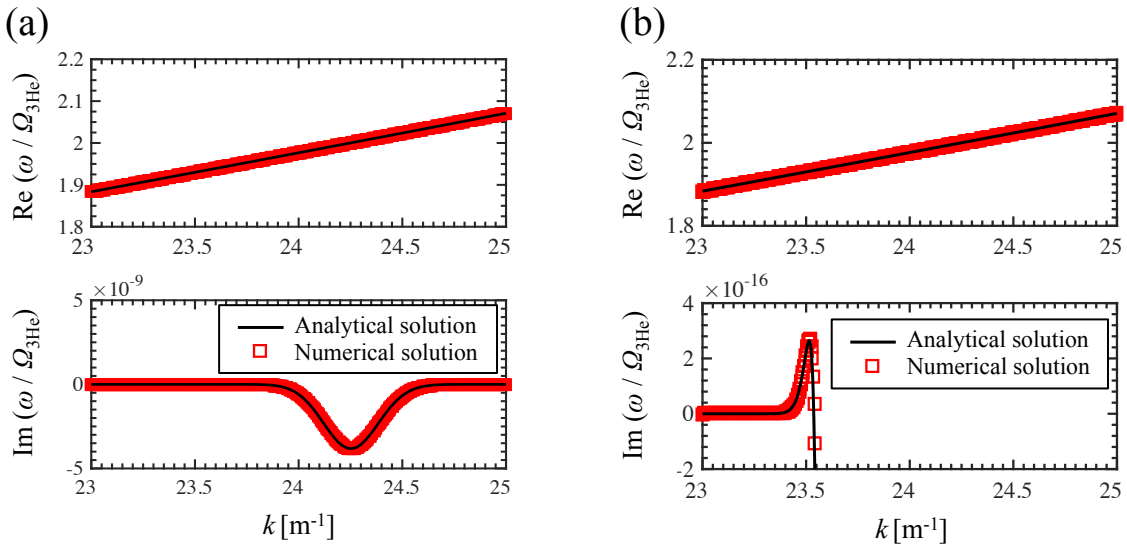

Figure 7.1. The calculation results of $\mathrm{Re}(\omega/\Omega_{3\mathrm{He}})$ (upper) and $\mathrm{Im}(\omega/\Omega_{3\mathrm{He}})$ (lower) as a function of k in the cases when the ^{3}He ion velocity distribution functions are (a) the Maxwell distribution and (b) the bi-Maxwell distribution. The dispersion relations on the fast Alfvén wave branch are shown. Solid lines indicate the analytical solutions and squares are the numerical solutions. Here, the ^{3}He ion temperatures used for the calculations are (a) 10 keV in both parallel and perpendicular directions, and (b) 10 keV in the parallel direction and 300 keV in the perpendicular direction to the magnetic field line.

7.2. Function for fast ^{3}He ion velocity distribution

In this section, we introduce a following ^{3}He ion velocity distribution function $f_{3\mathrm{He}}$ that can have the narrow-width pitch-angle distribution and express both broad and sharply peaked bump-on-tail structures in the energy direction.

$$f_{3\mathrm{He}} = C_d \exp\left[-\frac{\{(v_\parallel - v_{0\parallel})\cos\phi_0 + (v_\perp - v_{0\perp})\sin\phi_0\}^2}{\delta v_{\mathrm{E}}^2}\right] \exp\left[-\frac{\{-(v_\parallel - v_{0\parallel})\sin\phi_0 + (v_\perp - v_{0\perp})\cos\phi_0\}^2}{\delta v_{\mathrm{p}}^2}\right] \tag{7.8}$$

where $v_{0\parallel}$ and $v_{0\perp}$ are parallel and perpendicular velocities at the largest population of the velocity distribution, respectively. ϕ_0 is a pitch angle at the largest population and defined as $\phi_0 = \sin^{-1}(v_{0\perp}/v_0)$. δv_{E} and δv_{p} are velocity spreads of the distribution in the energy direction and in the pitch-angle direction, respectively. The decrement of δv_{E} indicates the increment of the gradient of the bump-on-tail structure in the energy direction. C_{d} is a normalization constant of the velocity distribution function.

Figure 7.2 shows examples of the modeled ^{3}He ion velocity distributions with Eq. (7.8) when $n_{3\mathrm{He}}$ = 3×10^9 m^{-3}, v_0 = 5.65 ×10^6 m/sec, ϕ_0 = 56 degree, $v_{0\parallel} = v_0\cos\phi_0$, $v_{0\perp} = v_0\sin\phi_0$ and δv_{p} = 0.05×10^6 m/sec. $n_{3\mathrm{He}}$, v_0 and ϕ_0 are set to be similar values to those of the evaluated fast ^{3}He ion velocity distribution at the midplane edge of the plasma on the low field side such as the distribution at t = 5.4 sec in E48473 (see Fig. 6.10(a)). The largest population of the bump-on-tail structure in Fig. 6.10(a) is located around E = ~500 keV and ϕ_{pitch} = ~54 degrees. v_0 is almost corresponding to the speed of the

^{3}He ion having the energy of 500 keV. The distributions with (a) $\delta v_E = 0.01 v_0$ and (b) $0.1 v_0$ are shown. Here, we adjusted C_d so that n_{3He} is kept to be constant when δv_E changes. The distributions of Eq. (7.8) can express different spreads in the energy direction while the widths in the pitch-angle distribution are narrow.

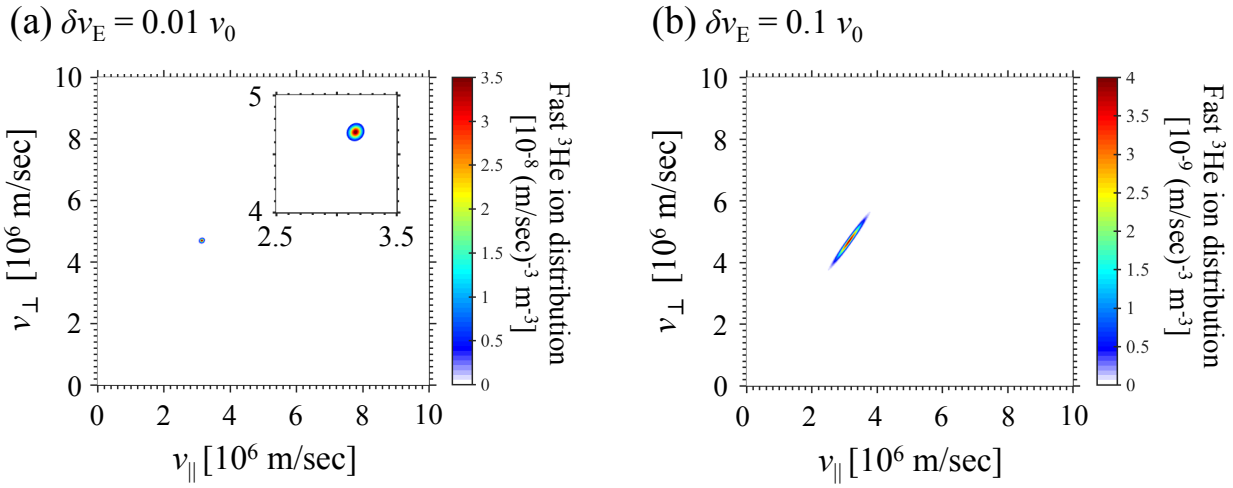

Figure 7.2. The modeled ^{3}He ion velocity distributions of Eq. (7.8) in the case of (a) $\delta v_E = 0.01\ v_0$ and (b) $0.1\ v_0$. Other parameters for the distributions are as follows: $v_0 = 5.65 \times 10^6$ m/sec, $\phi_0 = 56$ degree, $v_{0\parallel} = v_0 \cos\phi_0$, $v_{0\perp} = v_0 \sin\phi_0$, $\delta v_p = 0.05 \times 10^6$ m/sec and $n_{3He} = 3 \times 10^9$ m^{-3}.

7.3. Influence of gradient of bump-on-tail structure on linear growth rate of the MCI

We calculated the dispersion of the MCI by using the improved wave dispersion code. The calculation model is the uniform D plasma including the minority fast ^{3}He ions with the velocity distributions of Eq. (7.8). The parameters used for the calculations are as follows. $B = 2.5$ T, $n_e = n_D = 2 \times 10^{18}$ m^{-3}, $T_e = T_D = 300$ eV, $n_{3He} = 3 \times 10^9$ m^{-3}, $v_0 = 5.65 \times 10^6$ m/sec, and $\phi_0 = 56$ degree. These values are estimated from the plasma parameters at the plasma edge on the low field side at $t = 5.4$ sec in E48473, and set to be similar to the parameters of the evaluated fast ^{3}He ion distribution there. Here, we assume the wave propagation angle $\phi_k = 100$ degree, $v_{0\parallel} = v_0 \cos\phi_0$, $v_{0\perp} = v_0 \sin\phi_0$ and $\delta v_p = 0.05 \times 10^6$ m/sec.

Figure 7.3 shows calculation results of $\mathrm{Im}(\omega/\Omega_{3He})$ of the MCI in cases of $\delta v_E = 0.01 v_0$, $0.015 v_0$ and $0.02 v_0$. The horizontal axis is $\mathrm{Re}(\omega'/\Omega_{3He})$, where $\omega' = \omega - k_\parallel v_{0\parallel}$. The MCI becomes unstable in the frequency of $\mathrm{Re}(\omega') \sim 2\Omega_{3He}$. $\mathrm{Im}(\omega/\Omega_{3He})$ decreases as δv_E increases. Figure 7.4 shows δv_E dependence of the maximum value of $\mathrm{Im}(\omega/\Omega_{3He})$. The maximum value of $\mathrm{Im}(\omega/\Omega_{3He})$ drastically increases as δv_E becomes small. Namely, the linear growth rate of the MCI significantly increases as the gradient of the bump-on-tail structure becomes steep. These calculation results of the dependences of the growth rate of the MCI on the spread of the bump-on-tail structure are consistent with the previous theoretical works [1-4], and qualitatively agree with the analysis results of the characteristics of the fast ^{3}He ion velocity distribution driving ICE(^{3}He) (see Fig. 6.13). Hence, we have revealed that the growth rate of the MCI is qualitatively consistent with the excitation condition of the ICE(^{3}He).

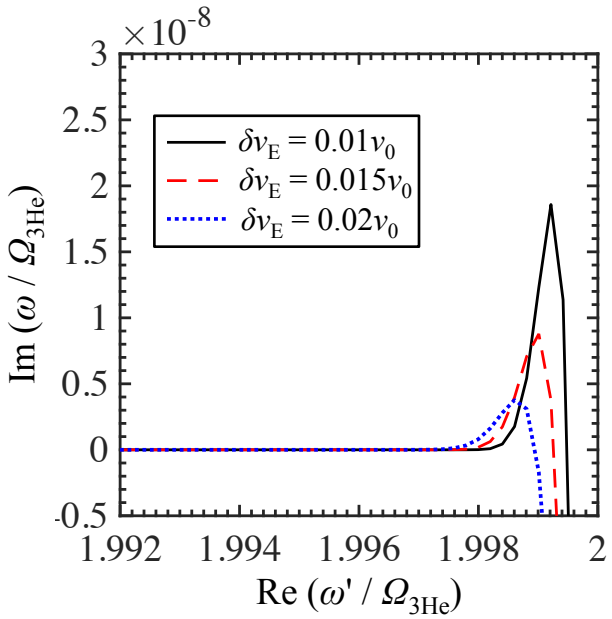

Figure 7.3. $\mathrm{Im}(\omega/\Omega_{3\mathrm{He}})$ of the MCI as a function of $\mathrm{Re}(\omega'/\Omega_{3\mathrm{He}})$. Here, ω' is defined as $\omega' = \omega - k_{\parallel}v_{0\parallel}$. Solid, dashed and dotted lines indicate the linear growth rates in the cases of $\delta v_{\mathrm{E}} = 0.01v_0$, $0.015v_0$ and $0.02v_0$, respectively. Other parameters used for the dispersion calculations are as follows: B = 2.5 T, $n_{\mathrm{e}} = n_{\mathrm{D}}$ = 2×10^{18} m^{-3}, $T_{\mathrm{e}} = T_{\mathrm{D}}$ = 300 eV, $n_{3\mathrm{He}}$ = 3×10^{9} m^{-3}, v_0 = 5.65 $\times10^{6}$ m/sec, ϕ_0 = 56 degree, $v_{0\parallel} = v_0\cos\phi_0$, $v_{0\perp} = v_0\sin\phi_0$ and δv_{p} = 0.05×10^{6} m/sec.

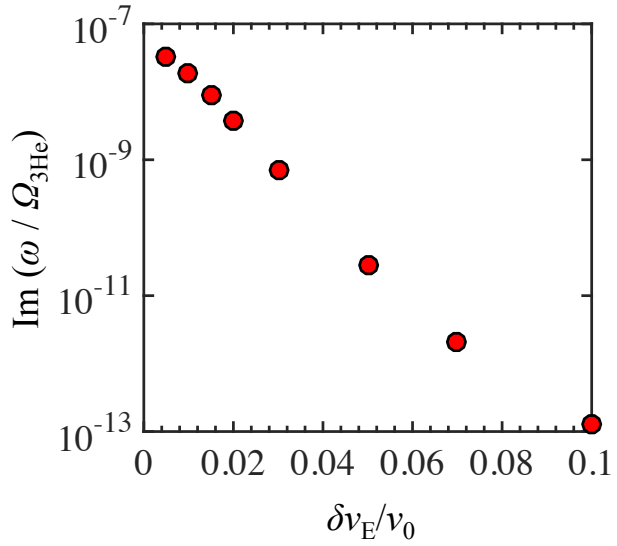

Figure 7.4. Dependence of the maximum $\mathrm{Im}(\omega/\Omega_{3\mathrm{He}})$ of the MCI on the spread of the bump-on-tail structure δv_{E}. Parameters used for the dispersion calculation are the same as those in Fig. 7.3 except for δv_{E}.

However, there are still a few quantitative discrepancies between the evaluated fast ^{3}He ion velocity distribution and the dependence of the MCI growth rate on the gradient of the bump-on-tail structure. For

examples, i) the absolute value of the calculated growth rate of the MCI is not high enough, and ii) the gradient of the evaluated bump-on-tail structure is relatively small.

i) The growth rates even in the case of $\delta v_{\mathrm{E}} = 0.01 v_0$ are lower than 10^{-6} order which is the least value expected from a time scale of the observed growth of the ICE(^{3}He). One of the possibilities is that the emission region for the ICE(^{3}He) is actually located slightly inside the plasma edge on the low field side. $n_{3\mathrm{He}}$ inside the plasma edge is much higher than that at the plasma edge. In general, the growth rate of the MCI increases as $n_{3\mathrm{He}}$ becomes high when the characteristics of the velocity distribution do not change. In addition, the gradient of the evaluated bump-on-tail structure of the fast ^{3}He ion velocity distribution is still positive even slightly inside the plasma edge as shown in Fig. 6.12. In the dispersion calculations shown in Figs. 7.3 and 7.4, the growth rates were evaluated by using the plasma parameters and the distribution only at the plasma edge on the low field side. Therefore, there is a possibility that the growth rate of the MCI is underestimated since $n_{3\mathrm{He}}$ used for the calculation is the value at the plasma edge. Moreover, our wave dispersion code adopts the wave model for the homogeneous plasma and does not include the wave mode structures in the tokamak plasma. This limitation of the wave model would also deteriorate the quantitativity of the MCI growth rate calculations.

ii) The positive gradients of the evaluated bump-on-tail structures shown Fig. 6.13 are relatively small by comparison with the dependence of the calculated growth rate on δv_{E} shown in Fig. 7.4. A possible reason is the limitation of the orbit calculation model used in this study. The positive gradient of the bump-on-tail structure is formed because the fast ^{3}He ions cannot reach the plasma edge on the low field side when their energies are decreased. In the orbit calculations with the OFMC in this study, the loss processes of the fast ions are only the collisions with the bulk plasma and with the wall. Therefore, the positive gradient of the evaluated bump-on-tail structure would be larger when other fast ion loss processes are additionally taken into account in the orbit calculations.

We discussed the quantitative discrepancies between the evaluated fast ^{3}He ion velocity distribution and the dependence of the MCI growth rate. However, these reasons are not concluded in this study. Understanding the cause for the above quantitative discrepancies is important toward the development of the ICE diagnostics. Further quantitative investigations on the fast ion velocity distribution and on the MCI growth rate are future works.

References in Chapter 7

[1] K. G. McClements *et al*., Phys. Plasmas **3**, 543 (1996).

[2] K. G. McClements *et al.*, Phys. Rev. Lett. **82**, 2099 (1999).

[3] N. N. Gorelenkov and C. Z. Cheng, Phys. Plasmas **2**, 1961 (1995).

[4] N. N. Gorelenkov and C. Z. Cheng, Nucl. Fusion **35**, 1743 (1995).

[5] K. Miyamoto, *Plasma Physics and Controlled Nuclear Fusion,* Springer, New York (2005).

[6] J. C. Wright *et al*., Commun. Comput. Phys. **4**, 545 (2008).

[7] N. Bertelli *et al*., Nucl. Fusion **57**, 056035 (2017).

Chapter 8
Conclusion

The purpose of this study is to reveal the emission mechanism for the ICE(^{3}He) in JT-60U as a typical ICE driven by the fusion product in the tokamak plasma. For the purpose, we have investigated whether the dispersions of the observed ICE(^{3}He) is consistent with the MCI (Chapter 5), what characteristics of the fast ^{3}He ion velocity distribution are necessary for the ICE(^{3}He) excitation (Chapter 6) and whether these characteristics are consistent with the growth rate of the MCI (Chapter 7).

In Chapter 5, first, we evaluated the fast ^{3}He ion velocity distributions in the almost stationary plasma with the OFMC. As the results, it was found that the evaluated fast ^{3}He ion distribution at the plasma edge on the low field side has both of the bump-on-tail structure and the strong pitch-angle anisotropy in the time period of the observation of the ICE(^{3}He). These characteristics are similar to those of the drifting-ring-type distribution. In addition, the evaluated distribution at the plasma edge on the low field side is consistent with the destabilization condition for the MCI in terms of the ion cyclotron resonance. Although the evaluated distribution inside the plasma can have the strong anisotropy, no bump-on-tail structure is formed there. Next, we developed the wave dispersion code that can numerically calculate the dispersion for the drifting-ring-type velocity distribution function. Then, we calculated the dispersions of the MCI by using the wave dispersion code, and compared the calculated dispersions with the measured frequency and toroidal wavenumber of the ICE(^{3}He) on JT-60U. As the results, the frequencies of the observed ICE(^{3}He) are close to those of the calculated MCI. In addition, the toroidal wave numbers of the observed ICE(^{3}He) are consistent with those of the MCI in the range of $\pm$ 1 m^{-1}. Hence, the comparison results suggest that the measured dispersions of the ICE(^{3}He) are consistent with the MCI.

In Chapter 6, in order to identify key characteristics of the distribution driving the ICE(^{3}He), we more quantitatively evaluated the fast ^{3}He ion velocity distributions, and compared the distributions between the cases when the ICE(^{3}He) is observed and not. As the results, it was found that the evaluated fast ^{3}He ion distributions at the plasma edge on the low field side have the relatively peaked bump-on-tail structure in the energy direction in the case with the ICE(^{3}He) excitation. On the other hand, the evaluated distributions in the case without the excitation have the almost flat structure in the energy direction or no bump-on-tail structure. Namely, these results indicate that the formation of the relatively peaked bump-on-tail structure is necessary for the excitation of the ICE(^{3}He).

In Chapter 7, first, we improved the wave dispersion code so that the dispersion for the arbitrary velocity distribution function can be numerically calculated. Next, using the improved wave dispersion code, we investigated the influence of the gradient of the bump-on-tail structure in the energy direction on the linear growth rate of the MCI. Here, the adopted function for the ^{3}He ion velocity distribution is a function that can have the narrow-width pitch-angle distribution and express both of the peaked and flat bump-on-tail structures in the energy direction. The calculation results of the growth rate of the MCI show that the growth rate drastically increases as the gradient of the bump-on-tail structure becomes steep. The analysis results of the fast ^{3}He ion velocity distribution are qualitatively consistent with the growth rate of the MCI.

Hence, we revealed that the emission mechanism for the ICE(^{3}He) is the MCI in terms of the dispersion and the fast ^{3}He ion velocity distribution.

Acknowledgements

First of all, I would like to show my greatest appreciation to Professor Dr. Shunsuke Ide of National Institutes for Quantum and Radiological Science and Technology (QST). He is my supervisor in the Doctoral program. He directed this study and strongly guided me. He always gave me considerable encouragement when I faced some difficult problems in this study. Without his guidance and encouragement, this study would not have been accomplished.

Next, I am deeply grateful to Professor Dr. Mizuki Sakamoto, Associate Professor Dr. Masayuki Yoshikawa of University of Tsukuba and Associate Professor Dr. Tomohide Nakano of QST for giving valuable and helpful comments.

Then, I would like to express my deepest appreciation to Dr. Kouji Shinohara of QST, Professor Dr. Makoto Ichimura of University of Tsukuba and Associate Professor Dr. Ryuya Ikezoe of Kyushu University. Dr. Shinohara always gave me valuable comments and advices in this study. In-depth technical discussions with him have been very insightful, and indispensable in progress of this study. Professor Dr. Ichimura and Associate Professor Dr. Ikezoe have patiently taught me fundamentals of research and plasma physics since I was an undergraduate student, and also gave me valuable comments and suggestions in this study.

I would like to thank Lecturer Dr. Mafumi Hirata of University of Tsukuba for not only giving helpful advices in this study, but also supporting my research life in the university as a group leader of ICRF group of Plasma Research Center (PRC) of the university. I would also like to thank Professor Dr. Yousuke Nakashima and Professor Dr. Tsuyoshi Imai of University of Tsukuba for giving the opportunity to study at PRC of the university.

I would like to express my gratitude to Dr. Yutaka Kamada, Dr. Nobuhiko Hayashi, Dr. Naoyuki Oyama, Dr. Takahiro Suzuki, and members of JT-60 team of QST for very valuable and constructive discussions.

I would like to thank the late Professor Tsuguhiro Watanabe of National Institute for Fusion Science for developing a wave dispersion code that can numerically calculate the dispersion in the case of the bi-Maxwell distribution function. Our wave dispersion code has been developed based on his wave dispersion code. I would also like to thank Dr. Shingo Kakimoto and Mr. Gennosuke Oda. They are from PRC of University of Tsukuba. Dr. Kakimoto gave me helpful advice about usage of the wave dispersion code. Mr. Oda helped me to analytically calculate the dielectric tensor in the case of the drifting-ring-type distribution function.

I am grateful very much to Mr. Masanobu Suzuki of Computer Associated Laboratory, Inc. for teaching usage of the OFMC and supporting the calculation with the OFMC. The calculations with the OFMC were mainly conducted using the supercomputer SGI ICE X in the Japan Atomic Energy Agency.

I am also grateful very much to Mr. Shota Sugiyama for his advice about the calculation of the birth energy of the fusion product in the laboratory system. He is a Ph. D. student at Department of Applied Quantum Physics and Nuclear Engineering of Kyushu University.

I would like to thank members of ICRF group of PRC of University of Tsukuba. I would particularly like to thank Mr. Yasunori Washo, Dr. Takuro Yokoyama, Mr. Yuki Saito, Mr. Takuma Iimura, Mr. Yoshiaki Iwamoto, Mr. Takuya Okada, Mr. Kazuyuki Watanabe, Mr. Seowon Jang, Mr. Kohei Takeyama, Mr. Junpei Itagaki, Mr. Yuto Onodera, Mr. Koki Izumi, Mr. Atsuto Tanaka, Mr. Yushi Kubota, and Mr. Ryo Sekine. Thanks to them, I could spend a fruitful time in the university, and discussions with them were valuable.

I would like to express my heartfelt appreciation to members of advanced plasma research group of QST. I

would particularly like to express the appreciation to Dr. Nobuyuki Aiba, Dr. Mitsuru Honda, Dr. Andreas Bierwage, Dr. Junya Shiraishi, Dr. Yoshiaki Miyata, Dr. Mitsunori Toma, Dr. Takuma Wakatsuki, Dr. Shizuo Inoue, Dr. Emi Narita, and Dr. Shohei Yamoto. Thanks to them, I could spend a very wonderful research life in the Doctoral program at QST.

I would like to show my appreciation to University of Tsukuba and QST for establishment and operation of the Cooperative Graduate School system. Thanks to the system, I could study at QST in the Doctoral program. In addition, I was employed as a graduate school course researcher at QST. I would also like to show my appreciation to QST for their financial support.

Finally, I would like to express my cordial gratitude to my family for their support and encouragement. In particular, I would like to thank my wife for her continuing support.

List of Publications

[1] S. Sumida, K. Shinohara, R. Ikezoe, M. Ichimura, M. Sakamoto, M. Hirata, S. Ide, "Comparison of Dispersion Model of Magneto-Acoustic Cyclotron Instability with Experimental Observation of ^{3}He Ion Cyclotron Emission on JT-60U", J. Phys. Soc. Jpn. **86**, 124501 (2017).

[2] S. Sumida, K. Shinohara, R. Ikezoe, M. Ichimura, M. Sakamoto, M. Hirata, S. Ide, "Study on ion cyclotron emission excited by DD fusion produced ions on JT-60U", Proc. the 45th European Physical Society Conference on Plasma Physics (Prague, Czech, 2018), P2.1002 (2018).

[3] S. Sumida, K. Shinohara, R. Ikezoe, M. Ichimura, M. Sakamoto, M. Hirata, S. Ide, "Characteristics of fast ^{3}He ion velocity distribution exciting ion cyclotron emission on JT-60U", Plasma Phys. Control. Fusion **61**, 025014 (2019).